

Stage long de recherche, FIP M1

# COLD FLOWS IN THE MARENOSTRUM SIMULATION

*Accrétion de gaz froids dans la simulation MareNostrum*

Jonathan Freundlich

Under the supervision of Professor Avishai Dekel,  
Racah Institute of Physics (Hebrew University of Jerusalem, Israel)

February 25<sup>th</sup> - August 25<sup>th</sup>, 2008

## Abstract

The standard lore in the idealized picture of galaxy formation was that the gas was first heated to the halo virial temperature behind an expanding virial shock. The articles by Dekel and Birnboim (2003, 2005) showed that the virial shock was not necessarily stable: below a threshold halo mass, the shock is unstable. Furthermore, these articles proposed a new scenario for galaxy formation: beyond the critical mass, a cold and a hot mode of accretion coexist. Some of the gas is shock-heated to the virial temperature, but some of it remains cold and penetrates deeply into the galaxy and these cold flows feed the galaxy very efficiently.

Our goal is to highlight the cold flows in the galaxies of the MareNostrum simulation. We isolate some galaxies from this cosmological simulation and define slices to study the gas accretion. The results confirm the predictions of Dekel and Birnboim and can be compared to theoretical analyses as well as related to star formation rate observations.

## Résumé

Le scénario traditionnel pour la formation des galaxies impliquait l'existence d'un choc autour du rayon viriel de la galaxie. Les articles de Dekel et Birnboim (2003, 2005) ont montré que ce choc n'était pas toujours stable: il existe ainsi une masse critique pour la galaxie en-deça de laquelle le choc ne peut être stable. De plus, ces articles ont prédit que même au-dessus de cette masse critique, des filaments de gaz froid n'ayant subi aucun choc pouvaient pénétrer profondément dans la galaxie: les *cold flows*. Ainsi, selon ce nouveau scénario, deux types d'accrétion peuvent se côtoyer: d'un côté une accrétion de gaz chaud, peu dense et qui a subi un choc, de l'autre des écoulements de gaz froid plus denses et qui apportent la plus grande partie du gaz à l'intérieur de la galaxie.

Nous cherchons à mettre en évidence ces *cold flows* dans la simulation MareNostrum: il s'agit d'une simulation cosmologique d'où nous isolons certaines galaxies pour en observer des coupes et pour en étudier l'apport en gaz. Les résultats obtenus confirment les prédictions de Dekel et Birnboim et peuvent être comparés avec les résultats théoriques, ainsi que reliés aux observations du taux de formation d'étoiles.

# Contents

<b>1</b>	<b>Formation of structure in the standard model of cosmology</b>	<b>7</b>
1.1	The $\Lambda$ CDM model . . . . .	7
1.1.1	A Friedmann-Lemaître model . . . . .	7
1.1.2	Cold dark matter and a cosmological constant . . . . .	8
1.1.3	A scenario for the early history of the universe . . . . .	10
1.2	The formation of structures . . . . .	11
1.2.1	The principal mechanism : gravitational instability in an expanding universe . . . . .	11
1.2.2	Hierarchical clustering . . . . .	12
1.3	The MareNostrum simulation . . . . .	13
1.3.1	The MareNostrum supercomputer . . . . .	13
1.3.2	A cosmological N body and hydrodynamics simulation . . . . .	14
1.3.3	Available data . . . . .	14
<b>2</b>	<b>Cold flows in the MareNostrum simulation</b>	<b>16</b>
2.1	Shock heated gas and cold flows . . . . .	16
2.1.1	The standard picture of infall to a disk . . . . .	16
2.1.2	Stability of the virial shock . . . . .	16
2.1.3	Cold streams in a hot medium . . . . .	18
2.2	Highlighting the cold streams in the MareNostrum simulation . . . . .	19
2.2.1	Different morphologies . . . . .	19
2.2.2	Slices reveal cold flows . . . . .	20
2.2.3	Isolating the high flux regions : smooth flows versus clumpy accretion . . . . .	22
2.3	How can we find systematically the best slice to view the streams ? . . . . .	22
2.3.1	The direction of the disks . . . . .	22
2.3.2	A numerical bias concerning the direction of the disks . . . . .	23
2.3.3	An idea to isolate the direction of the flows . . . . .	24

<b>3</b>	<b>Accretion around galaxies</b>	<b>25</b>
3.1	Histograms . . . . .	25
3.1.1	One dimensional histograms . . . . .	25
3.1.2	Decomposing galaxies into components: <i>bird plots</i> . . . . .	25
3.2	Flux feeding the galaxy . . . . .	26
3.2.1	Flux profiles . . . . .	26
3.2.2	Smooth flows versus mergers . . . . .	29
3.3	Building the disk : the direction of the cold flows . . . . .	29
3.3.1	Hammer-Aitoff maps . . . . .	29
3.3.2	Comparison between the direction of the disk and the direction of the flows . . . . .	30
<b>A</b>	<b>Matlab programs</b>	<b>35</b>
A.1	Extracting the data from the MareNostrum simulation . . . . .	35
A.1.1	Reading the cubes . . . . .	35
A.1.2	Defining the environment . . . . .	35
A.1.3	Virial mass and virial radius . . . . .	36
A.2	Defining the desired quantities . . . . .	37
A.2.1	Virial quantities . . . . .	37
A.2.2	Physical quantities . . . . .	37
A.2.3	Finding the center of the cube . . . . .	38
A.2.4	Projected density . . . . .	39
A.3	Viewing a slice . . . . .	40
A.3.1	Defining the slice . . . . .	40
A.3.2	How do the slice look like ? . . . . .	41
A.3.3	An image of the slice : density . . . . .	41
A.4	The direction of the disk . . . . .	42
A.4.1	Inertial tensor . . . . .	42



A.4.2	Angular momentum . . . . .	43
A.4.3	Comparing the two methods . . . . .	43
A.4.4	Study of a numerical bias : the alignment with the grid . . . . .	44
A.5	Bird plots . . . . .	44
A.6	Spherical coordinates . . . . .	45
A.6.1	Unity sphere . . . . .	45
A.6.2	Transferring to spherical coordinates . . . . .	46
A.7	Flux profiles . . . . .	46
A.7.1	Flux as a function of the radius . . . . .	46
A.7.2	Flux profiles : plots . . . . .	47
A.7.3	Density profiles . . . . .	48
A.8	Hammer-Aitoff maps . . . . .	49
A.8.1	Rotating the spherical grid . . . . .	49
A.8.2	Hammer-Aitoff projection . . . . .	49
<b>B</b>	<b>Projected densities</b>	<b>50</b>
B.1	Five random $\sim 10^{11}M_{\odot}$ haloes at $z = 2.46$ . . . . .	50
B.2	Five random $\sim 10^{12}M_{\odot}$ haloes at $z = 2.46$ . . . . .	51
B.3	Five random $\sim 10^{13}M_{\odot}$ haloes at $z = 2.46$ . . . . .	52
B.4	Five random $\sim 10^{12}M_{\odot}$ haloes at $z = 1.57$ . . . . .	53
B.5	Five random $\sim 10^{12}M_{\odot}$ haloes at $z = 4.01$ . . . . .	54
<b>C</b>	<b>Slices for four <math>\sim 10^{12}M_{\odot}</math> haloes at <math>z = 2.46</math></b>	<b>55</b>
C.1	Halo 303 output 75 . . . . .	55
C.2	Halo 310 output 75 . . . . .	56
C.3	Halo 311 output 75 . . . . .	57
C.4	Halo 314 output 75 . . . . .	58
<b>D</b>	<b>Workshop poster : <i>New understanding of galaxy evolution</i></b>	<b>59</b>
<b>E</b>	<b>Submitted <i>Nature</i> article : <i>Massive galaxy formation by cold streams</i></b>	<b>60</b>

## Introduction

In the last ten years, huge observation programs and the development of computer simulations have transformed cosmology from a highly speculative science into a predictive science. We now speak of a “standard model of cosmology” which would describe as accurately as possible the structure and the evolution of the universe. An important part of cosmology consists in refining that model by constraining its parameters, but even if this model is extremely successful at explaining the large scale structure of the universe, a phenomenological approach is necessary to achieve a better understanding of the complex processes involved in structure formation. The current Big Bang model assumes a very homogeneous universe at early times, an assumption which is confirmed by the observations of the Cosmic Microwave Background. But looking at the sky today, we see structure on all scales - from planets and stars to galaxies, clusters of galaxies and enormous voids between them. The scenario which leads to these huge inhomogeneities is based on the simple gravitational instability, but the non linearity of the equations and the prodigious number of particles require using numerical simulations and a phenomenological approach. Indeed, knowing the basic equations does not mean understanding the complex physical processes deriving from them.

The idealized picture of galaxy formation in the standard cosmological model is a spherical infall of gas inside a dark-matter halo[14]. The standard lore was that the gas was first heated to the halo virial temperature behind an expanding virial shock, but Yuval Birnboim and Avishai Dekel showed in 2003 that below a critical mass, the virial shock in a galactic system is unstable and therefore often does not develop at all[1]. The resulting picture is that at high redshifts, galactic systems below the shock-heating mass scale will be comprised almost solely of cold gas, whereas above this scale a shock-heated gas extends out to the virial radius and cold, dense streams of gas fall along all the way down to the central galactic disk[3, 5, 15]. During my internship, I worked under the supervision of Avishai Dekel in the Racah Institute of Physics at the Hebrew University of Jerusalem, being part of his team working on the cold streams. This team comprises PhD students and postdocs (Yuval Birnboim, Elad Zinger, Noam Libeskind, Joanna Woo, Tobias Goerdt) as well as undergraduate students (Giora Engel, Michael Mumcuoglu, Barak Einav) and combines theoretical work with simulation and data analysis. Besides reading about galaxy formation and cosmology, my first task was to extract data from the MareNostrum simulation, aiming at highlighting the cold flows, and it is finally with this data and using Matlab that I worked during my whole internship. The results of this work were largely used in a team article submitted to *Nature* towards the end of my internship: *Massive galaxy formation by cold streams*[4], available in the appendix section. The team work and the frequent seminars were very stimulating and enabled me to keep in mind the more general frame in which my work was embedded ; during my internship, I was also able to attend a class of *Advanced Cosmology* on structure formation in the universe by Avishai Dekel and to listen to world leading cosmologists during a workshop which took place in June.

# 1 Formation of structure in the standard model of cosmology

## 1.1 The $\Lambda$ CDM model

### 1.1.1 A Friedmann-Lemaître model

The first cosmological model based on general relativity was proposed in 1917 by Albert Einstein, who was prejudiced to believe in a perfectly static universe without beginning or end. More generally, the Einstein equations of general relativity relate the structure of space-time with its mass and energy contents: gravitational fields intrinsically affect the curvature of space-time. Consequently, the matter distribution of the universe determines its global geometry. The more general form of these tensorial equations can be written as:

$$G^{\mu\nu} = E^{\mu\nu} + \Lambda g^{\mu\nu}$$

where  $G^{\mu\nu}$  is a tensor related to the distribution of matter, the Einstein tensor  $E^{\mu\nu}$  is related to the Riemann tensor which itself describes the curvature of space-time, and the last term proportional to the metric  $g^{\mu\nu}$  implies a cosmological constant  $\Lambda$ . This tensorial equation leads to ten non linear scalar equations and implies the local conservation of energy. A non zero cosmological constant was initially introduced by Einstein to allow a static universe, but was later removed as Edwin Hubble confirmed that our universe was not static, but expanding. The cosmological constant was then abandoned, until recent observations reintroduced it.

The basic assumption in cosmology is the cosmological principle: the universe is assumed to be homogeneous and isotropic on large scales. There is no preferred place to observe the laws of nature, which are assumed to be the same everywhere and at all times, and at very large scales the universe is smooth. Other assumptions arise when using general relativity: space-time should be simply connected (it could be filled with observers), locally flat (special relativity is locally valid) and there should be a means to synchronize all clocks in space.

The structure of space-time can be generally described by its metric, which is a quadratic form analog to distance in an Euclidean space. Assuming a homogeneous and isotropic universe, the Einstein equations of general relativity lead to the Friedmann-Lemaître-Robertson-Walker metric as the metric of the universe, which can be written in spherical coordinates  $(r, \theta, \phi)$

$$ds^2 = -c^2 dt^2 + a(t)^2 \left( \frac{dr^2}{1-kr^2} + r^2 d\Omega^2 \right)$$

where  $k$  describes the spatial curvature and is constant in time,  $a(t)$  is the *scale factor*, explicitly time dependent and expressing the relative expansion or compression of the universe, and  $d\Omega^2 = d\theta^2 + \sin^2\theta d\phi^2$ . In an expanding universe, physical distances will expand proportionally to  $a(t)$  and it is therefore current to express the metric in *comoving coordinates*  $d\xi = cdt/a(t)$ :

$$ds^2 = -c^2 dt^2 + a(t)^2 (d\xi^2 + S_k(\xi) d\Omega^2)$$

$$\text{where } S_k(\xi) = \begin{cases} \sin(\xi) & \text{if } k = +1 \\ \xi & \text{if } k = 0 \\ \sinh(\xi) & \text{if } k = -1 \end{cases}$$

The resulting equations in the case of an homogeneous and isotropic universe are called the Friedmann equations:

$$H^2 \equiv \frac{\dot{a}^2}{a^2} = \frac{8\pi G}{3} \rho - \frac{kc^2}{a^2} + \frac{\Lambda c^2}{3}$$

$$2\frac{\ddot{a}}{a} + \frac{\dot{a}^2}{a^2} = -\frac{8\pi G}{c^2} P - \frac{kc^2}{a^2} + \Lambda c^2$$

These equations are the basis of the different models for the universe, as they give the evolution of the scale factor as a function of time. Even if the real universe is not rigorously homogeneous and isotropic, the Friedmann-Lemaître-Robertson-Walker model is used as a first approximation to describe the evolution of the real universe. Different parameters are involved in these equations, such as the curvature  $k$  whose values are taken from  $\{-1, 0, +1\}$  or the cosmological constant  $\Lambda$ . The first Friedmann equation can be rewritten in terms of density parameters

$$H^2/H_0^2 = \Omega_{r,0}a^{-4} + \Omega_{m,0}a^{-3} + \Omega_{k,0}a^{-2} + \Omega_{\Lambda,0}$$

where  $\Omega_{m,0} \equiv \rho_{m,0}/\rho_c$  is the actual matter density parameter, defined as the ratio of the actual matter density  $\rho_{m,0}$  to the critical density of an Einstein-de Sitter universe (no curvature, no cosmological constant)  $\rho_c = 3H_0^2/8\pi G$ ,  $\Omega_{r,0} \equiv \rho_{r,0}/\rho_c$  is the radiation density today,  $\Omega_{k,0} \equiv -kc^2/H_0^2$  is the spatial curvature density today and  $\Omega_{\Lambda,0} \equiv \Lambda c^2/3H_0^2$  is linked to the value of the cosmological constant today (often assimilated as a vacuum density). These quantities are some of the cosmological parameters which determine a cosmological model and the properties of the universe, as its mode of expansion. Recent observation programs have placed severe constraints on the cosmological parameters, leading to the emergence of the  $\Lambda$ CDM cosmology as the standard cosmological model.  $\Lambda$ CDM stands for  $\Lambda$ -Cold Dark Matter, as that Friedmann-Lemaître-Robertson-Walker model assumes the existence of a cosmological constant and of cold dark matter. It is a Big Bang model where the expansion is even accelerated. Some of the parameters of the  $\Lambda$ CDM cosmology, assuming no spatial curvature  $\Omega_k = 0$ , are listed in Table 1: these values have been obtained with the data of the Wilkinson Microwave Anisotropy Probe (WMAP), combined with the Sloan Digital Sky Survey (SDSS) and supernovae data. The errors quoted are  $1\sigma$ : there is statistically a 68% likelihood that the true value falls within the upper and lower error bounds.

Parameter	Value	Description
$H_0$	$73.2^{+3.1}_{-3.2} \text{ km s}^{-1}\text{Mpc}^{-1}$	Hubble parameter
$\Omega_{m,0}$	$0.266^{+0.025}_{-0.040}$	Total matter density (baryons and dark matter)
$\Omega_{b,0}$	$0.0444^{+0.0042}_{-0.0035}$	Baryon density
$\Omega_{\Lambda,0}$	$0.732^{+0.040}_{-0.025}$	Dark energy density
$t_0$	$13.7^{+0.13}_{-0.17}\text{Gyr}$	Age of the universe

Table 1: Some parameters of the  $\Lambda$ CDM cosmology

### 1.1.2 Cold dark matter and a cosmological constant

The  $\Lambda$ CDM model assumes the existence of a cold, non baryonic dark matter. The observed phenomena which lead to the assumption of the existence of this dark matter were the radial velocities of stars and gas in galaxies. Indeed, Newtonian dynamics relate the rotation velocity of an object around a central mass to the distance between the two objects and to the mass of the central one. As he was trying to determine the mass of the Coma cluster in 1933, the Swiss astronomer Fritz Zwicky was surprised to find that 100 to 500 times more mass than observed would be needed to explain the high values of the rotation velocities. The same phenomenon was later observed by Sinclair Smith in 1936 for the Virgo cluster, but the problem did not trigger interest at that time. It reappeared in the seventies when the American astronomer Vera Rubin studied the rotation of spiral galaxies: stars far from the center of the galaxy seemed to be rotating so fast that the rotation curve of most spiral galaxies was flat. According to Newtonian dynamics, the rotation velocity should decrease when moving away from the center of the galaxy, as most of the visible matter is concentrated around the center. As the density decreases approximately exponentially from the center, the velocity of the stars in the spiral arms of the galaxy should also decrease exponentially, which is not observed.

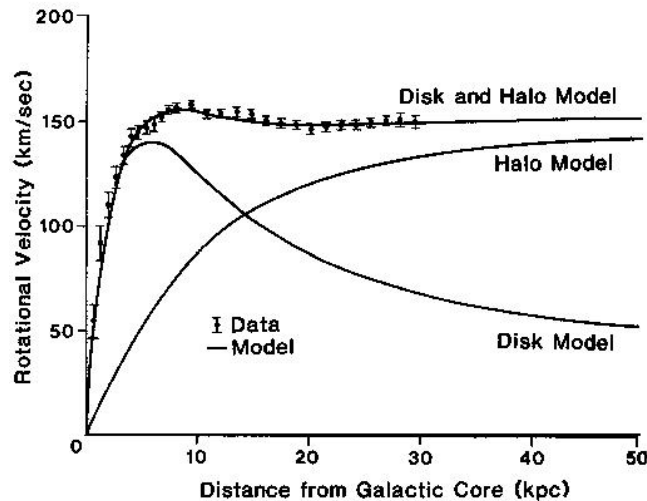


Figure 1: The rotation velocity of stars within a galaxy is not compatible with a simple disk model induced by the luminous matter distribution. Assuming the existence of a dark matter halo surrounding the disk permits to fit the observations.

To explain the dynamics of these galaxies, one could imagine the existence of a halo made of non visible matter in which the visible matter would be embedded and whose mass would be more than five times higher than the mass of the visible matter. For a few years, this dark matter was expected to be constituted of ordinary baryonic matter, like asteroids, extrasolar planets or neutron stars. But later studies have shown that it is not possible: the Big Bang theory precisely predicts the quantity of baryons present at the first epochs of the universe and dark matter has therefore to be explained with a different type of matter. The first candidates were neutrinos, which are neutral particles weakly interacting with ordinary matter. But we now know that their mass would have been too small to explain the masses of galactic haloes and their velocities too big to enable haloes to form: the high velocities of this “warm dark matter” would have dispersed the little primordial inhomogeneities which then led to the formation of galaxies and clusters of galaxies. It is for this reason that most of the dark matter has to be “cold”, which means that its mean velocity at the first stages of cosmic history was much smaller than the speed of light. Particle physicists are researching such a particle, which would weakly interact with ordinary matter and would be much more slower and massive than the neutrino. Some extensions of the standard model of particle physics, as supersymmetry, offer possible candidates named WIMPS (*Weakly Interacting Massive Particles*): these particles would only interact through weak and gravitational interactions. Experiencing no electromagnetic interaction, we would not be able to detect them directly and their indifference to the strong nuclear interaction prevent them to react with atomic kernels. Within the supersymmetric theory, the neutralino would be a good candidate for dark matter: this particle would be the fermionic superpartner of both the photon (boson which transmits the electromagnetic force) and the  $Z^0$  boson (which transmits the weak nuclear interaction). The neutralino would be more massive than all known particles but the lightest supersymmetric particle, which would assure its stability.

Even if the  $\Lambda$ CDM model seems to be the most accurate model to describe our universe nowadays, dark matter has not been directly detected. The assumption of its existence is not the only possible answer to the incompatibility between the observed galactic orbits and newtonian predictions: the israeli physicist Mordechai Milgrom proposed in 1983 to modify Newton’s law of gravity[6]. This was the starting point of the MOND theory (*Modified Newtonian Dynamics*), which explains extremely well the rotation curves of galaxies without dark matter. But even with its successes, the absence of an underlying theory which would explain the modification of Newton’s law prevents it to be a fully convincing model.

Recent measurements of the velocities of distant (high redshift) objects have shown that the Hubble constant was lower earlier in the history of the universe: the expansion of the universe is accelerating[12]. This can be only achieved with a non zero positive cosmological constant. This constant arises as a property of the structure of space-time itself, as if it had an intrinsic repulsive action. The energy related to this property is referred as *dark energy* and constitutes as much as 70% of the energy distribution of our universe.

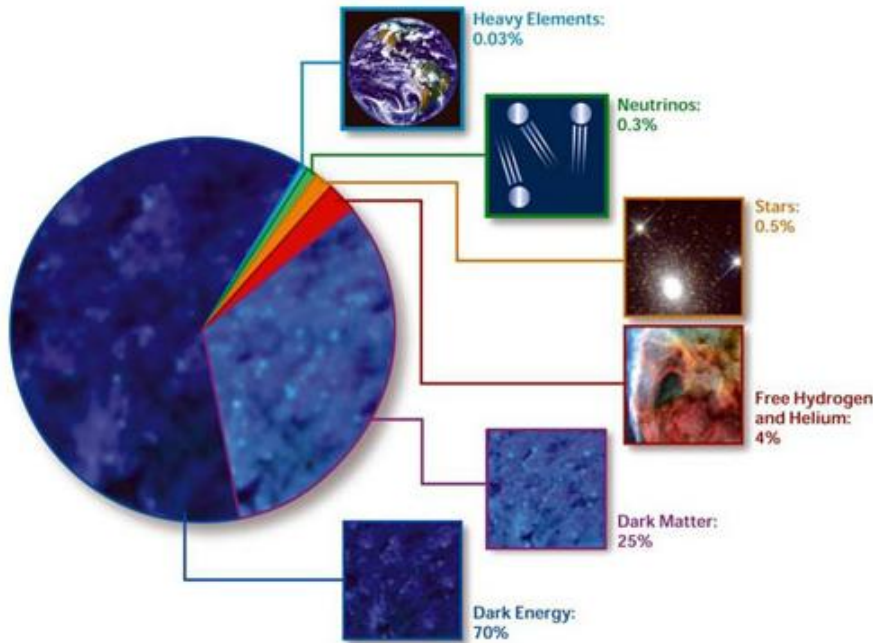


Figure 2: The composition of the universe: stars and visible matter are responsible for only 0.5% of the total mass, whereas ordinary baryonic dark matter reaches 5% of the mass of the universe. Neutrinos constitute a warm dark matter but their low masses reduce their contribution to a few tenth of percents: a cold dark matter dominates the matter distribution (25% of the mass of the universe). When dark energy is added to the total mass-energy of matter (baryons and dark matter), the total energy density is consistent with what is needed to make the universe flat ( $\Omega_{k,0} = 1 - \Omega_{m,0} - \Omega_{\Lambda,0} = 0$ ). <http://www.lsst.org/Science/darkenergy.shtml>

### 1.1.3 A scenario for the early history of the universe

The basic process involved in galaxy formation is the gravitational instability: a local excess of matter will attract the neighboring matter due to its gravitational potential and will be amplified that way. In the standard cosmological model, density fluctuations were created very early in the history of the universe and later condensed to form the structured objects we now see. Extrapolating the laws of physics indicates that at the time of the Big Bang, around 13.7 Gyr ago, the distances between the now visible objects were close to zero and temperature and density were infinite. Quantum fluctuations at the very first moments were the seeds for the future growth of structure in the universe. As the nascent universe passed through a phase of exponential expansion driven by a negative-pressure vacuum energy density, called *inflation*, these microscopic fluctuations were magnified to cosmic size. Within this model, cosmic inflation lead to fluctuations described by a Gaussian random field with a nearly scale invariant spectrum (Harrison-Zel'dovich spectrum). As the universe expanded, temperature decreased and formation of structured matter became possible. At that time, the universe was still opaque: there was an equilibrium between matter and radiation, as free electrons ceaselessly absorbed and re-emitted photons. As the universe continued to cool, electrons had no longer enough energy to overcome the attractive force of atomic nuclei, and became bound to atoms. Light could now stream forth unimpeded. This process is called *recombination*, and the “first light” enabled to stream is what we now see as the Cosmic Microwave Background Radiation.

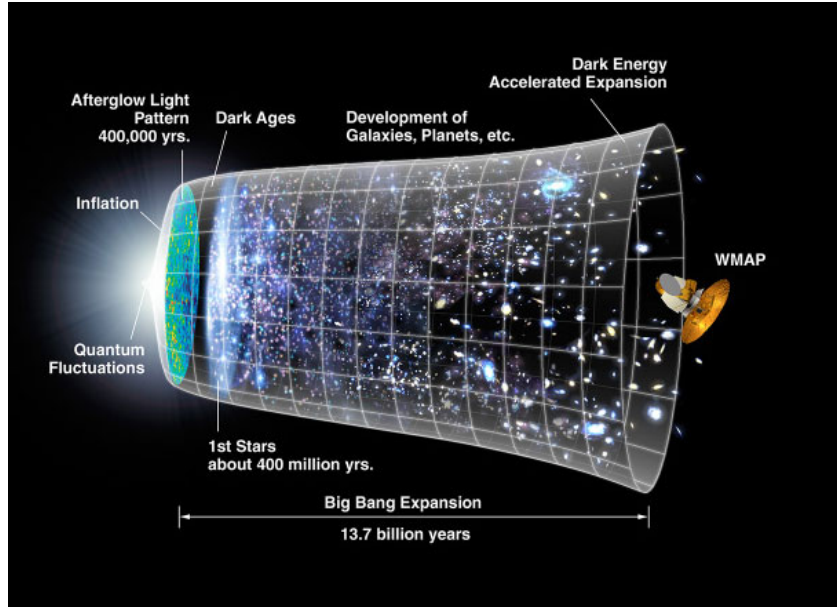


Figure 3: The recent WMAP observations lead by NASA probed the Cosmic Microwave Background and gave evidence in favor of the standard model of cosmology, and especially of the cosmic inflation model. [http://map.gsfc.nasa.gov/m\\_ig/060915/CMB\\_Timeline150.jpg](http://map.gsfc.nasa.gov/m_ig/060915/CMB_Timeline150.jpg)

## 1.2 The formation of structures

### 1.2.1 The principal mechanism: gravitational instability in an expanding universe

Formation of structures is essentially driven by the competition between the gravitational growth of fluctuations and the expansion of the universe, which tends to dilute each local overdensity.

The first study of the gravitational instability was carried by the british physicist James Jeans in 1902: his theory took into account gravity and pressure and assumed a static medium. Gravity tends to condense matter, whereas pressure diminishes inhomogeneities: the more the mass of a fluctuation, the more gravity is important compared to pressure. The system is described by the following set of fluid equations:

$$\begin{cases} \dot{\rho} + \vec{\nabla}_{\vec{r}}(\rho\vec{v}) = 0 & \text{Continuity equation} \\ (\partial\vec{v}/\partial t)_{\vec{r}} + (\vec{v}\cdot\vec{\nabla}_{\vec{r}})\vec{v} = -\vec{\nabla}_{\vec{r}}\Phi - \vec{\nabla}_{\vec{r}}(P)/\rho & \text{Euler equation} \\ \nabla_{\vec{r}}^2\Phi = 4\pi G\rho & \text{Poisson equation} \end{cases}$$

where  $\rho$  is the local density,  $\vec{v} = \dot{\vec{r}}$  where  $\vec{r}$  is the physical space coordinate,  $\Phi$  is the gravitational potential and  $P$  the pressure. Taking the expansion of the universe into account and assuming a uniform background, we switch to comoving coordinates  $\vec{x} = \vec{r}/a(t)$  where  $a(t)$  is the scale factor of the universe, and we write  $\rho(t, \vec{r}) = \rho_u(t)[1 + \delta(t, \vec{x})]$  where  $\rho_u(t)$  is the mean density of the universe at time  $t$  and  $\delta(t, \vec{x})$  the overdensity at the same time at a specified position. To describe the global behaviour of the universe, we use the Friedmann equations and assume an Einstein-de Sitter universe (which is a good approximation for early times).

After the inflation period, the fluctuations are small enough to use a linear approximation: assuming that  $\delta \ll 1$ ,  $\nabla\delta \ll 1$  and  $v \ll 1$ , we obtain the following equation for  $\delta$ , where  $c_s^2 = \partial P/\partial\rho$  is the sound speed[9]:

$$\ddot{\delta} + 2H\dot{\delta} = 4\pi G\rho_u\delta + a^{-2}c_s^2\nabla^2\delta$$

The right side of this equation shows the competition between gravity and pressure, whereas in the left side, the Hubble flow seems to slow down as a friction force, which is an artifact of the comoving coordinates.

The first stage of the fluctuation growth can be described by the linear approximation, but this approximation becomes inaccurate when fluctuations have developed up to  $\delta \geq 1$  and to even higher values, as we observe today in galaxies. The linear phase leads to a non linear phase whose analytic treatment is more difficult and requires additional assumptions or a statistical approach.

### 1.2.2 Hierarchical clustering

Instead of using the spatial distribution of the overdensity  $\delta(t, \vec{x})$ , we consider its Fourier transform  $\delta_{\vec{k}}(t)$  and define the power spectrum as its variance  $\langle |\delta_{\vec{k}}|^2 \rangle$ . The evolution of the power spectrum of the fluctuations depends on the properties of matter: if matter would have been mostly constituted of adiabatic baryons or hot dark matter (neutrinos), the spectrum would have been cut for small scales and galaxies would have formed by fragmentation of huge structures[2]. But in the  $\Lambda$ CDM model, most of the matter is assumed to be made of cold dark matter: galaxies formed within the potential wells of the dark matter haloes[14]. As dark matter does not lose its energy by radiation, it can't condense as efficiently as baryonic matter and is organised in more diffuse haloes in which ordinary matter is embedded. In the case of cold dark matter, small structures form first and larger structures form by successive mergers: this is the hierarchical scenario. Galaxy formation is not a unique event but a continuous hierarchical process where small galaxies assemble to form bigger ones through successive mergers. Collisions and close interactions between galaxies lead to tidal forces which distort and strip the galaxies: their morphology is not fixed and evolves with the influences of the environment and of the successive mergers.

In cosmological simulations, we can define for each dark matter halo its progenitors and follow its formation back in time through *merger trees*[13]. The Extended Press-Schechter theory (EPS) gives the conditional probability for a halo of a given mass to have a progenitor of another given mass and a formula for the flux around a galaxy depending on its mass.

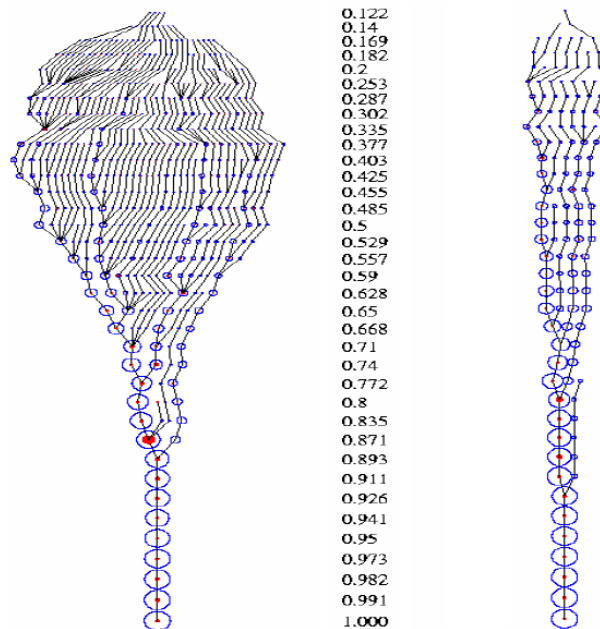


Figure 4: Example of merger trees for two galaxies: whereas the left one underwent several major mergers, in which two galaxies of about the same mass merge, the right was mainly formed by smooth accretion. The number of progenitors which are followed is determined by the mass resolution we chose: the merger trees could have continued further up.



But galaxy formation is not limited to the merging processes of dark matter haloes: intricate gas processes affect galaxy morphology and structure. Within haloes, ordinary matter cools, losing energy by radiation, and falls to the center of the potential well. Due to the conservation of the momentum, the gas velocity increases when falling inwards and the centrifugal force can lead to the formation of a disk perpendicular to the initial rotation axis of the halo. Violent mergers can interfere with the smooth accretion of gas within the halo and brutally bring their own mass and angular momentum to the halo. At the center of the potential well, gas is able to fragment to form stars. At the end of their evolution, most massive stars explode and eject their gas and the heavy elements formed at their center in the interstellar medium. This feedback process, but also the activity of some galactic nuclei (*AGN - Active Galactic Nuclei*) can produce powerful galactic winds which reduce the size of the galaxies and inhibit new star formation.

### 1.3 The MareNostrum simulation

#### 1.3.1 The MareNostrum supercomputer

The different processes involved in galaxy formation can be implemented in numerical simulations. The MareNostrum galaxy formation project is a multidisciplinary collaboration between astrophysicists of France, Germany, Spain, Israel and the United States, together with computer experts from IDRIS (Institut du Développement et des Ressources en Informatique Scientifique) and BSC (Barcelona Supercomputing Center). The application solves a very complex set of mathematical equations by translating them into sophisticated computational algorithms. These algorithms are based on state-of-the-art adaptive mesh refinement techniques and advanced programming technologies in order to optimize the timely execution of the same application on several thousands of processors in parallel. This requires the combined power of 2048 PowerPC 970 MP processors and up to 3.2 TB of RAM memory. Contrary to other large computational problems in which information can be split into independent tasks, and because of the non-local nature of the physical processes, all 2048 processors have to exchange large amounts of data very frequently. A personal computer, provided it had enough memory to store all the data, would need around 114 years to do the same task.



Figure 5: The MareNostrum computer in Barcelona is one of the most powerful of the world with its 10240 processors. Ironically located inside an old chapel, it is the perfect place to compute the formation and evolution of a virtual replica of our own universe. *Courtesy of Barcelona Supercomputing Center*

### 1.3.2 A cosmological N body and hydrodynamics simulation

The MareNostrum simulation is a cosmological N body and hydrodynamics simulation with most of the processes involved in galaxy formation theory. The main asset of the MareNostrum project relies on using a quasi exhaustive number of physical ingredients that are part of the current theory of galaxy formation, and at the same time covering a large enough volume to provide a fair sample of the universe, especially at redshift above one. Metal dependent cooling and UV heating, as well as a simple model for supernovae feedback and metal enrichment have been incorporated in the simulation. A polytropic equation of state has been used to describe the high density regions and star formation is included. The simulation was started with a base grid of  $1024^3$  cells and the same number of dark matter particles for a simulation box of  $50 h^{-1}\text{Mpc}$  and a spatial resolution of about  $1 h^{-1}\text{kpc}$  in physical units. The grid was progressively refined, on a cell-by-cell basis, when the local number of particles exceeded 10 according to the RAMSES Adaptive Mesh Refinement (AMR) code [11, 8]. AMR permits to focus on high density regions and to permanently adapt the grid to the complex flows. Periodic boundary conditions are used to simulate an infinite volume.

The simulation was run for a  $\Lambda\text{CDM}$  universe with  $\Omega_m = 0.3$ ,  $\Omega_\Lambda = 0.7$ ,  $\Omega_b = 0.045$ ,  $H_0 = 70 \text{ kms}^{-1}\text{Mpc}^{-1}$  and the amplitude of mass fluctuations on 8 Mpc scale  $\sigma_8 = 0.9$ . The simulation was momentarily stopped at redshift  $z \approx 1.5$  because of insufficient allocated time. At the end of the simulation, the total number of AMR cells was above  $5.10^9$ .

### 1.3.3 Available data

The data of the MareNostrum simulation is stored in a computer at the *Institut d'Astrophysique* in Paris from which we are able to download. In order to analyze the physical properties around high redshift galaxies, a Friend-Of-Friend (FOF) catalog is available for each snapshot. This catalog lists the position and the number of dark matter particles for each halo of the specified output, each halo being delimited by a FOF algorithm. We are able to download cubes for different physical quantities: density, pressure, metallicity and the three components of the velocity. The size of the cubes and their resolution can be chosen at will, but as the physical resolution is about  $1 h^{-1}\text{kpc}$ , it is irrelevant to chose a grid cell whose size is smaller than the corresponding comoving length. For output 75, corresponding to redshift  $z = 2.46$ , the highest resolution is resolution 14 - where each grid cell has a size of  $50\,000/2^{14} = 3.05 \text{ kpc}/h$  comoving, that is to say  $1.26 \text{ kpc}$  physical.

Centering is an important issue: from the FOF catalog, we have access to the position of the center of the dark matter halo, which does not necessarily corresponds to the center of the gas density. To define the gas center, we smooth the density field at resolution 13 with a gaussian filter and search the highest value of the smoothed density. The width of the gaussian filter is chosen to cover about 5 grid cells, which corresponds to  $12.6 \text{ kpc}$  physical - a typical size for the radius of a galaxy (the radius of the Milky Way is about  $15 \text{ kpc}$ ). We then download the recentered cubes at resolution 14.

For each halo, we compute the virial mass  $M_{vir}$  and the virial radius  $R_{vir}$ , which is defined as the radius of the sphere centered on the halo within which the average density is greater than the critical density by a specified factor (depending on  $\Omega_m$ , but close to 200). Different virial quantities can be derived from the virial radius and the virial mass, as the virial velocity or the virial density and eventually used to normalize the different physical quantities. The units used in the simulation are not directly meaningful, as they are redefined at each time step to fit the refinement: for each output different density, length and time multiplicative factors permit to obtain cgs units. For each halo, we redefine the velocity as the center of mass velocity and we compute different physical quantities deriving from density, pressure and velocity (see Table 2). Table 3 shows the panel of downloaded haloes during my internship: we focused on redshift  $z \approx 2.5$  and haloes of mass  $M_{vir} \approx 10^{12} M_\odot$ .

Density	$\rho$
Pressure	$P$
Velocity	$\vec{v}$
Metallicity	$Z$
Radial velocity	$v_r \equiv \vec{v} \cdot \vec{r} / r$
Radial flux per solid angle	$\dot{m} \equiv r^2 \rho v_r$
Temperature	$T \equiv \frac{\mu m_p}{k_B} \frac{P}{\rho}$
Entropy	$K \equiv \frac{k_B}{\mu m_p} \frac{T}{\rho^{2/3}}$
Sound speed	$c_s \equiv \left(\frac{5}{3} \frac{P}{\rho}\right)^{1/2}$
Radial Mach number	$M_r \equiv v_r / c_s$

Table 2: Physical quantities available from the MareNostrum simulation for each grid cell.  $m_p$  refers to the proton mass,  $\mu$  is the mean molecular weight of the gas or plasma in units of  $m_p$ , considered to be equal to 0.59, and  $k_B$  refers to the Boltzmann constant.

	$z = 1.57$	$z = 2.46$	$z = 4.01$
$M_{vir} \approx 10^{11} M_\odot$		7	
$M_{vir} \approx 10^{12} M_\odot$	8	12	8
$M_{vir} \approx 10^{13} M_\odot$		12	

Table 3: The panel of downloaded haloes during my internship: the figure lists the number of haloes at specified redshifts and halo masses. We focused on redshift  $z \approx 2.5$  and haloes of mass  $M_{vir} \approx 10^{12} M_\odot$ .

## 2 Cold flows in the MareNostrum simulation

### 2.1 Shock heated gas and cold flows

#### 2.1.1 The standard picture of infall to a disk

The standard picture of disk formation assumes that while a dark matter halo relaxes to a virial equilibrium, the gas that falls in within it is shock-heated near the halo virial radius to the halo virial temperature.

Initial density perturbations are assumed to grow by gravitational instability, reach maximum expansion, and collapse into virial equilibrium at roughly half the maximum expansion radius. During the initial phase, and roughly until shells start crossing each other near the virial radius  $R_{vir}$ , the gas pressure is negligible compared to the gravitational force, so the shells of gas and dark matter move in a similar manner. Once interior to the virial radius, where shells tend to cross and the gas density becomes high enough, the gas pressure becomes an important player in the dynamics. Its hydrodynamic properties allow transfer of bulk kinetic energy into internal energy and the pressure prevents gas elements from passing through other gas elements and from being compressed without limit. This makes the infall velocity vanish at the center. Since in the cold infalling gas the typical velocity is higher than the speed of sound, the information about this inner boundary condition cannot propagate outwards in time, and these supersonic conditions create a shock. After the gas crosses the shock, it is heated up, the speed of sound increases, and the flow becomes subsonic. The shock transfers the kinetic energy that has been built during the collapse into internal gas energy just behind the shock. A stable spherical shock would slowly propagate outwards through the infalling gas, leaving behind it hot, high-entropy gas that is almost at rest. The temperature of the post-shock gas roughly equals the virial temperature.

#### 2.1.2 Stability of the virial shock

The persistence of the shock depends on sufficient pressure by the post-shock gas, which supports it against being swept inwards due to the gravitational pull together with the infalling matter. Radiative gas cooling makes the gas lose entropy and pressure, which weakens the pressure support behind the shock front. Yuval Birnboim and Avishai Dekel analyzed the stability of the virial shock in 2003, both numerically and analytically [1, 3].

One dimensional spherical simulations without metallicity permitted to follow the evolution of the radii of Lagrangian gas shells in a spherical gravitating system consisting of gas and dark matter. The initial density fluctuation was coherent with the  $\Lambda$ CDM model, gas was assumed to be cooling radiatively and the collapse of each gas shell was stopped at roughly  $0.05R_{vir}$  by an artificial centrifugal force which mimicked the formation of a central disc. The results of these simulations are presented in Fig. 6: it shows that a strong shock exists near the virial radius for massive haloes of mass  $\sim 10^{12}M_{\odot}$ , as expected in the common picture. The virial shock gradually propagates outwards, encompassing more mass in time. But for lower masses, a stable shock forms and inflates from the disk towards the virial radius only after a total mass of more than a few times  $10^{11}M_{\odot}$  has collapsed.

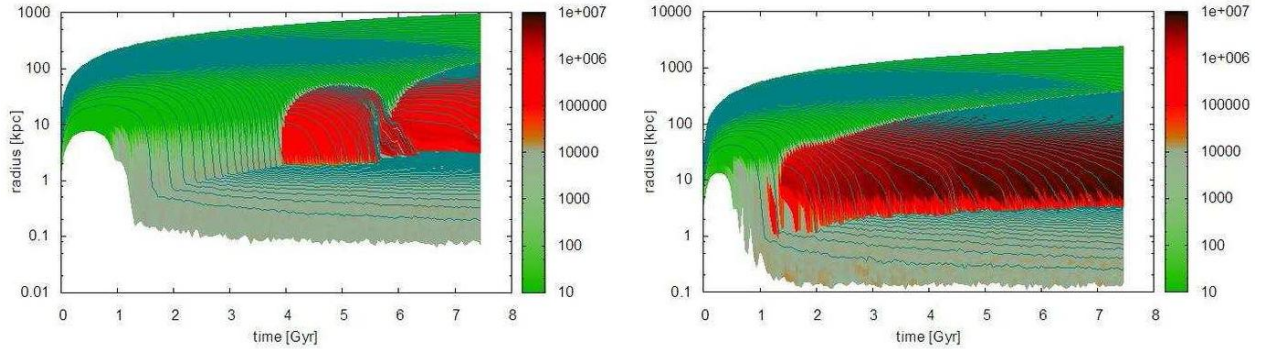


Figure 6: Time evolution of the radii of Lagrangian gas shells in a spherical simulation of a protogalaxy consisting of primordial gas (metallicity  $Z = 0$ ) and dark matter[3]. Lines represent different gas shells and temperature is marked by color. A shock shows up as a sharp break in the flow lines, namely a sudden slowdown of the infall, associated with an abrupt increase in the temperature. The lower discontinuity marks the “disk” radius due to an artificial centrifugal force. The figure to the right shows a massive system where the virialized mass grows from  $10^{11}$  to  $10^{13}M_{\odot}$  whereas in the left one, the virialized mass grows from  $10^{10}$  to  $10^{12}M_{\odot}$ . A virial shock exists only in systems more massive than a critical mass, while in smaller haloes the gas flows cold and unperturbed into the inner halo[3].

The existence or absence of a shock, as seen in the simulations, can be evaluated via an analysis of the post-shock gas[1]. The condition for the existence of a stable shock can be derived from the balance between the pressure in the post-shock gas and the gravitational attraction towards the halo center. For an ideal gas, the pressure is expressed in the equation of state  $P = (\gamma - 1)\rho e$  where  $\rho$  is the gas density and  $e$  the specific internal energy. The adiabatic index  $\gamma$  has a value of  $5/3$  for a mono-atomic gas such as ionized hydrogen.

If there is no cooling in the gas, the stability criterion is the standard Jeans stability criterion,  $\gamma > 4/3$  in the adiabatic case. Generalizing the definition of the adiabatic index  $\gamma = (\partial \ln P / \partial \ln \rho)_S$ , we define the new quantity along the particle trajectories

$$\gamma_{eff} \equiv \frac{\partial \ln P}{\partial \ln \rho} = \gamma - \frac{\rho}{e} \frac{q}{\dot{\rho}}$$

where  $q$  is the radiative cooling rate and the second equality follows from energy conservation  $\dot{e} = -P\dot{V} - q$  plugged into the equation of state, where  $V = \rho^{-1}$  is the specific volume. The quantity  $\gamma_{eff}$  deviates from the adiabatic index by a term which is the ratio between the characteristic rates of the two involved processes: the cooling rate  $q/e$  which reduces the pressure in the post-shock gas, and the compression rate  $\dot{\rho}/\rho$  which tends to increase the pressure.

A perturbation analysis on spherical shells results in a stability criterion of the form (with  $\gamma = 5/3$ ):

$$\gamma_{eff} > \gamma_{crit} \equiv \frac{2\gamma}{\gamma+2/3} = \frac{10}{7}$$

It is possible to express  $\gamma_{eff}$  in terms of characteristic timescales rather than rates. The cooling timescale is defined as  $t_{cool} \equiv e/q$  and the compression time as  $t_{comp} \equiv \Gamma\rho/\dot{\rho}$ , where  $\Gamma$  is a numerical factor chosen to have the stability criterion equivalent to  $t_{cool} > t_{comp}$ . The simple condition for an unstable shock is that the cooling rate has to be faster than the compression rate. If the cooling rate is slower, the compression in the gas will cause an increase in pressure which can then balance the loss of energy by radiative cooling and allow the post-shock gas to be stable against the global gravitational collapse and keep the shock supported. It is possible to restate the stability criterion in terms of pre-shock quantities of the gas and, by employing the virial relations in the  $\Lambda$ CDM cosmology, find a critical post-shock temperature with its halo virial velocity and consequently the critical halo mass for a stable shock  $M_{crit} \approx 6 \cdot 10^{11}M_{\odot}$ , largely independent of redshift. The implementation of this critical mass in cosmological simulations like GalICS permitted to fit observations much more accurately than before, especially it reproduced the observed bimodality of the distribution of galaxies[3].

### 2.1.3 Cold streams in a hot medium

This shock stability analysis lead to an new scenario for galaxy formation. Gas accreted to a galaxy below the mass threshold  $M_{crit}$  is never heated and remains cold. Once the mass of the galactic system reaches the critical mass, a stable virial shock forms and the subsequent evolution of the galaxy is in accordance with the “classic” spherical infall model. Nevertheless, simulations have shown that the gas could accrete onto a forming galaxy in two modes [5]: a conventional “hot mode”, which dominates the growth of high mass systems, and a “cold mode”, which is never heated above  $10^5\text{K}$ , dominates in low mass systems and is largely found along filaments. At high redshifts of  $z \gtrsim 2$ , one expects to find galactic systems containing hot gas in a virial shock punctured by cold dense streams. The resulting picture -summarized in Fig. 7- is that at high redshifts, galactic systems below the shock-heating scale will be comprised almost solely of cold gas, which falls to the center roughly spherically, whereas above this scale a shock heated gas extends out to the virial radius and cold, dense streams of gas fall along filaments all the way down to the central galactic disk. These filaments should carry more angular momentum than the shock-heated gas and the direct collapse of cold gas should affect the star formation rate and the morphology of galaxies[15, 4].

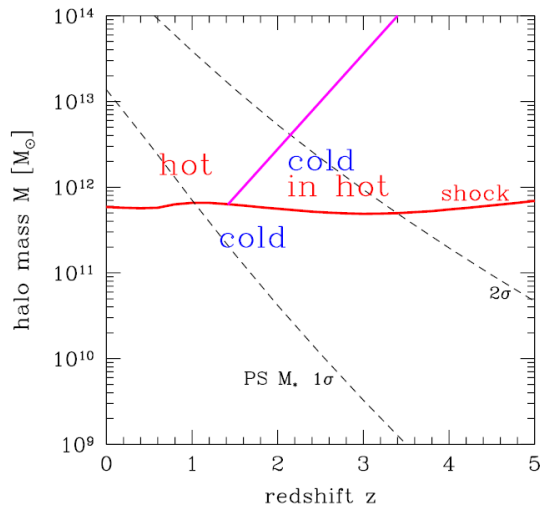


Figure 7: Analytic predictions for the regimes of cold streams and shock-heated medium in the plane of halo mass and redshift. The nearly horizontal curve is the robust threshold mass for a stable shock based on spherical infall analysis,  $M_{shock}(z)$ . Below this curve the flows are predicted to be predominantly cold and above it a shock-heated medium is expected to be present. The inclined solid curve is the conjectured upper limit for cold streams, valid at redshifts higher than  $z_{crit} \sim 2$ . The hot medium in  $M_{vir} > M_{shock}$  haloes at  $z > z_{crit}$  is predicted to host penetrating cold streams, while haloes of a similar mass at  $z < z_{crit}$  are expected to be all hot, shutting off most of the gas supply to the inner galaxy. The dotted lines correspond to the Press-Schechter mass function, which gives the typical mass of haloes as a function of redshift[3].

The reason for penetrating cold streams at high redshifts is that at early times, the haloes of  $M_{vir} > M_{shock}$  populate the extreme massive tail of the halo mass distribution. As such, they are fed by dark-matter filaments from the cosmic web that are narrow compared to  $R_{vir}$  and denser than the mean density within the halo. The enhanced density of the gas that streams along these filaments allows it to cool more rapidly than the dynamical compression rate behind a shock and thus avoid the shock heating that occurs elsewhere in the halo.

## 2.2 Highlighting the cold streams in the MareNostrum simulation

### 2.2.1 Different morphologies

To have a first idea of the galaxies extracted from the simulation, we can plot projected density and temperature along the directions of the cube: we just sum up the values along a specified direction. But instead of weighting temperature by volume, we weight it by mass, which is more accurate: more importance is given to the cells which contains more gas. The high density centers of the galaxies appear to be colder: at the center, gas cools to form a disk and stars.

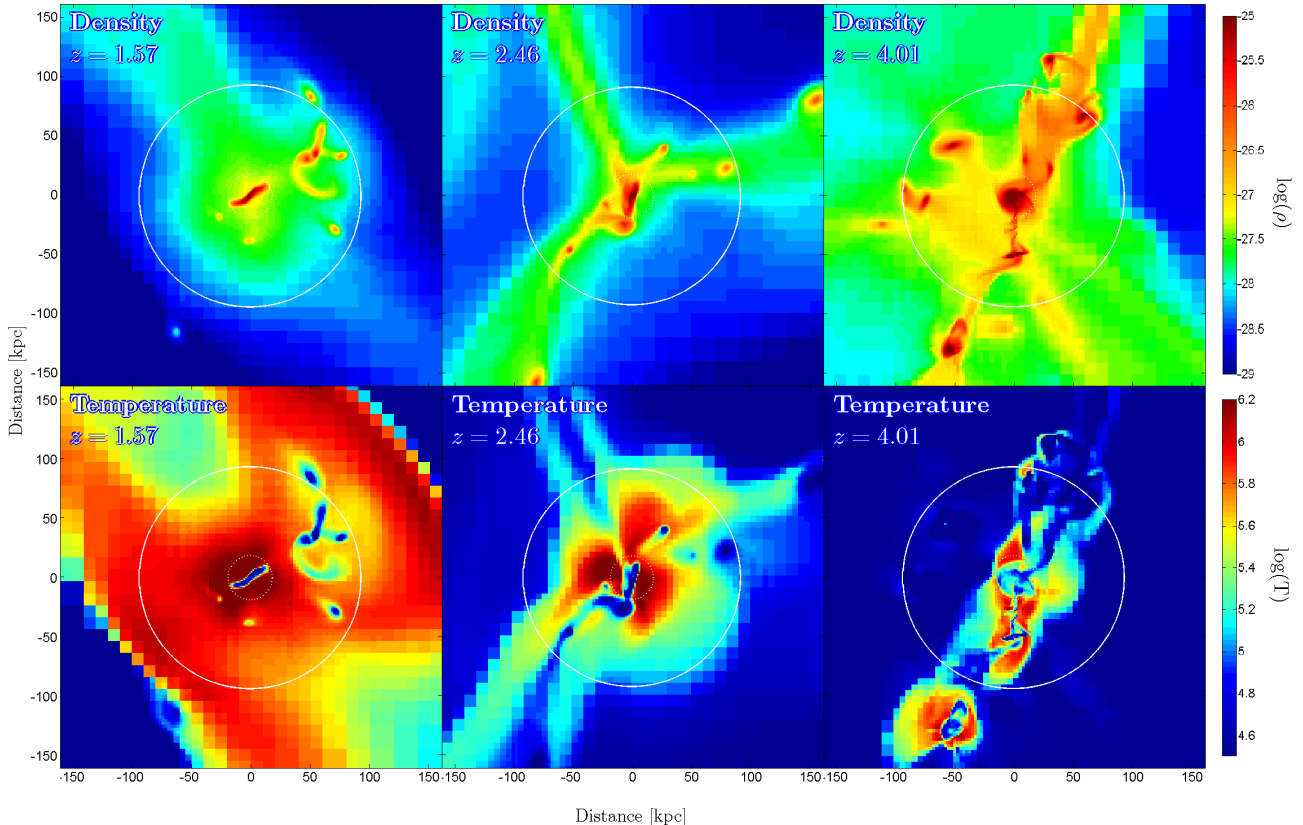


Figure 8: Maps of projected density and weighted temperature for typical  $M_{vir} \approx 10^{12} M_{\odot}$  haloes at different redshifts. The plain white circle indicates the virial radius  $R_{vir}$  of the halo whereas the dotted white circle indicates  $0.2 R_{vir}$ . At higher redshifts, thin filaments penetrate to the inner part of the halo, which is not the case at  $z = 1.57$ .

The maps of Fig. 8 show a typical halo of mass  $M_{vir} \approx 10^{12} M_{\odot}$  at redshifts 1.57, 2.46 and 4.01. A disk can be seen at each redshift in the central area, but the general structure of the halo and its satellites differs. We can clearly identify disk satellites and tidal tails provoked by the gravitational field of the central galaxy. The halo at redshift 1.57 is all hot, which is not the case at higher redshift, where cold streams penetrate the shock-heated gas. The critical mass for the existence of a virial shock without cold streams seems to increase with redshift: while at redshift 4.01 and even 2.46, clear filaments are streaming into the inner halo, the  $z = 1.57$  halo lies at the center of a hot bubble with no apparent filaments inside the virial radius. At high redshift, an accretion shock coexists with cold streams coming from the outer parts of the halo.

Fig. 9 clearly shows the development of a virial shock when the mass grows: no shock is observed for  $M_{vir} \approx 10^{11} M_{\odot}$ , a shock is developing from the disk in the second  $M_{vir} \approx 10^{12} M_{\odot}$  halo and at  $M_{vir} \approx 10^{13} M_{\odot}$  the virial shock encompasses the whole halo, without any penetrating cold filaments. These results are perfectly coherent with the predictions of Dekel & Birnboim (2006) shown in Fig. 7.

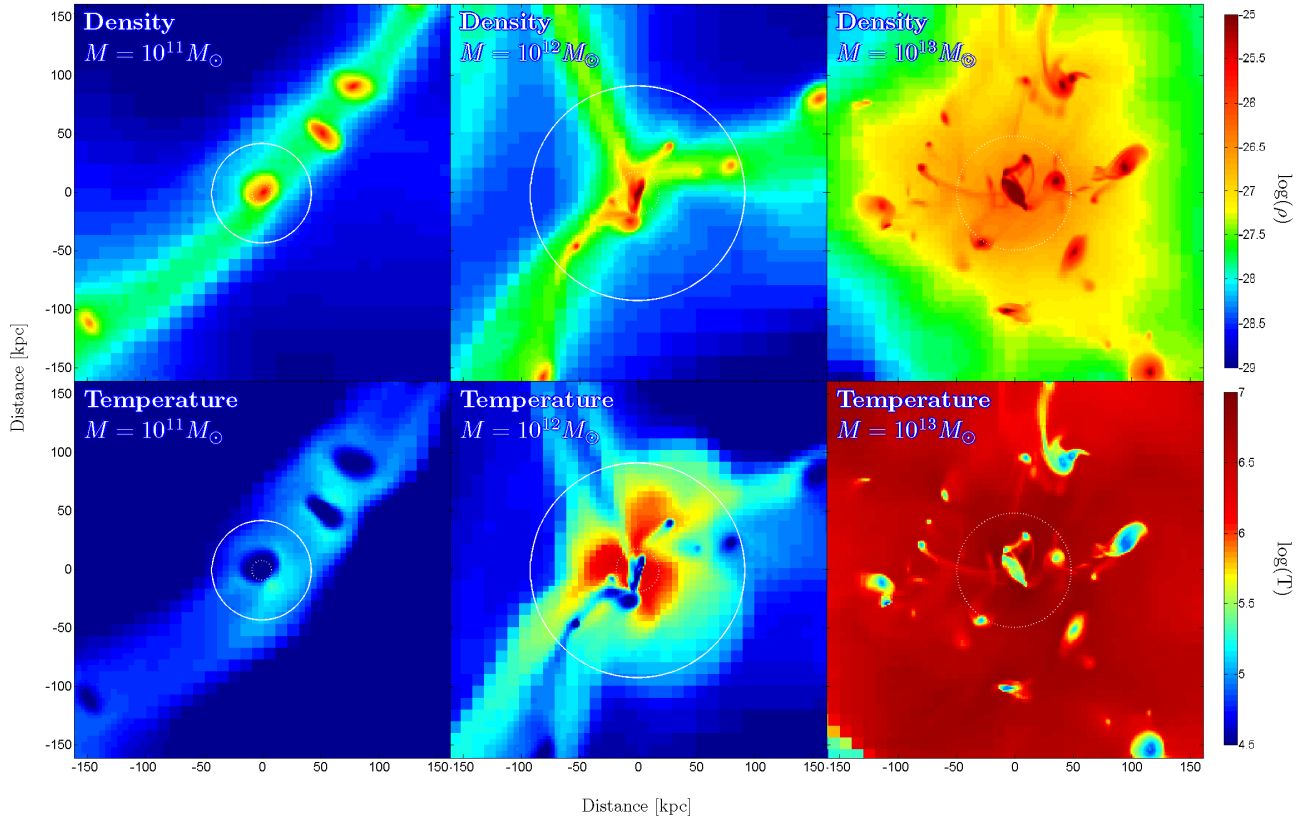


Figure 9: Maps of projected density and weighted temperature for typical haloes at redshift  $z = 2.46$  and different masses. The plain white circle indicates the virial radius  $R_{vir}$  of the halo whereas the dotted white circle indicates  $0.2 R_{vir}$ . A virial shock develops when the halo mass is higher than  $M_{vir} \approx 10^{12} M_{\odot}$ , which an intermediate regime of cold streams within a hot medium (central halo).

### 2.2.2 Slices reveal cold flows

The next step to analyze the cold streams is to select the plane where we would be able to see them as well as possible and to plot thin slices through a galaxy, defined with a linear interpolation from the initial cube. We select a typical halo of mass  $M_{vir} = 10^{12} M_{\odot}$  at  $z = 2.46$  from the simulation and we map different quantities relevant to the gas in a thin slice chosen to highlight the cold streams - we will focus on the same halo in the next sections. The Matlab programs I developed are available in the appendix section, as well as slices from three different galaxies of the same mass at the same redshift.

Fig. 10 maps different gas quantities in a thin slice centered on one typical galaxy of  $M_{vir} \approx 10^{12} M_{\odot}$  at  $z = 2.46$ : density, entropy, inward flux and radial Mach number. The shock-heated, high-entropy, low-flux medium is penetrated by three massive, narrow streams of low-entropy gas. The entropy map shows  $\log(T/\rho^{2/3})$  where the temperature and gas density are in units of the virial temperature and mean density within the virial radius. They exhibit the virial shock which covers most of the virial sphere. The narrow streams are of much lower entropy and the boundaries between them and the hot medium within the virial radius are sharp and well defined. Shocks surround the streams long before they enter the virial radius. Flux inwards is almost exclusively channeled through the narrow streams and the streaming velocities are supersonic whereas the velocity field in the hot medium is turbulent and sometimes even outflowing. The Mach number seems to be roughly the same in the dense filaments and outside the halo, but this comes from very different reasons: the density is very low outside the halo so the sound speed is high and the Mach number too, whereas in the filaments, the high values for the Mach number come from the high velocities.



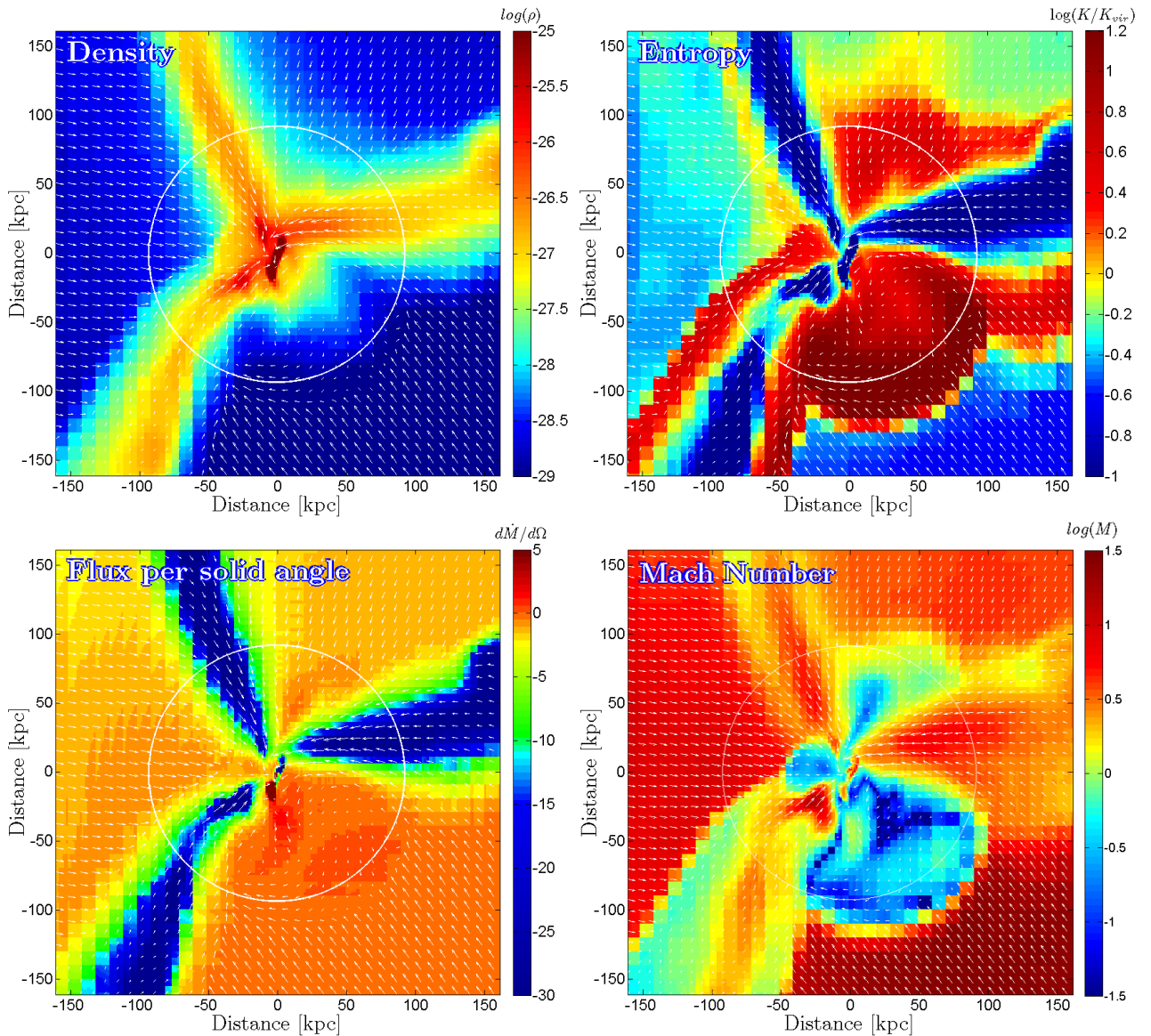


Figure 10: Gas maps in a thin slice through a galaxy of mass  $M_{vir} \approx 10^{12} M_{\odot}$  at redshift  $z = 2.46$ . Arrows describe the velocity field and the circle marks the halo virial radius. The density map emphasizes the narrowness of the streams and reveals that they are typically denser than the surrounding medium by more than an order of magnitude. The entropy  $K \propto T/\rho^{2/3}$  highlights the high-entropy medium filling the halo out to the virial shock and exhibits three radial low-entropy streams penetrating to the inner disk seen edge-on. The radial flux per solid angle,  $\dot{m} = r^2 \rho v_r$ , demonstrates that almost all the inward flux is channeled through the streams and the radial Mach number  $M = v_r/c_S$  shows that the streams are supersonic, in the contrary to the shock-heated gas.

Although the streams tend to be rather radial when viewed on scales compared to the halo virial radius, some of them flow in with impact parameters of the order of 10 kpc, comparable to the disc sizes: this steady flux is the source of angular momentum required for the buildup of a rotating disk.

### 2.2.3 Isolating the high flux regions: smooth flows versus clumpy accretion

Instead of a real three dimensional representation of the halo, isolating the high flux regions permits to have a three dimensional impression. By plotting the column density for cells whose inwards flux is higher than a certain threshold, we isolate the streams from the low flux regions. Fig. 11 displays the three dimensional structure of the streams and uncovers almost spherical clumps along two of them. The other stream can be referred as a smooth flow, as its clumps are hidden below the resolution limit and are too small to damage significantly the central disk. It is not clear to what extent the smooth component is truly smooth or built by minor clumps, and whether the smoothness has a physical origin or is merely a numerical artifact.

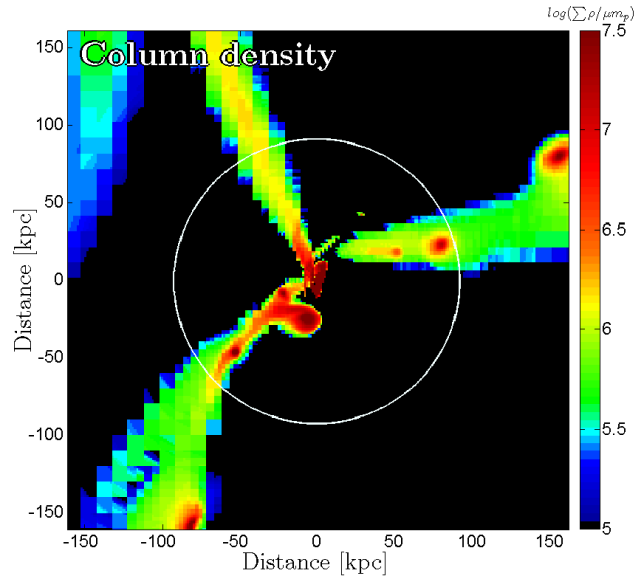


Figure 11: Flux-selected column density map for a typical halo of mass  $M_{vir} \approx 10^{12} M_{\odot}$  at  $z = 2.46$ . Are plotted only the cells in which the radial flux per solid angle  $\dot{m} = r^2 \rho v_r$  is above two times the radial flux, defined as  $\dot{m}_{vir} = R_{vir}^2 \rho_{vir} V_{vir}$ , where  $\rho_{vir} = M_{vir}/(4\pi/3 R_{vir}^3)$  and  $V_{vir} = (GM_{vir}/R_{vir})^{1/2}$ . The colors represent the logarithm of the column density divided by the molecular weight of the gas  $\mu m_p$  and the white circle corresponds to the virial radius  $R_{vir}$ . Two of the three radial streams show gas clumps of mass of the order of one tenth of the mass of the central galaxy.

## 2.3 How can we find systematically the best slice to view the streams ?

### 2.3.1 The direction of the disks

The first developed program to view the streams is a program whose input arguments are the angles defining a slice: the direction of the slice has to be defined manually. But we would like to have a program which would automatically find the best possible slice to highlight the cold streams. Motivated by the assumption that it is the cold streams which feed the angular momentum of the disk, we can assume as a first try that the direction of the disk is close to the direction of the flows. This assumption will have to be tested, but it gives at least specific directions to view the galaxy.

The direction of the disk can be determined in two different ways: by the direction of its angular momentum, and by diagonalizing its inertial tensor. But the first thing to do is to isolate the disk from the rest of the halo: we select a sphere of radius  $0.2R_{vir}$  around the center of the halo. This sphere usually encompasses the central disk but is close to its limits. The angular momentum is defined by the sum within this sphere of  $\rho_i \vec{r}_i \times \vec{v}_i$ , where  $\vec{r}_i$  is the radial vector from the center of the halo to a given cell labeled by the subscript  $i$ ,  $\rho_i$  and  $\vec{v}_i$  being the density and the velocity in that cell. The inertial tensor is defined by  $I_{\mu\nu} = \sum_i \rho_i (r_i^2 \delta_{\mu\nu} - r_{i\mu} r_{i\nu})$  where the

indexes  $\mu$  and  $\nu$  refer to the directions  $x$ ,  $y$ , and  $z$ ,  $\delta_{\mu\nu}$  is the Kronecker symbol,  $r_{i\mu}$  refers to the  $\mu$  component of the radial vector at position  $i$  and  $r_i^2$  is the distance from the center of the halo. Matlab is able to diagonalize easily the  $I_{\mu\nu}$  matrix, and the eigenvectors give the directions of the disk: the eigenvector corresponding to the smallest eigenvalue corresponds to the main direction of the disk.

Both methods converge to the same result, as shown in Fig. 12, but this method is not satisfactory enough to highlight the streams. It is nevertheless important to be able to determine the direction of the central disk, as the comparison between this direction and the direction of the streams could be interesting to understand the building of the disk.

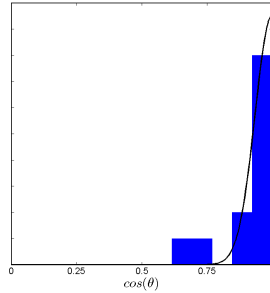


Figure 12: Cosinus of the angle between the direction given by the angular momentum and the direction obtained from the inertial tensor for the 12 downloaded haloes of mass  $M_{vir} \approx 10^{12} M_{\odot}$  at  $z = 2.46$ : both methods agree.

### 2.3.2 A numerical bias concerning the direction of the disks

The disks are expected to have a small tendency to be aligned with the  $x$ ,  $y$  and  $z$  axes of the simulation box, as can be seen in Fig. 13: the figure plots  $\cos(\theta)$  where  $\theta$  is the angle between the main direction of the disk and one of the three axes of the simulation. For each galaxy of mass  $M \approx 10^{12} M_{\odot}$ , we calculate the angle between the disk and each of the axes: if we have a gaussian distribution around the alignment case, we expect a distribution for  $\cos(\theta)$  of the form  $N = A(2\exp[\cos^2(\theta)/2\sigma^2] + \exp[(\cos(\theta) - 1)^2/2\sigma^2])$ , where  $\sigma$  is the standard deviation and  $A$  a numerical factor. The effect exists, but is small and its amplitude is comparable to the Poisson noise.

This effect comes from the discretization inherent to numerical simulations: the numerical force is not equal to the real force and induce small potential wells along the axes. Indeed, the gravitational force is computed from the matter distribution by the Poisson equation  $\nabla^2 \Phi = 4\pi G \rho$ , which implies the second order derivative of the gravitational potential  $\Phi$ . At a low order approximation and in the one dimensional case, discretization leads to equal  $\Phi''(x)$  to  $(\Phi(x + \Delta x) - 2\Phi(x) + \Phi(x - \Delta x))/\Delta x^2$  where  $\Delta x$  is the length of the grid cell: higher orders of approximation can be achieved, but this identification will always remain approximative.

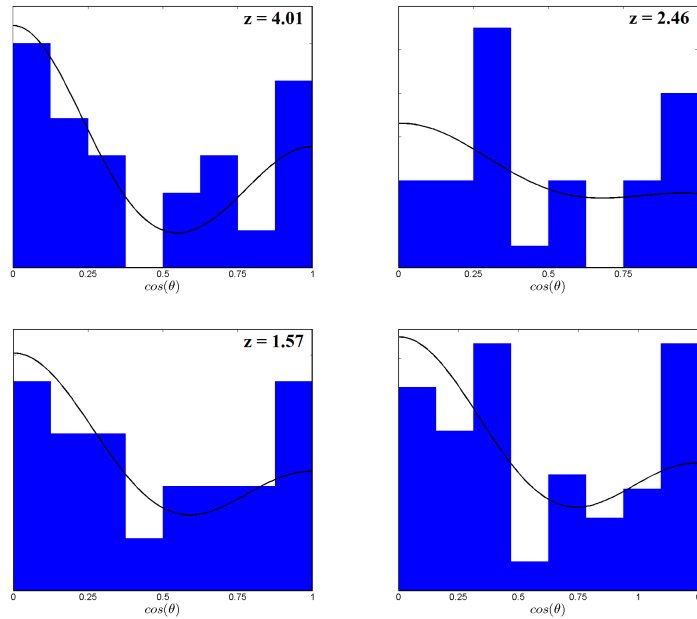


Figure 13: Cosinus of the angles between the direction of the disk and the axes of the simulation for haloes of mass  $M_{vir} \approx 10^{12} M_{\odot}$  at different redshifts. The figure to the bottom right corresponds to all redshifts together. The black curve is a fitting function of the form  $A(2 \exp[\cos^2(\theta)/2\sigma^2] + \exp[(\cos(\theta) - 1)^2/2\sigma^2])$ , whose parameters are the standard deviation  $\sigma$  and the numerical factor  $A$ .

### 2.3.3 An idea to isolate the direction of the flows

Assuming there is a slice in which the flows would be the most visible, comparing a large panel of slices would permit to select the best one. To automate this selection, we can imagine a program which would create different slices and compute a certain quantity relevant to the flows for each slice, for example the total sum on the grid cells of  $v_r/T$ ,  $S$  or even just the density  $\rho$ . The slice in which this scalar quantity would be maximal (or minimal) would be selected. A first task would have been to compare different quantities, but the realization of such a program faced a strong RAM memory problem and was not fulfilled.

### 3 Accretion around galaxies

#### 3.1 Histograms

##### 3.1.1 One dimensional histograms

Histograms permit to have an idea of the distribution of a certain quantity. Temperature and entropy histograms weighted by mass are represented in Fig. 14: we delimited the region corresponding to the cold flows by isolating the streams area in the pictures. These regions corresponds to relative peaks of the distribution, but we can't really deduce from these histograms that the accretion is bimodal. The initial purpose of these histograms was to select threshold values to isolate different regions of the accreting gas, but they did not permit to extract any robust threshold.

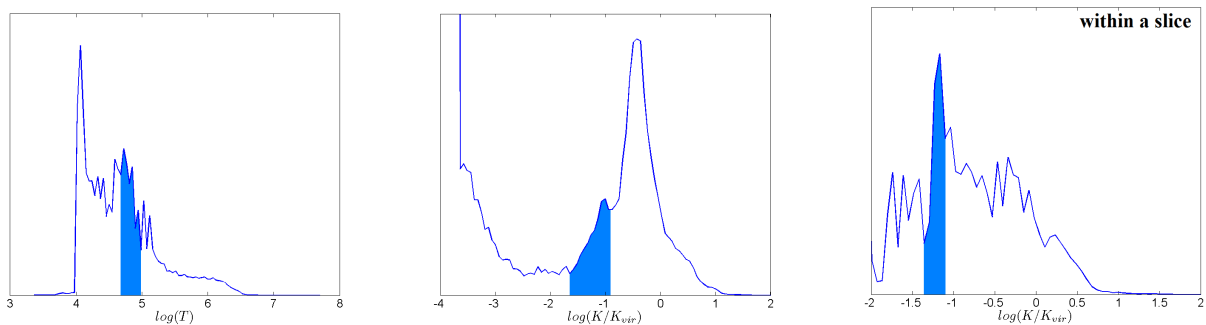


Figure 14: Mass-weighted temperature and entropy histograms for a typical halo of mass  $M_{vir} \approx 10^{12} M_{\odot}$  at  $z = 2.46$ . The filled area corresponds roughly to the cold streams and the very low values to the disk at the center of the galaxy. The figure to the right corresponds to a weighted entropy histogram within the slice of Fig. 10.

##### 3.1.2 Decomposing galaxies into components: *bird plots*

To identify and isolate the different components of the simulated systems, we use in Fig. 15 mass histograms of the gas distributed on the temperature-density plane, dubbed *bird plots*[15]. This distribution reflects the basic underlying gas processes taking place in the simulation.

The prominent line of positive slope in the lower left hand corner of the plot corresponds to the adiabatically contracting medium at the edge of the halo. This low-density gas has not yet undergone shock-heating and is not greatly affected by radiative cooling: it contracts adiabatically with  $\rho \propto T^{1/(\gamma-1)} \propto T^{2/3}$ . The diffuse area that dominates the right hand side corresponds to the shock-heated gas: its shape is the result of the complicated and different forms of cooling and shock heating taking place in the hot component of the halo gas. In the cold mode, the virial shock does not develop so the gas remains relatively cold in denser filaments, as seen in the feature rising towards the left-hand corner in the plot. Even denser regions seem to contract adiabatically in the upper line of the plot, which may be a numerical artifact. A distinction between the cold flows and the hot medium can be made from Fig. 15: the cooling processes begin to dominate the structure of the gas at  $T \sim 10^{4.5}$ .

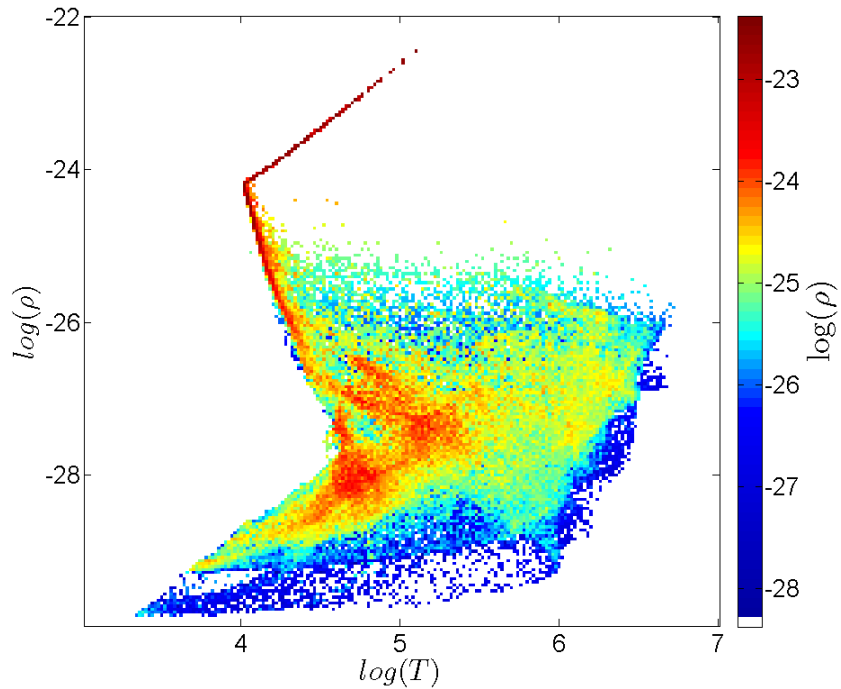


Figure 15: *Bird plot* : gas distribution on the  $T$ - $\rho$  plane for the typical halo of Fig. 10 ( $M_{vir} \approx 10^{12}M_{\odot}$ ,  $z = 2.46$ ). Color coding corresponds to the mass of the gas with given values of  $T$  and  $\rho$ . This figure reveals many of the underlying thermodynamic processes taking place in the gas. In the bottom right we see the adiabatically contracting gas from the intergalactic medium, the shock-heated gas is in the large area on the right side and we find the cold streams and gas clumps in the thin sharp rise in slope to its left.

## 3.2 Flux feeding the galaxy

### 3.2.1 Flux profiles

In order to quantify the accretion around the galaxy, we have defined the flux per solid angle  $\dot{m} = r^2 \rho v_r$ . Using a spherical grid where the angular area covered by each grid cell is constant, we can easily compute the flux as a function of the radius for each galaxy. Practically, the profiles of total mass flow rate through shells of radius  $r$  are obtained by integrating  $\rho v_r dS$  over the shell, where  $\rho$  is the gas density,  $v_r$  the radial velocity and  $dS = r^2 d\Omega$  with  $d\Omega$  the angular area element.

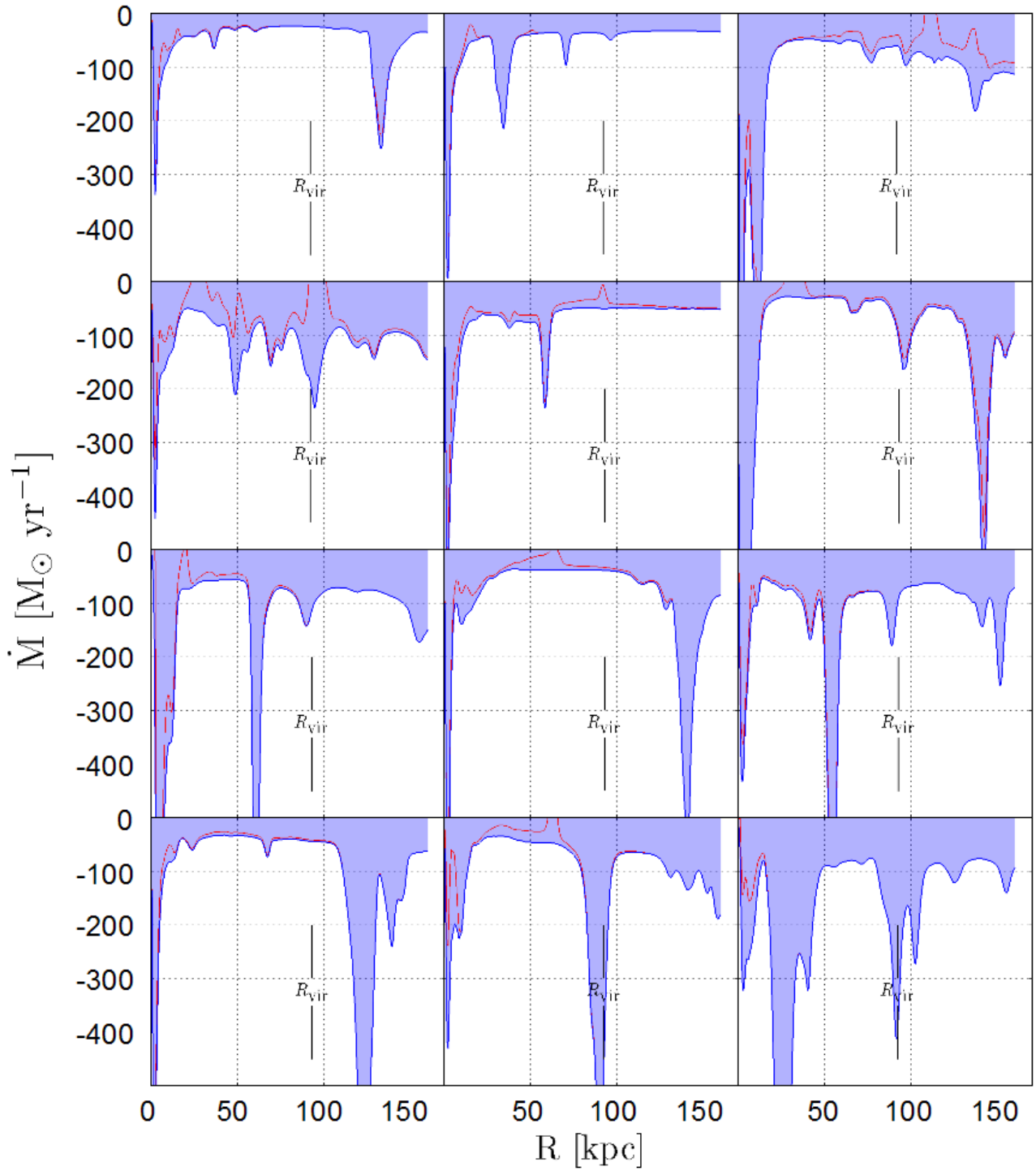


Figure 16: Profiles of total gas inflow rate through spherical shells for 12 galaxies of  $M_{\text{vir}} \approx M_{\odot}$  at  $z = 2.46$ . The blue line corresponds to the inwards flux (summation only over cells with a negative value of  $\dot{m} = r^2 \rho v_r$ ), whereas the red line corresponds to the total flux (summation over all cells).

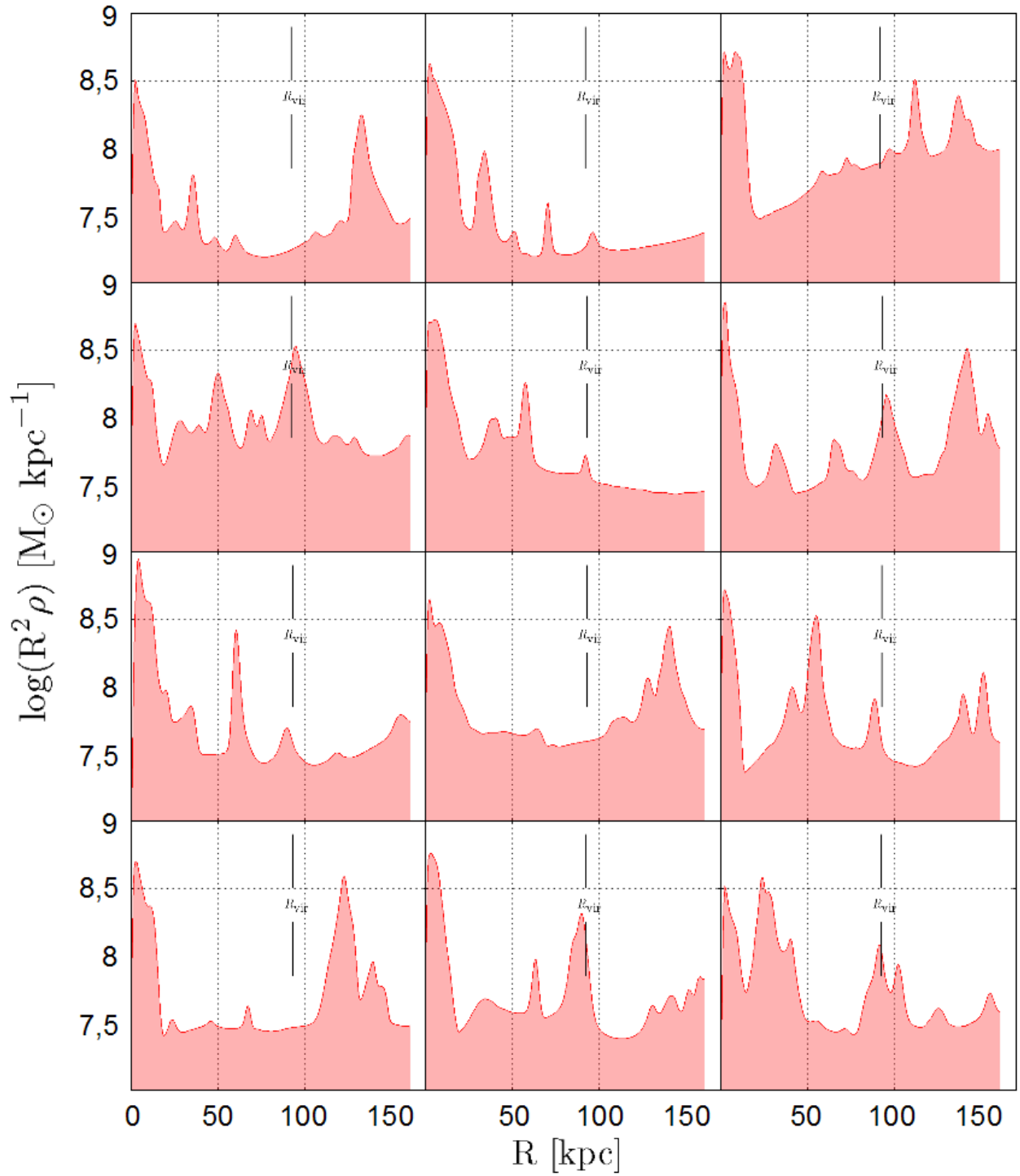


Figure 17: Density profiles on spherical shells for 12 galaxies of  $M_{vir} \approx M_{\odot}$  at  $z = 2.46$  corresponding to the galaxies of Fig. 16. These profiles permit to have an idea of the mass distribution within the halo and have to be related to the flux profiles of Fig. 16.



On average over the different galaxies of  $M_{vir} \approx M_{\odot}$  at  $z = 2.46$ , the total flux remains roughly constant from well outside the virial radius ( $R_{vir} \sim 90$  kpc) all the way to the disc vicinity inside  $r \sim 15$  kpc. This calculation takes into account the various mergers observed in the curves (minor and major ones), so the average inflow rate reaches  $\sim 100M_{\odot}\text{yr}^{-1}$ [4].

The Extended Press Schechter (EPS) theory of gravitational clustering gives an approximation for the average growth rate via mergers and smooth accretion as a function of the virial mass  $M_{vir}$  of the specified halo. This theory gives the mass distribution of the progenitors of a given halo, using a statistical approach of galaxy clustering beyond the linear growth. The growth rate of the baryonic component is expected to follow the practical formula[7]:

$$\dot{M} \approx 6.6M_{12}^{1.15}(1+z)^{2.25}f_{.165} M_{\odot}\text{yr}^{-1}$$

where  $M_{12} \equiv M_{vir}/10^{12}M_{\odot}$  and  $f_{.165}$  is the baryonic fraction in the matter in units of the cosmological value  $f_b = 0.165$ . At  $z = 2.46$ , the average baryonic growth rate of haloes of  $10^{12}M_{\odot}$  is  $\dot{M} \sim 100M_{\odot}\text{yr}^{-1}$ . Consequently, the average growth rate measured in the 12 haloes of the MareNostrum simulation is in very good agreement with the EPS prediction.

Flux profiles involving only cells along streamlines penetrating to the inner core of the halo were obtained by Tobias Goerdt: these profiles were almost the same as the profiles in Fig. 16: the galaxy is mostly fed by the cold gas streaming along the filaments to the center of the halo.

### 3.2.2 Smooth flows versus mergers

The flux profiles reveal the clumpiness of the gas streams: the clumps appear as narrow peaks of inwards flux. A large fraction of the baryons comes into the center of the halo as minor clumps or smoothed flows. These smooth flows keep the discs intact unlike destructive major mergers and assure a constant cold gas supply along the filaments of the cosmic web. This important phenomena could explain observed high star formation rates in massive galaxies in the young universe. Indeed, the surprisingly high formation rates were commonly attributed to violent mergers, which are incompatible with rotating discs. The existence of smooth cold flows could be the key to understand these star-forming galaxies, as it would supply a large enough quantity of cold gas to form stars without destroying the central disk of these galaxies[4].

## 3.3 Building the disk: the direction of the cold flows

### 3.3.1 Hammer-Aitoff maps

Cold streams are an essential phenomena to understand the building of a disk inside a halo, as the high flux filaments bring angular momentum up to the central area of the halo. One important issue is the relationship between the direction of the rotating disk and the direction of the streams: we could easily imagine that the disk develops within the plane of the gas feeding filaments - if there is such a plane.

Hammer-Aitoff projections are equal-area maps of the surface of a sphere. As for the Cosmic Microwave Background, it enables to map spherical shells around a galaxy to see the three dimensional structure of the streams. Fig. 18 shows the flux on shells around the center of a typical halo of  $M_{vir} \approx 10^{12}M_{\odot}$  at  $z = 2.46$  (still the same as in Fig. 10): we distinctly see the three streams of inward flux, preserved during their infall to the center of the galaxy.

The next step would be to plot these maps in the direction of the central disk, which would define the equatorial plane. It would enable us to visualize the direction of the streams with respect to the direction of the disk and therefore to compare visually both directions.

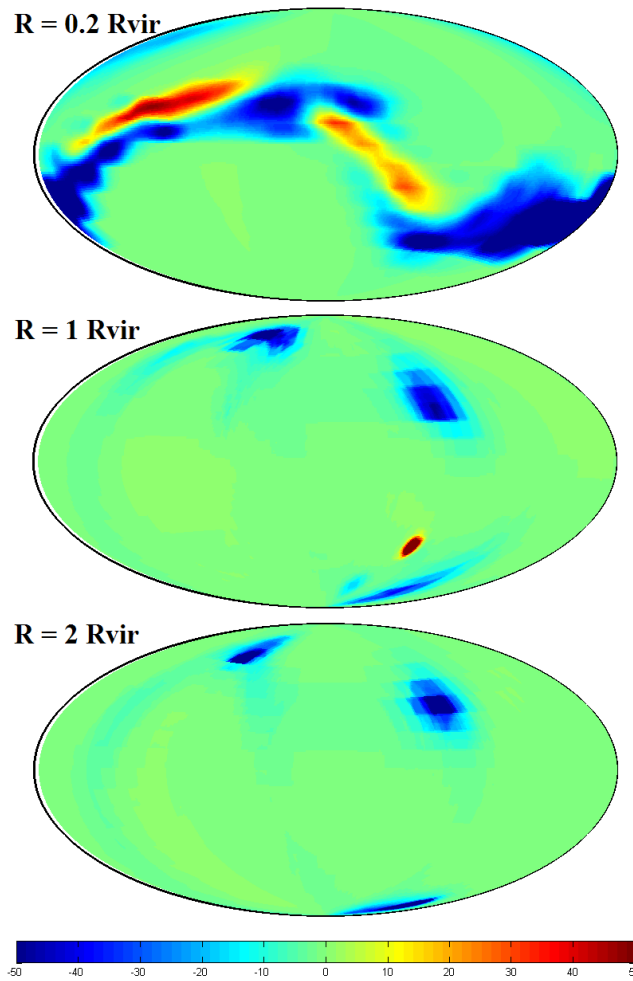


Figure 18: Hammer-Aitoff projections of the flux per solid angle for three different shells at radius  $0.2R_{vir}$ ,  $R_{vir}$  and  $2R_{vir}$  for the typical halo of Fig. 10 ( $M_{vir} \approx 10^{12}M_{\odot}$ ,  $z = 2.46$ ). The color scale represents the flux per solid angle in  $M_{\odot}\text{yr}^{-1}$ . We can clearly see the three filaments with gas flowing inwards, but as we can see it in the first map, the choice of the equatorial plane is not accurate.

### 3.3.2 Comparison between the direction of the disk and the direction of the flows

An ongoing work is to quantitatively compare the direction of the flows and the direction of the disk. The imagined means to do that is to use a certain quantity (for example the inward flux) to weight the angle between the position vector  $\vec{r}$  of each grid cell and the main direction of the disk. We would then obtain the histogram for the distribution of the cosine of this angle, which would give us an idea about the building of the disk. For the moment, difficulties concerning the Hammer-Aitoff maps have held us.

## Conclusion

During my internship, I was able to experience theoretical research in cosmology, especially the work with simulations and the research of phenomenological models to explain the data. As most of my internship was spent writing programs for Matlab, I got used to this program and more generally to programming. I wrote a few codes to work with the MareNostrum simulation which will surely be used by the rest of the team at the Hebrew University, as this simulation has still many things to teach: it is very rich and gives a statistical sample of galaxies to study their formation. The research on galaxy formation is a vast and promising subject, many questions remain unanswered and the cold flows could be very useful to solve them: How do galaxies get their angular momentum and how is the central disk formed ? How can we explain observed high star formation rates in high redshift galaxies ? What is the relationship between the Active Galactic Nuclei and the two modes of accretion ? This internship also enabled me more generally to widen my knowledge in cosmology, by the means of reading articles, attending a course on structure formation and by weekly seminars on various aspects of cosmology. And last but not least, I was able to discover a wonderful city, Jerusalem, and a very dynamic and colourful country, Israel...



Wadi in the Judean desert

## Acknowledgments

I would like to thank my supervisor, Prof. Avishai Dekel, to have given me the opportunity to discover his field of cosmology and to have welcomed me into his team, Elad Zinger to have always taken time to answer my questions and the other members of the team: Tobias Goerdts, Giora Engel and Michael Mumcuoglu for their clues in Matlab, Joanna Woo, Eyal Neistein and Noam Libeskind as well as my office mates: Ido Ben Dayan, Shlomi Ziskin, Calanit Dotan and Boaz Carni. I would also like to thank Mordechai Milgrom and Joel Primack for interesting discussions, and Gary Mamon, who prepared me for this internship.



The walls of the old city of Jerusalem viewed from the Mount of Olives

## References

- [1] Birnboim Yuval, Dekel Avishai, *Virial shocks in galactic haloes ?*, Monthly Notices of the Royal Astronomical Society 345, 349-364, 2003
- [2] Combes Françoise, Boissé Patrick, Mazure Alain, Blanchard Alain, *Galaxies et Cosmologie*, InterEditions /Éditions du CNRS, 371-395, 1991
- [3] Dekel Avishai, Birnboim Yuval, *Galaxy bimodality due to cold flows and shock heating*, Monthly Notices of the Royal Astronomical Society 368, 2-20, 2005
- [4] Dekel Avishai, Birnboim Yuval, Engel Giora, Freundlich Jonathan, Goerdt Tobias, Mumcuoglu Michael, Neistein Eyal, Pichon Christophe, Teyssier Romain, Zinger Elad, *Massive galaxy formation by cold streams*, Nature, submitted, Archiv e-prints 0808.0553, 2008
- [5] Kereš Dušan, Katz Neal, Weinberg David H., Davé Romeel, *How do galaxies get their gas ?*, Monthly Notices of the Royal Astronomical Society 363, 2-28, 2005
- [6] Milgrom Mordechai, *The MOND paradigm*, 2008, private communication
- [7] Neistein Eyal, Van den Bosch Franck C., Dekel Avishai, *Natural downsizing in hierarchical galaxy formation*, Monthly Notices of the Royal Academy of Science 372, 933-948, 2006
- [8] Ocvirk Pierre, Pichon Christophe, Teyssier Romain, *Bimodal gas accretion in the MareNostrum galaxy formation simulation*, ArXiv e-prints 0803.4506, 2008
- [9] Peacock John A., *Cosmological Physics*, Cambridge University Press, 457-494, 1999
- [10] Peebles P. J. E., *Principles of Physical Cosmology*, Princeton University Press, 528-534 & 608-622, 1993
- [11] Teyssier Romain, *Cosmological hydrodynamics with adaptive mesh refinement. A new high resolution code called RAMSES*, Astronomy and Astrophysics 385, 337-364, 2002
- [12] Riess Adam G. et al., *Observational Evidence from Supernovae for an Accelerating Universe and a Cosmological Constant*, Astronomical Journal 116, 1009-1038, 1998
- [13] White Simon D. M., *Formation and Evolution of Galaxies: Lectures given at Les Houches, August 1993*, in Cosmology and Large Scale Structure: Les Houches Session LX (ed. R. Schaeffer, J. Silk, M. Spiro and J. Zinn-Justin), North Holland, 1996
- [14] White, S. D. M., Rees, M. J., *Core condensation in heavy halos - A two-stage theory for galaxy formation and clustering*, Monthly Notices of the Royal Astronomical Society 183, 341-358, 1978
- [15] Zinger Elad, Birnboim Yuval, Dekel Avishai, Kravtsov Andrey, *Cold flows in a hot medium: angular momentum accretion in forming galaxies*, in preparation

## Appendices

## A Matlab programs

### A.1 Extracting the data from the MareNostrum simulation

After downloading the specified cubes from triguedina, a computer at the *Institut d'Astrophysique de Paris*, we have to use the files in Matlab. The following programs for Matlab were written by Elad Zinger: the first one permits to extract the data cubes from the initial .dat file specified by *filename*, the second one defines usual parameters and the last one computes the virial radius  $R_{vir}$  and the virial mass  $M_{vir}$  from the number of dark matter particles within the specified halo (the number of particles is given in the halo list of the MareNostrum simulation). As we downloaded haloes from only three different outputs, we just took into account the parameters of these three outputs (34, 75, and 128).

#### A.1.1 Reading the cubes

```
function result = read_cube(filename)
    [inp message]=fopen(filename,'rb','b');
    JUNK=fread(inp,1,'int32');
    result.nx=fread(inp,3,'int32');
    SPACE=fread(inp,2,'int32');
    result.data=reshape(fread(inp,result.nx(1)*result.nx(2)*result.nx(3),'float32'),result.nx);
    result.data=single(result.data);
    JUNK=fread(inp,1,'int32');
    fclose(inp);
end
```

#### A.1.2 Defining the environment

```
% Global MareNostrum Environment
global omega_m; global omega_l; global omega_k; global omega_b; global h; global Lbox; global Mdm;

% Cosmological parameters
omega_m=0.300000011920929E+00;
omega_l=0.699999988079071E+00;
omega_k=0.000000000000000E+00;
omega_b=0.450000017881393E-01;

% Hubble constant in units of 100 km /s /Mpc
h=0.7;

% Size of the simulation cube (comoving kpc/h)
Lbox=50000;

% Mass of a dark matter particle (solar masses)
Mdm=11695786.658674;
```

```

% Expansion factor, redshift and numerical factors depending on the output

if output==34,
    aexp=0.199702383922873E+00;
    zz=1/aexp-1;    %z=4.01

    den_fac=0.346996787056857E-27;
    len_fac=0.439345258038073E+26;
    time_fac=0.175476585435706E+17;
elseif output==75,
    aexp=0.289015390621532E+00;
    zz=1/aexp-1;    %z=2.46

    den_fac=0.114475431737723E-27;
    len_fac=0.635833878771479E+26;
    time_fac=0.367531542470913E+17;
elseif output==128,
    aexp=0.389854287769091E+00;
    zz=1/aexp-1;    %z=1.57

    den_fac= 0.466410432392356E-28;
    len_fac= 0.857679459266299E+26;
    time_fac= 0.668740009044558E+17;
else error('wrong output')
end

```

### A.1.3 Virial mass and virial radius

```

%% Find the virial mass Mvir in solar masses given the number of dark matter particles in the halo
function result=mv_MN(ndm)
    global Mdm
    Mdm= 11695786.658674;

    result= Mdm.*ndm;
end

%% Find the virial radius Rvir in kpc physical given Mvir and redshift
function result=rv(mv,z)
    % Convert mass to c.g.s
    m = mv.*1.989e+33;

    % Define cosmological parameters
    global omega_m; global omega_l; global h;
    omm0=omega_m;
    om10=omega_l;
    hub=h;

    % Average mass density of the universe in c.g.s
    avg_dens=1.877e-29*omm0*(hub^2)*(1+z)^3;

    % The virial radius is define as the radius within which the density exceeds some threshold
    omm=omm0*(1+z)^3/(om10+omm0*(1+z)^3);
    Δ=(18*(pi^2)+82*(omm-1)-39*(omm-1)^2)/omm
    result=((m.*3./Δ.*avg_dens*4*pi)).^(1/3)/(1000*3.0856e18);
end

```



## A.2 Defining the desired quantities

The quantities available directly from the simulation are: the density  $\rho$ , the pressure  $p$ , the velocities  $v_x$ ,  $v_y$  and  $v_z$ , and the metallicity  $met$ . We compute the center of mass velocity  $V_{xx}$ ,  $V_{yy}$  and  $V_{zz}$ , as well as the radial flux per solid angle  $\dot{m}$ , the radial velocity  $vr$ , the temperature  $T$ , the entropy  $S$ , the sound speed  $c$  and the radial mach number  $mach$ . We consider here cubes of resolution 14, which is the highest resolution available (about 1 kpc/h comoving).

### A.2.1 Virial quantities

```
% The virial quantities deriving from Rvir and Mvir

% Rvir in physical coordinates: kpc and cgs
Rvir_kpc=Rvir/h*aexp;
Rvirial=Rvir_kpc*3.08568025*10^21;

% Mvir in cgs
Mvirial=Mvir*1.9891*10^33;

% The following quantities are in cgs units
f_b=0.165;
Rhovirial=f_b*Mvirial/(4*pi/3*Rvirial^3);

Gcgs=6.6725985*10^(-8);
Vvirial=sqrt(Gcgs*Mvirial/Rvirial);

m=0.59*1.672623110*10^(-24);
kb=1.38065812*10^(-16);
Tvirial=1/2*Vvirial^2*m/kb;

% Virial flux in solar masses/year
Mdotvirial=0.165*40*(Mvir/10^12)^1.15*(1+zz)^2.25;
```

### A.2.2 Physical quantities

```
% Center of mass velocity
M=sum(sum(sum(rho)));
Vx_cm=sum(sum(sum(vx.*rho)))/M;
Vy_cm=sum(sum(sum(vy.*rho)))/M;
Vz_cm=sum(sum(sum(vz.*rho)))/M;

Vxx=vx-Vx_cm;
Vyy=vy-Vy_cm;
Vzz=vz-Vz_cm;
clear vx vy vz Vx_cm Vy_cm Vz_cm M

% Radial flux per solid angle (solar masses/year)
[y, x, z] = meshgrid(1:n(1), 1:n(2), 1:n(3));
x=single(x - ic);
y=single(y - jc);
z=single(z - kc);

resolution=14;
x=x*50000/(2^resolution);
y=y*50000/(2^resolution);
z=z*50000/(2^resolution);

x=x/h*aexp;
y=y/h*aexp;
z=z/h*aexp;
```

```

global mdot
mdot=sqrt(x.^2+y.^2+z.^2);
mdot=mdot.*(Vxx.*x+Vyy.*y+Vzz.*z);
mdot=mdot.*rho;
mdot=mdot*(3.08568025*10^21)^2/(1.98892E33)*31536000;

% Radial velocity (cgs)
global vr
vr=x.*Vxx+y.*Vyy+z.*Vzz;
vr=vr./sqrt(x.^2+y.^2+z.^2);
clear x y z

% Temperature
global T
m=0.59*1.67262158E-24;
T=m/(1.380658E-16)*p./rho;

% Entropy
global S
S=(T.*(rho.^(-2/3)));
S=S/(Tvirial*Rhovirial^(-2/3));
S=log10(S);

% Sound speed
gamma=5/3;
c=sqrt(gamma*p./rho);

% Mach number
global mach
mach=vr./c;\emph{}

```

### A.2.3 Finding the center of the cube

```

function result=find_center(rho,resolution)
global Xc Yc Zc
n=size(rho);

if resolution==13,
    smooth_length=5;
elseif resolution==14,
    smooth_length=9;
end

sbox=[smooth_length,smooth_length,smooth_length];
rho_s=smooth3(rho,'gaussian',sbox);
[C,ind]=max(rho_s(:));
[i,j,k]=ind2sub(n,ind);
ijk=[i, j, k]

Xc=i-(n(1)+1)/2;
Yc=j-(n(2)+1)/2;
Zc=k-(n(3)+1)/2;
Xc=Xc*50000/(2^resolution);
Yc=Yc*50000/(2^resolution);
Zc=Zc*50000/(2^resolution);
DX=Xc/50000;
DY=Yc/50000;
DZ=Zc/50000;

result=[DX DY DZ];
end

% If the initial center was "center" (in cube units - between 0 and 1)
DL=find_center(rho,resolution);
new_center=center+DL;

```

## A.2.4 Projected density

```

% Simple projected density along the three directions
function rhoview(rho, cubename, output, resolution)
    filename='%s_%s.png';
    cname='%d_o%d_l%d';
    cname=sprintf(cname, cubename, output, resolution);

    figure('Position',[5 -135 1000 1000])
    imagesc(log10(squeeze(mean(rho,1))))
    colorbar
    cdens1=get(gcf,'Colormap');
    xlabel('Z','FontSize',12,'Interpreter','latex');
    ylabel('Y','FontSize',12,'Interpreter','latex');
    title('Density (log) direction X','FontSize',14,'Interpreter','latex');
    saveas(gcf,sprintf(filename,cname,'rho1'))

    figure('Position',[5 -135 1000 1000])
    imagesc(log10(squeeze(mean(rho,2))))
    colorbar
    set(gcf,'Colormap',cdens1)
    xlabel('Z','FontSize',12,'Interpreter','latex');
    ylabel('X','FontSize',12,'Interpreter','latex');
    title('Density (log) direction Y','FontSize',14,'Interpreter','latex');
    saveas(gcf,sprintf(filename,cname,'rho2'))

    figure('Position',[5 -135 1000 1000])
    imagesc(log10(squeeze(mean(rho,3))))
    colorbar
    set(gcf,'Colormap',cdens1)
    xlabel('Y','FontSize',12,'Interpreter','latex');
    ylabel('X','FontSize',12,'Interpreter','latex');
    title('Density (log) direction Z','FontSize',14,'Interpreter','latex');
    saveas(gcf,sprintf(filename,cname,'rho3'))
end

% Projected density with a flux threshold (depending on the virial flux Mdotvirial)
function just_flow(mat,direction,frac)
    global rho T S vr mdot aexp Mdotvirial
    mdotc=-frac*Mdotvirial/(4*pi);
    tic=[9.4531 49.1354 88.8177 128.5 168.1813 207.8646 247.5469];
    dim={'-150','-100','-50','0','50','100','150'};
    index=single(find(mdot<mdotc));
    mat1=single(zeros(size(mat)));
    mat1(index)=mat(index);
    weight=mat1≠0;
    norm2=0.6*1.6726231*20^(-24); %mu*mproton CGS

    figure('Position',[5 -135 1000 1000])
    imagesc(log10(squeeze(sum(mat1,direction))/norm2)),
    load('flowmap2')
    set(gcf,'Colormap',flowmap2)
    caxis([4.5 8.5])
    text(7,243,'Column density','Interpreter','latex','FontSize',22,'Color',[1 1 1],'FontWeight','bold')
    c=colorbar;
    set(c,'YTick',[3 4 5 6 7 8 9],'FontSize',14);
    set(get(c,'Title'),'string','log(∑  $\frac{\rho}{\mu m_p}$ )','Interpreter','latex','FontSize',14);
    set(gca,'Xdir','normal');
    set(gca,'Ydir','normal');
    set(gca,'XTick',tic)
    set(gca,'YTick',tic)
    set(gca,'XTickLabel',dim,'FontSize',14)
    set(gca,'YTickLabel',dim,'FontSize',14)
    xlabel('Distance [kpc]','Interpreter','latex','FontSize',18)
    ylabel('Distance [kpc]','Interpreter','latex','FontSize',18)
end

```

## A.3 Viewing a slice

### A.3.1 Defining the slice

The slice is defined by the position of the center, *niveau*, and by the two angles *theta* and *phi*. For each slice, one of the initial direction x, y or z is chosen to fit the slice. Here we present a slice viewed along the y axis, for  $256 \times 256 \times 256$  cubes.

```
% Extrema of the slice (at the edges of the cube)
YA=niveau+255/2*(-tan(theta)-tan(phi));
YB=niveau+255/2*(-tan(theta)+tan(phi));
YC=niveau+255/2*(tan(theta)-tan(phi));
YD=niveau+255/2*(tan(theta)+tan(phi));

[Z,X]=meshgrid(1:255:256);
Y=[YC YD;YA YB];

[Zi,Xi]=meshgrid(1:256);
Yi=interp2(Z,X,Y,Zi,Xi);

Ymin=round(Yi-width/2);
Ymax=Ymin+width-1;

% Quantities within the slice
rho_slice=zeros(256,width,256);
T_slice=zeros(256,width,256);
S_slice=zeros(256,width,256);
vx_slice=zeros(256,width,256);
vy_slice=zeros(256,width,256);
vz_slice=zeros(256,width,256);
mdot_slice=zeros(256,width,256);
mach_slice=zeros(256,width,256);

for i=1:256,
    for j=1:256,
        ymin=Ymin(j,i);
        ymax=Ymax(j,i);
        rho_slice(i,:,j)=rho(i,ymin:ymax,j);
        S_slice(i,:,j)=S(i,ymin:ymax,j);
        vx_slice(i,:,j)=Vxx(i,ymin:ymax,j);
        vy_slice(i,:,j)=Vyy(i,ymin:ymax,j);
        vz_slice(i,:,j)=Vzz(i,ymin:ymax,j);
        mdot_slice(i,:,j)=mdot(i,ymin:ymax,j);
        mach_slice(i,:,j)=abs(mach(i,ymin:ymax,j));
    end
end

rho_mean=squeeze(mean(rho_slice,2));
R=sum(rho_slice,2);
S_mean=squeeze(mean(S_slice,2));
vxrho=sum(vx_slice.*rho_slice,2);
vyrho=sum(vy_slice.*rho_slice,2);
vzrho=sum(vz_slice.*rho_slice,2);
vx_mean=squeeze(vxrho./R);
vy_mean=squeeze(vyrho./R);
vz_mean=squeeze(vzrho./R);
mdot_mean=squeeze(mean(mdot_slice,2));
```

**A.3.2 How do the slice look like ?**

```

% The picture of the slice permits to detect possible errors
figure(niveau*10)
mesh(Xi,Yi,Zi,C)
hold on
mesh(Xi,Yi+width-1,Zi,C)

%Tracing the cube
vertex_matrix=[1 1 1;256 1 1;256 256 1;1 256 1;1 1 256;256 1 256;256 256 256;1 256 256];
faces_matrix=[1 2 6 5;2 3 7 6; 3 4 8 7; 4 1 5 8;1 2 3 4; 5 6 7 8];
patch('Vertices',vertex_matrix,'Faces',faces_matrix,'FaceVertexCData',hsv(6),'Facecolor','white')
alpha(0.5)

%To view the points A,B,C,D
text(256,YA,1,'A')
text(256,YB,256,'B')
text(1,YC,1,'C')
text(1,YD,256,'D')

set(gca,'Xdir','normal')
set(gca,'Ydir','normal')
set(gca,'Zdir','normal')
set(gca,'Xlim',[1 256])
set(gca,'Ylim',[1 256])
set(gca,'Zlim',[1 256])
set(gca,'YTick',round(YA))
set(gca,'YTickLabel',round(YA))
set(gca,'YTick',round(YB))
set(gca,'YTickLabel',round(YB))
set(gca,'YTick',round(YC))
set(gca,'YTickLabel',round(YC))
set(gca,'YTick',round(YD))
set(gca,'YTickLabel',round(YD))
xlabel('X')
ylabel('Y')
zlabel('Z')
view(20,26)
hold off

```

**A.3.3 An image of the slice: density**

```

figure('Position',[5 -135 1000 1000])
imagesc(log10(rho_mean))
colormap(jet)
load('densmap')
set(gcf,'Colormap',densmap)
caxis([-29 -25])
c=colorbar;
axis square

set(gca,'Xdir','normal');
set(gca,'Ydir','normal');
set(gca,'XTick',tic)
set(gca,'YTick',tic)
set(gca,'XTickLabel',dim,'FontSize',18)
set(gca,'YTickLabel',dim,'FontSize',18)

set(get(c,'Title'),'string','log( $\rho$ )','Interpreter','latex','FontSize',26);
set(c,'YTick',[-29 -28.5 -28 -27.5 -27 -26.5 -26 -25.5 -25],'FontSize',14);
xlabel('Distance [kpc]','Interpreter','latex','FontSize',24)
ylabel('Distance [kpc]','Interpreter','latex','FontSize',24)

% To trace the Virial Radius

```

```

t=linspace(0,2*pi,1000);
h=256/2;
k=256/2;
xvir=Rvir*cos(t)+h;
yvir=Rvir*sin(t)+k;

hold on
plot(xvir,yvir,'w','LineWidth',2)

% Add velocity arrows
hold on
[x z]=meshgrid(1:pas:256,1:pas:256);
vx_mean=vx_mean(1:pas:256,1:pas:256);
vy_mean=vy_mean(1:pas:256,1:pas:256);
vz_mean=vz_mean(1:pas:256,1:pas:256);
quiver(z,x,transpose(vz_mean),transpose(vx_mean),'w','LineWidth',1.2)

text(6,243,'Density','Interpreter','latex','FontSize',32,'Color',[0 0 1],'FontWeight','bold')
text(8,243,'Density','Interpreter','latex','FontSize',32,'Color',[0 0 1],'FontWeight','bold')
text(7,242,'Density','Interpreter','latex','FontSize',32,'Color',[0 0 1],'FontWeight','bold')
text(6,244,'Density','Interpreter','latex','FontSize',32,'Color',[0 0 1],'FontWeight','bold')
text(7,243,'Density','Interpreter','latex','FontSize',32,'Color',[1 1 1],'FontWeight','bold')

```

## A.4 The direction of the disk

### A.4.1 Inertial tensor

```

% We compute the inertial tensor inside 0.2 Rvir (R is in grid cells)
f=0.2;
R=f*Rvir/50000*2^14;
radius=ceil(R)+1;
radius1=[ic jc kc]-radius;
radius2=[ic jc kc]+radius;

rho=rho(radius1(1):radius2(1),radius1(2):radius2(2),radius1(3):radius2(3));
vx=vx(radius1(1):radius2(1),radius1(2):radius2(2),radius1(3):radius2(3));
vy=vy(radius1(1):radius2(1),radius1(2):radius2(2),radius1(3):radius2(3));
vz=vz(radius1(1):radius2(1),radius1(2):radius2(2),radius1(3):radius2(3));
clear radius1 radius2

n_inertia=size(rho);
ntot_inertia=n_inertia(1)*n_inertia(2)*n_inertia(3);

index=1:ntot_inertia;
[i,j,k]=ind2sub(n_inertia,index);
clear index

i=i';
j=j';
k=k';

X=i-(radius+1);
Y=j-(radius+1);
Z=k-(radius+1);

Ixx=sum(rho(:).*(X.^2));
Ixy=sum(rho(:).*X.*Y);
Ixz=sum(rho(:).*X.*Z);
Iyy=sum(rho(:).*(Y.^2));
Iyz=sum(rho(:).*Y.*Z);
Izz=sum(rho(:).*(Z.^2));
clear rhocore

I=[Ixx,Ixy,Ixz;Ixy,Iyy,Iyz;Ixz,Iyz,Izz];

```

```
clear Ixx Ixy Ixz Iyy Iyz Izz

% We search the eigenvectors and eigenvalues of the inertial tensor I
[V,D]=eig(I,'nobalance');
clear I

Eigval=[D(1,1),D(2,2),D(3,3)];
[Cmax,I1]=max(Eigval);
[Cmin,I3]=min(Eigval);
I2=6-I1-I3;
clear Cmax Cmin Eigval D

V1=V(:,I1)/norm(V(:,I1));
V2=V(:,I2)/norm(V(:,I2));
V3=V(:,I3)/norm(V(:,I3));
clear V I1 I2 I3
% V3 corresponds to the main direction of the disk
```

#### A.4.2 Angular momentum

```
% We compute the angular momentum J
X=reshape(X,n_inertia);
Y=reshape(Y,n_inertia);
Z=reshape(Z,n_inertia);

Jx=rho.*(Y.*vz-Z.*vy);
Jy=rho.*(Z.*vx-X.*vz);
Jz=rho.*(X.*vy-Y.*vx);
Jx=sum(Jx(:));
Jy=sum(Jy(:));
Jz=sum(Jz(:));
J=[Jx,Jy,Jz];
J=J/norm(J);
```

#### A.4.3 Comparing the two methods

```
% Both vectors are normalized
cosangle=dot(V3,J);

% We then apply the following function to plot the histogram
function result=histo(mat,edges,n)
    absc=linspace(edges(1),edges(2),n+1);
    offset=(absc(2)-absc(1))/2;
    absc=absc+offset;
    absc=absc(1:n);

    n=hist(mat,absc);
    hist(mat,absc)
    set(gca,'Xlim',[edges(1) edges(2)])

    result=[absc,'n'];
end
```

#### A.4.4 Study of a numerical bias: the alignment with the grid

```
% Defining the cosinus of the angles
ux=[1;0;0];
uy=[0;1;0];
uz=[0;0;1];

cosx=dot(V3,ux);
cosy=dot(V3,uy);
cosz=(dot(V3,uz));
```

```
% We plot a histogram for the different values, all directions and all haloes together
% data is the matrix containing the absolute values of the cosinus
[absc,n]=histo(data,[0 1],8);

% Fitting function
function result=bigaussian_fit(params,x,y)
    A=params(1);
    sigma=params(2);

    Fitted_curve=A.*(2*exp(-x.^2/sigma^2)+exp(-(x-1).^2/sigma^2));
    Error_vector=Fitted_curve-y;

    result=sum(Error_vector.^2);
end

% Fitted parameters
Starting=rand(1,2);
options=optimset('Display','iter');
Estimates=fminsearch(@bigaussian_fit,Starting,options,absc,n)
% Estimates gives the values of the two parameters A and sigma
```

#### A.5 Bird plots

```
% hist2d is a program adapted from a program written by Elad Zinger.
% xx: we can make bird plots defined by mass or number of particles...

function result = hist2d(T,rho,xx,weight)
    global tro mnro mxro mnt mxt

    ltm=(T);
    lro=(rho);
    wt=ones(size(ltm));
    wt=wt.*weight;

    ltm=ltm(:);
    lro=lro(:);
    wt=wt(:);
    xx=xx(:);

    len=200;
    mnro=floor(min(lro));
    mxro=ceil(max(lro))-mnro;
    mnt=floor(min(ltm));
    mxt=ceil(max(ltm))-mnt;

    tro=zeros(len,len,2);

    ltm=ltm-mnt;
    lro=lro-mnro;

    for i=1:size(ltm,1)
```



```

indx=round((ltm(i)./mxt).*len);
indy=round((lro(i)./mxro).*len);
if indx==0, indx=1;end
if indy==0, indy=1; end
tro(indx,indy,1)=tro(indx,indy,1)+xx(i).*wt(i);
tro(indx,indy,2)=tro(indx,indy,2)+wt(i);
end

%Bird Plot
figure
imagesc(transpose(log10(tro(:, :, 1))))
colorbar
load('bird_colormap')
set(gcf, 'Colormap', bird_colormap)
set(gca, 'Xdir', 'normal')
set(gca, 'Ydir', 'normal')
xlabel('log T')
ylabel('log \rho')
title('Mass Bird')
set(gca, 'XTick', [(2-mnt)*len/mxt, (3-mnt)*len/mxt, (4-mnt)*len/mxt, (5-mnt)*len/mxt, ...
(6-mnt)*len/mxt, (7-mnt)*len/mxt, (8-mnt)*len/mxt, (9-mnt)*len/mxt, (10-mnt)*len/mxt, ...
(11-mnt)*len/mxt, (12-mnt)*len/mxt, (13-mnt)*len/mxt, (14-mnt)*len/mxt])
set(gca, 'YTick', [(-30-mnro)*len/mxro, (-28-mnro)*len/mxro, (-26-mnro)*len/mxro, ...
(-24-mnro)*len/mxro, (-22-mnro)*len/mxro, (-20-mnro)*len/mxro, (-18-mnro)*len/mxro])
set(gca, 'XTickLabel', [2, 3, 4, 5, 6, 7, 8, 9, 10, 11, 12, 13, 14])
set(gca, 'YTickLabel', [-30, -28, -26, -24, -22, -20, -18])
end

```

## A.6 Spherical coordinates

### A.6.1 Unity sphere

```

% The following function defines and plot the unity sphere (equal angular area sphere)
function [xx,yy,zz]=uni_sphere(n)
    error(nargchk(0,2,nargin));
    [cax,args,nargs] = axescheck(n);

    n=n-1;
    theta = (-n:2:n)/n*pi;
    phi = acos((-n:2:n)/n)-pi/2;

    cosphi = cos(phi); cosphi(1) = 0; cosphi(n+1) = 0;
    sintheta = sin(theta); sintheta(1) = 0; sintheta(n+1) = 0;

    x = cosphi*cos(theta);
    y = cosphi*sintheta;
    z = sin(phi)*ones(1,n+1);

    if nargout==0,
        cax = newplot(cax);
        surf(x,y,z)
    else
        xx = x; yy = y; zz = z;
    end
end

```

## A.6.2 Transferring to spherical coordinates

```

% We transfer a cube in cartesian coordinates into a cube in spherical coordinates
% cube: the cartesian cube wanted in spherical coordinates
% MAX_R: maximum value of r (number of cells)
% center: center of the cube
function result=create_sphere(cube,MAX_R,center)
result = zeros(size(cube),'single');
CUBE_SIZE = size(cube,1);
SPHERE_RES = CUBE_SIZE;
INTERP = 'linear';

[Sx Sy Sz] = uni_sphere(SPHERE_RES);
size(Sx);
RR = [0.5:0.5:((CUBE_SIZE-1)/2)];
% length(RR) = CUBE_SIZE -1

if ~exist('MAX_R','var')
MAX_R = length(RR);
end

if ~exist('center','var')
center = (CUBE_SIZE+1)/2;
center=[center,center,center];
end

MAX_R=min([MAX_R (CUBE_SIZE-1)]);

for ridx = 1:MAX_R
RSx = RR(ridx)*Sx+center(1);
RSy = RR(ridx)*Sy+center(2);
RSz = RR(ridx)*Sz+center(3);

result(ridx,,:) =single(interp3(cube, RSx, RSy, RSz, INTERP));
end
end

```

## A.7 Flux profiles

### A.7.1 Flux as a function of the radius

```

% Spherical coordinates

% (ic,jc,kc) is the center of the cube
max_r=2*min([floor(nc/2),ic,nc-ic,jc,nc-jc,kc,nc-kc]);

rho=create_sphere(rho,max_r,[ic jc kc]);
vr=create_sphere(vr,max_r,[ic jc kc]);

% n=[256,256,256] is the size of the initial cubes
[y, x,, z] = meshgrid(1:n(1), 1:n(2), 1:n(3));
r=x*50000/(2^resolution)/h*aexp/2;

mdot=vr.*r.^2.*rho*(3.08568025E21)^2;
mdot=mdot/(1.98892E33)*31536000; %In solar masses/year

% As a function of the radius
r = 0.5:0.5:((max_r-1)/2);
r=r*50000/2^resolution/h*aexp;

flux_tot=squeeze(sum(sum(mdot,2),3)*4*pi/(nc^2));
flux_tot=flux_tot(1:(max_r-1))';

```

```

in=mdot<0;
flux_in=squeeze(sum(sum(mdot.*in,2),3)*4*pi/(nc^2));
flux_in=flux_in(1:(max_r-1));

vvir=vr≤(-Vvirial)/2;
flux_vvir=squeeze(sum(sum(mdot.*vvir,2),3)*4*pi/(nc^2));
flux_vvir=flux_vvir(1:(max_r-1));

% Eventually: temperature and entropy thresholds Tc and Sc
cold=log10(T)<Ts;
flux_cold=squeeze(sum(sum(mdot.*cold,2),3)*4*pi/(nc^2));
flux_cold=flux_cold(1:(max_r-1));

lows=S<Ss;
flux_lows=squeeze(sum(sum(mdot.*lows,2),3)*4*pi/(nc^2));
flux_lows=flux_lows(1:(max_r-1));

```

### A.7.2 Flux profiles: plots

```

figure('Position',[5 -135 1000 1000])
plot(r,flux_tot,'r','LineWidth',1.5)
hold on
plot(r,flux_in,'b','LineWidth',2)
hold on
jbbfill(r,ze,flux_in,'b','w',1,0.3)
hold on
plot([0 170],[0 0],'k','LineWidth',1.5)
hold on
axis([0 170 -300 0])
grid on
set(gca,'FontSize',20)
plot([0 170],[0 0],'k','LineWidth',3)
plot([0 170],[-300 -300],'k','LineWidth',3)
plot([0 0],[-300 0],'k','LineWidth',3)
plot([170 170],[-300 0],'k','LineWidth',3)
plot([Rvir_kpc Rvir_kpc],[-225 -175],'k','LineWidth',2)
plot([Rvir_kpc Rvir_kpc],[-150 -100],'k','LineWidth',2)
text(Rvir_kpc-5,-160,'Rvir','FontSize',24,'Interpreter','latex','Color','k','FontWeight','bold')

xlabel('R [kpc]','FontSize',22,'Interpreter','latex','FontWeight','bold');
ylabel('Ḁ [M⊙-yr-1'],'FontSize',22,'Interpreter','latex','FontWeight','bold');
legend('Ḁtot','Ḁ<0');
set(legend(),'interpreter','latex','Location','SouthWest','FontSize',24,'FontWeight','bold')

function [fillhandle,msg]=jbbfill(xpoints,upper,lower,color,edge,add,transparency)
    %USAGE: [fillhandle,msg]=jbbfill(xpoints,upper,lower,color,edge,add,transparency)
    %This function will fill a region with a color between the two vectors
    %fillhandle is the returned handle to the filled region in the plot.
    %xpoints= The horizontal data points (ie frequencies).
    %upper = the upper curve values (data can be less than lower)
    %lower = the lower curve values (data can be more than upper)
    %color = the color of the filled area
    %edge = the color around the edge of the filled area
    %add = a flag to add to the current plot or make a new one.
    %transparency is a value ranging from 1 for opaque to 0 for invisible, for the filled color only.
    %John A. Bockstege November 2006;

    if nargin<7;transparency=.5;end %default is to have a transparency of .5
    if nargin<6;add=1;end %default is to add to current plot
    if nargin<5;edge='k';end %default edge color is black
    if nargin<4;color='b';end %default color is blue

    if length(upper)==length(lower) && length(lower)==length(xpoints)
        msg='';
        filled=[upper,flipplr(lower)];
        xpoints=[xpoints,flipplr(xpoints)];
    end

```

```
    if add
        hold on
    end
    fillhandle=fill(xpoints, filled, color);
    set(fillhandle, 'EdgeColor', edge, 'FaceAlpha', transparency, 'EdgeAlpha', transparency);
    if add
        hold off
    end
    else
        msg='Error: Must use the same number of points in each vector';
    end
end
```

### A.7.3 Density profiles

```
% We plot the density as a function of the radius r
r = 0.5:0.5:((256-1)/2);
r=r(1:(256-1));
r=r*50000/2^resolution/h*aexp;

rhor=squeeze(mean(mean(rho,3),2));

ze=7*ones(size(rho));

msun=1.98892*10^33;
kpc=3.08568025*10^21;

figure('Position',[5 -135 1000 1000])
quant=log10(r.^2.*rho/msun*kpc^3);
plot(r,quant,'r','LineWidth',1.5)

hold on
jbbfill(r',quant,ze','r','w',1,0.3)
hold on
axis([0 170 7 9])
grid on
plot([0 170],[7 7],'k','LineWidth',3)
plot([0 170],[9 9],'k','LineWidth',3)
plot([0 0],[7 9],'k','LineWidth',3)
plot([170 170],[7 9],'k','LineWidth',3)

set(gca,'YTick',[7 7.5 8 8.5 9])
set(gca,'YTickLabel',[7 7.5 8 8.5 9],'FontSize',30)
plot([Rvir_kpc Rvir_kpc],[7.85 8.25],'k','LineWidth',2)
plot([Rvir_kpc Rvir_kpc],[8.5 8.90],'k','LineWidth',2)
text(Rvir_kpc-5,8.375,'Rvir','FontSize',24,'Interpreter','latex','Color','k','FontWeight','bold')
```

## A.8 Hammer-Aitoff maps

### A.8.1 Rotating the spherical grid

```

% Rotated unity sphere
function [xx,yy,zz]=uni_sphere2(n,thetac,phic)
    [cax,args,nargs] = axescheck(n);
    n=n-1;
    phi = (-n:2:n)/n*pi;
    theta = (-n:2:n)'/n*pi/2+pi/2;

    x = sin(theta)*cos(phi);
    y = sin(theta)*sin(phi);
    z = cos(theta)*ones(1,n+1);
    x=cos(thetac).*x-sin(thetac).*y;
    y=cos(thetac)*sin(phic).*x+cos(thetac)*cos(phic)*y+sin(thetac)*z;
    z=-sin(thetac)*sin(phic).*x-sin(thetac)*cos(phic)*y+cos(thetac)*z;

    if nargsout == 0
        cax = newplot(cax);
        surf(x,y,z)
    else
        xx = x; yy = y; zz = z;
    end
end

% Rotated surface of the sphere at a specified radius
function result=aitoff_sphere(cube,thetac,phic,radius,center)
    CUBE_SIZE = size(cube,1);
    SPHERE_RES = CUBE_SIZE;
    INTERP = 'linear';
    [Sx Sy Sz] = uni_sphere2(SPHERE_RES,thetac,phic);
    size(Sx);

    if ~exist('center','var')
        center = (CUBE_SIZE+1)/2;
        center=[center,center,center];
    end

    RSx = radius*Sx+center(1);
    RSy = radius*Sy+center(2);
    RSz = radius*Sz+center(3);
    result=single(interp3(cube, RSx, RSy, RSz, INTERP));
end

```

### A.8.2 Hammer-Aitoff projection

```

function aitoff(data)
    n=size(data);

    [theta,phi]=meshgrid(1:n(2),1:n(1));
    [thetaI,phiI]=meshgrid(1:360,1:180);
    thetaI=thetaI*n(1)/360;
    phiI=phiI*n(2)/180;

    dataitoff=double(interp2(theta,phi,data,thetaI,phiI));

    figure('Position',[5 -135 1000 1000])
    axesm('hammer','Frame','on','Grid','on');
    meshm(dataitoff,[1 90 180])
    colorbar('h');
end

```

## B Projected densities

### B.1 Five random $\sim 10^{11}M_{\odot}$ haloes at $z = 2.46$

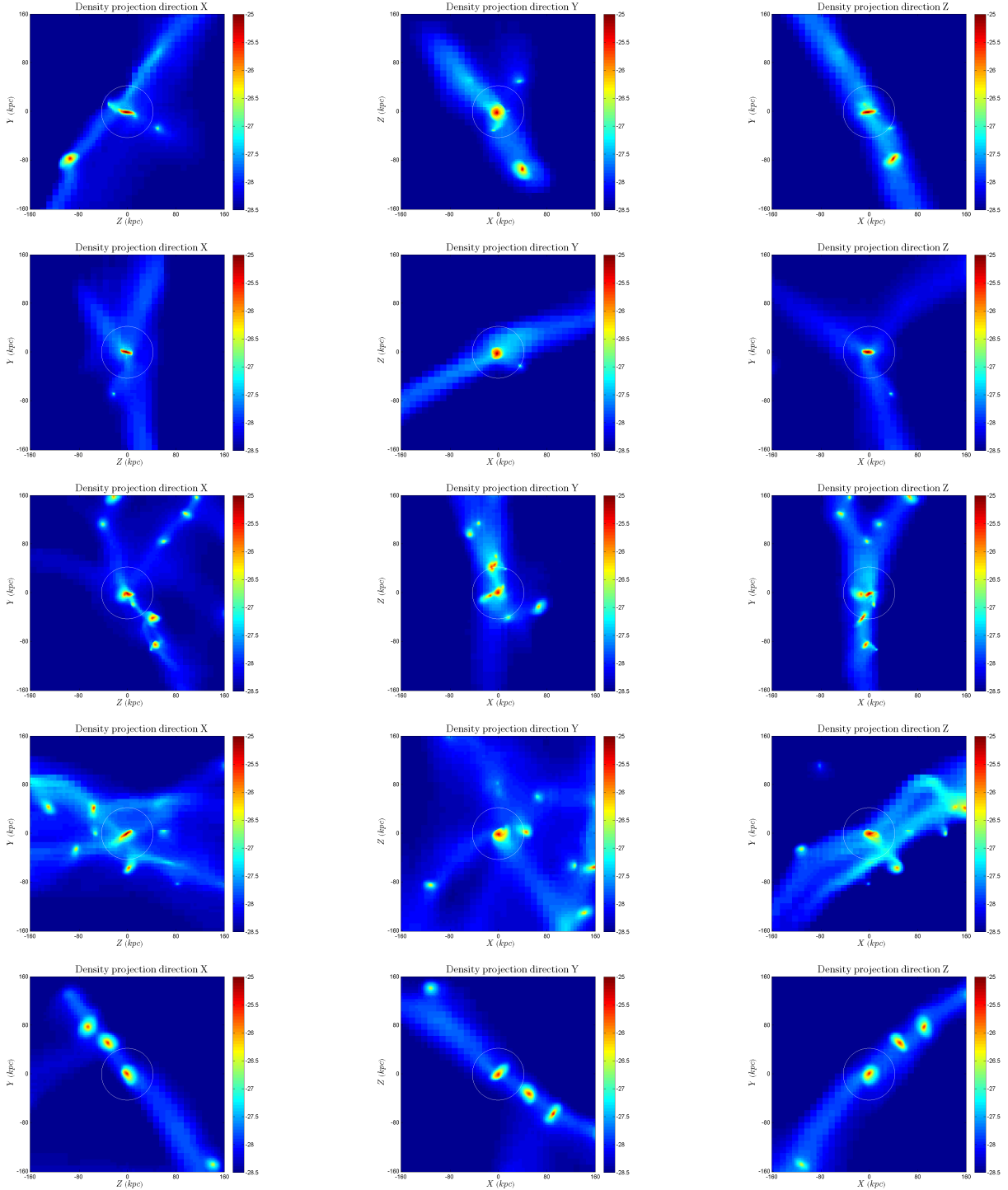


Figure 19: Five random  $\sim 10^{11}M_{\odot}$  haloes at  $z = 2.46$ : output 75, haloes 4340, 4341, 4342, 4344, and 4347. The white circle represents the virial radius.

## B.2 Five random $\sim 10^{12}M_{\odot}$ haloes at $z = 2.46$

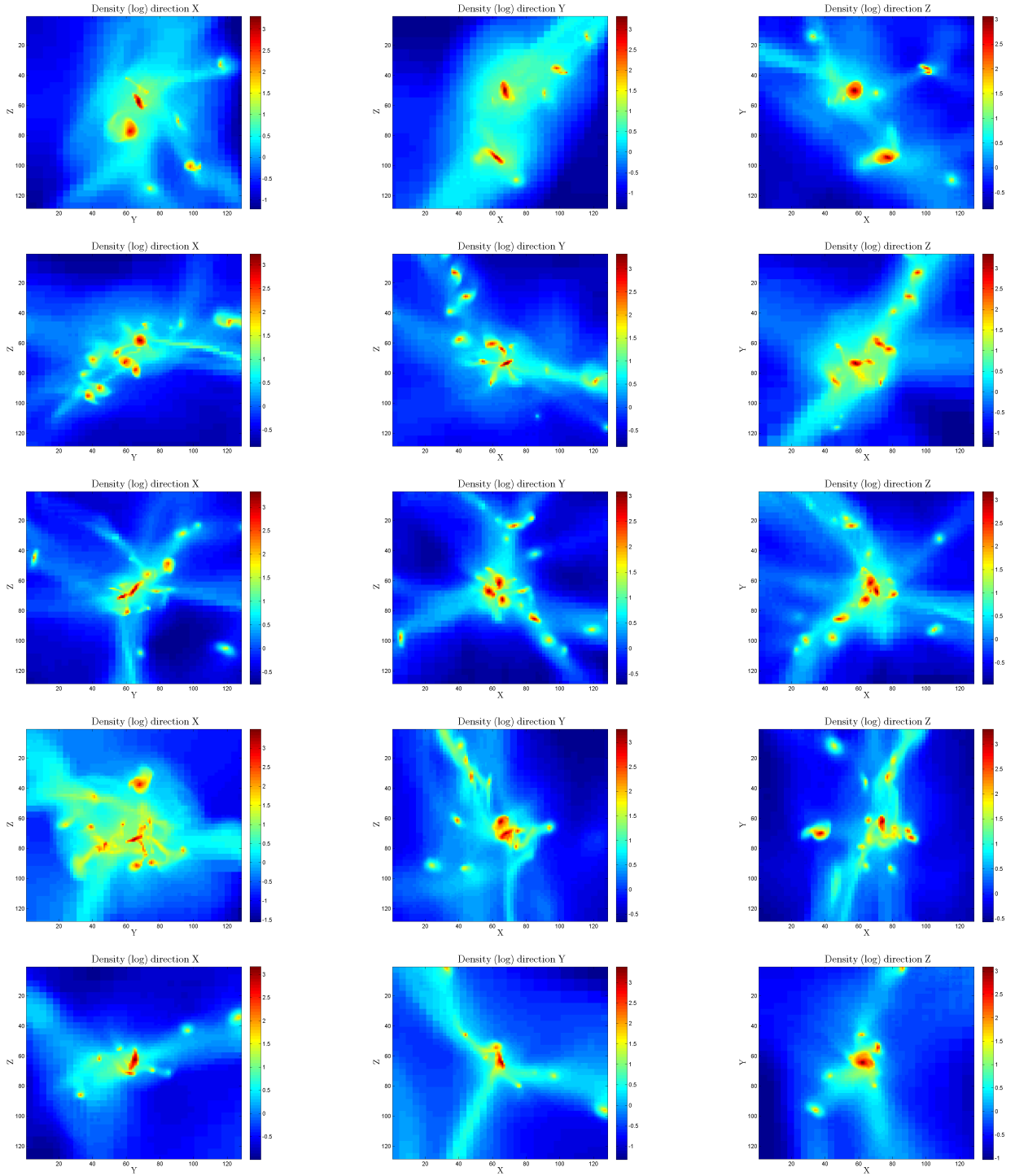


Figure 20: Five random  $\sim 10^{12}M_{\odot}$  haloes at  $z = 2.46$ : output 75, haloes 300, 307, 309, 310, and 314. The white circle represents the virial radius.

### B.3 Five random $\sim 10^{13} M_{\odot}$ haloes at $z = 2.46$

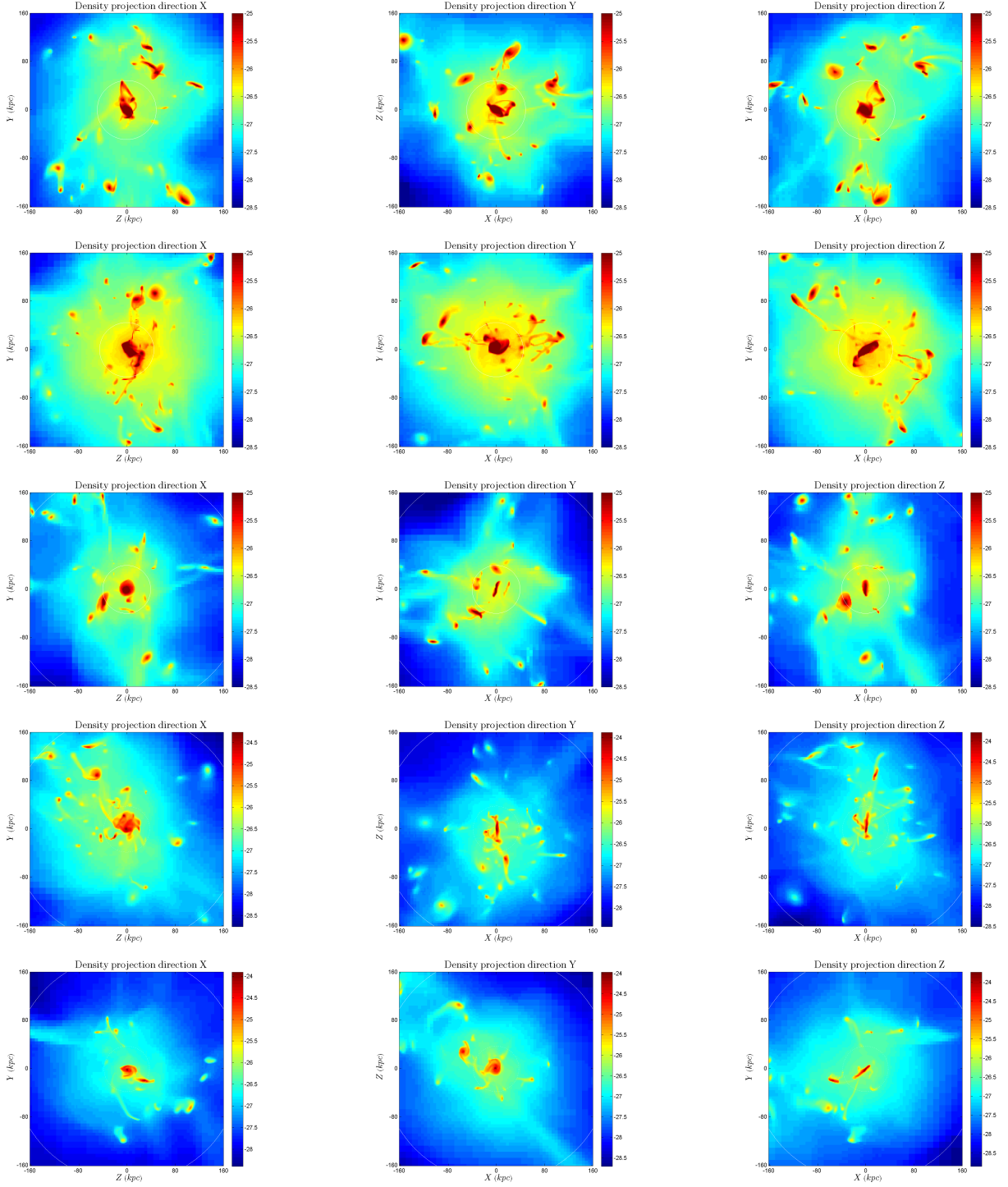


Figure 21: Five random  $\sim 10^{13} M_{\odot}$  haloes at  $z = 2.46$ : output 75, haloes 2, 3, 6, 10, and 13. The inner white circle represents  $0.2 R_{vir}$ .



### B.4 Five random $\sim 10^{12}M_{\odot}$ haloes at $z = 1.57$

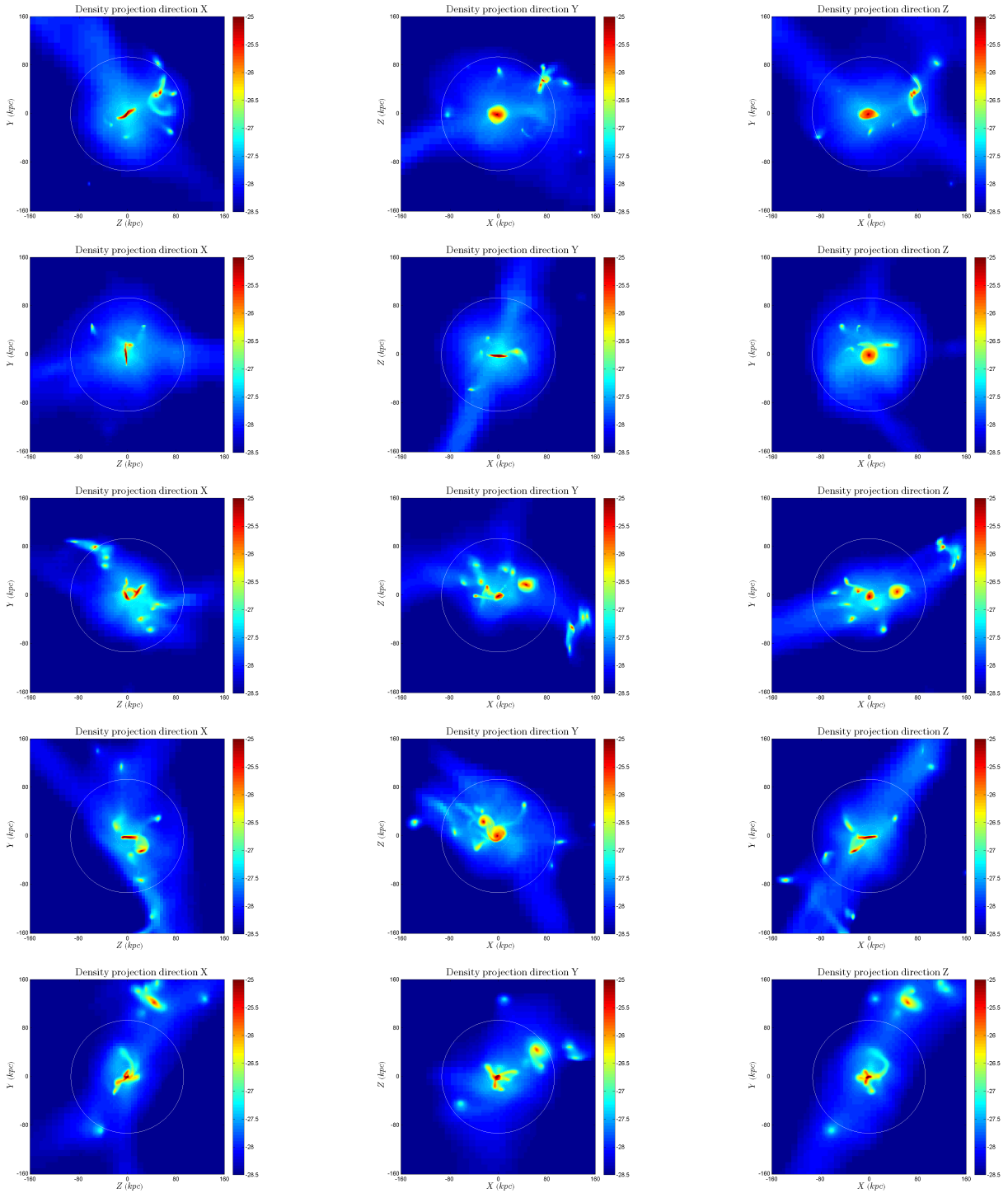


Figure 22: Five random  $\sim 10^{12}M_{\odot}$  haloes at  $z = 1.57$ : output 128, haloes 426, 427, 428, 429, and 433. The white circle represents the virial radius.

### B.5 Five random $\sim 10^{12}M_{\odot}$ haloes at $z = 4.01$

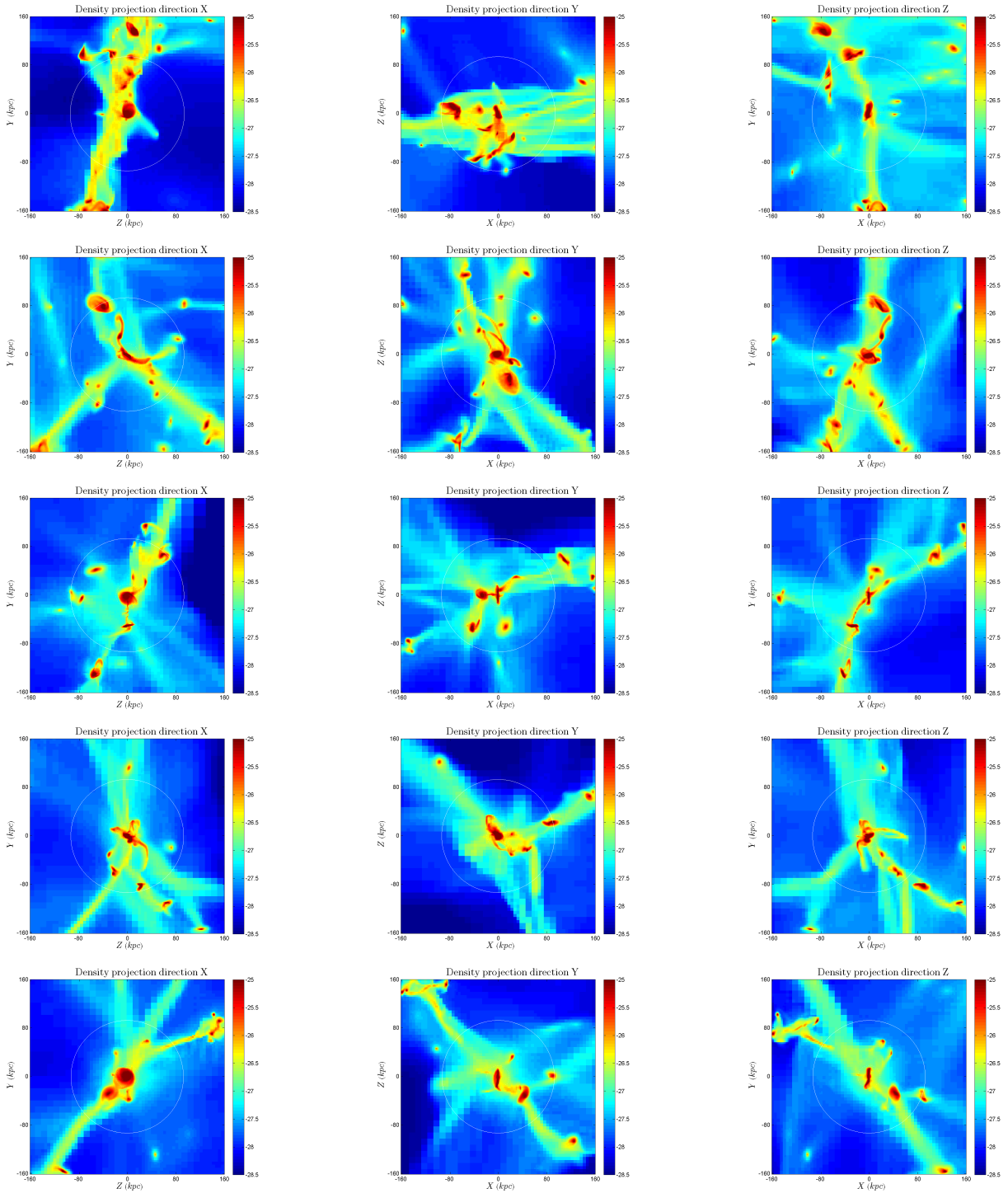


Figure 23: Five random  $\sim 10^{12}M_{\odot}$  haloes at  $z = 4.01$ : output 34, haloes 75, 76, 78, 81, and 82. The white circle represents the virial radius.

## C Slices for four $\sim 10^{12} M_{\odot}$ haloes at $z = 2.46$

### C.1 Halo 303 output 75

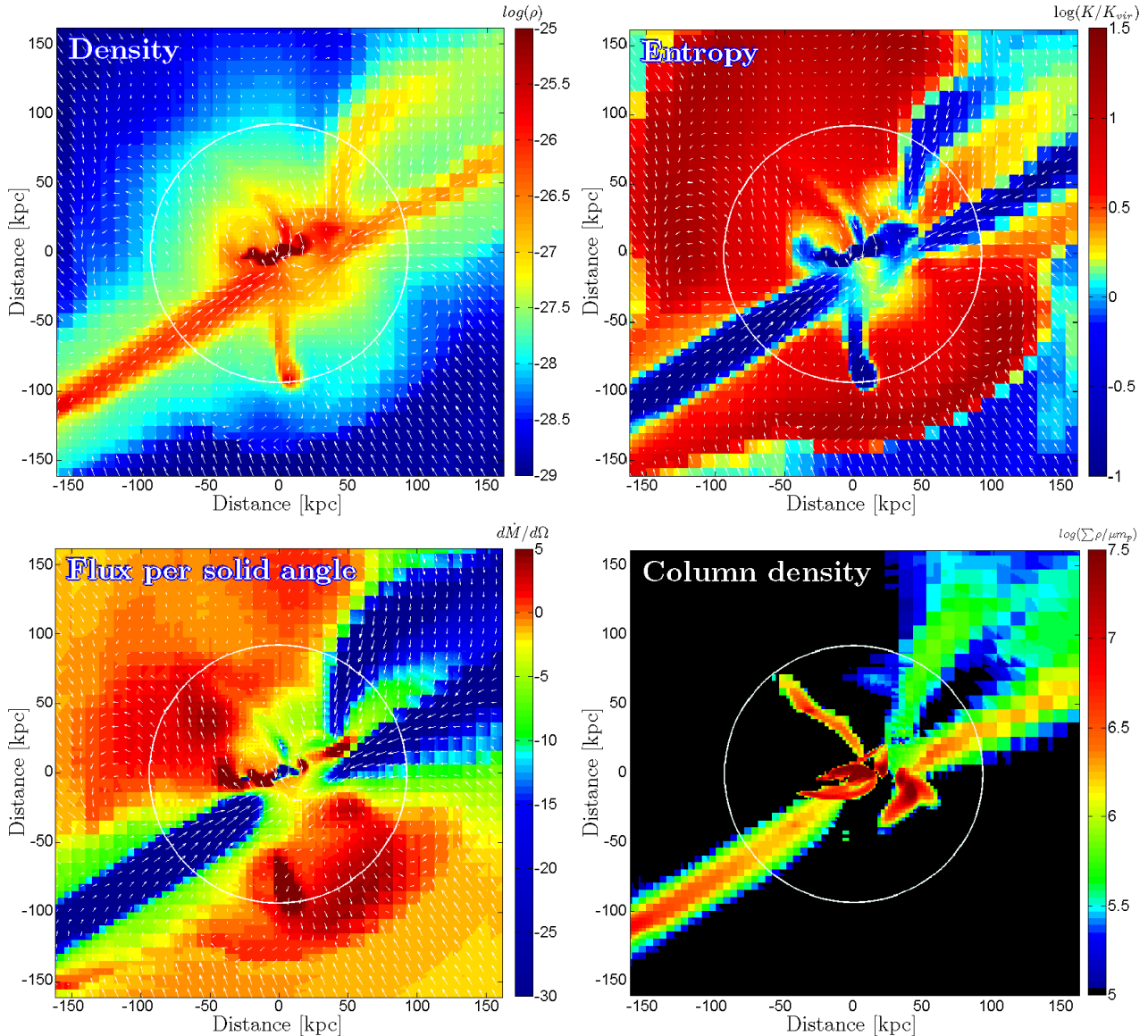


Figure 24: Gas maps in a thin slice and flux-selected column density through a galaxy of mass  $M_{vir} \approx 10^{12} M_{\odot}$  at redshift  $z = 2.46$ . Arrows describe the velocity field and the circle marks the halo virial radius. The density map emphasizes the narrowness of the streams and reveals that they are typically denser than the surrounding medium by more than an order of magnitude. The entropy  $K \propto T/\rho^{2/3}$  highlights the high-entropy medium filling the halo out to the virial shock and exhibits three radial low-entropy streams penetrating to the inner disk seen edge-on. The radial flux per solid angle,  $\dot{m} = r^2 \rho v_r$ , demonstrates that almost all the inward flux is channeled through the streams and the flux-selected column density map averages the density along a specified direction in the cells in which the flux per solid angle is higher than two times the virial flux.

## C.2 Halo 310 output 75

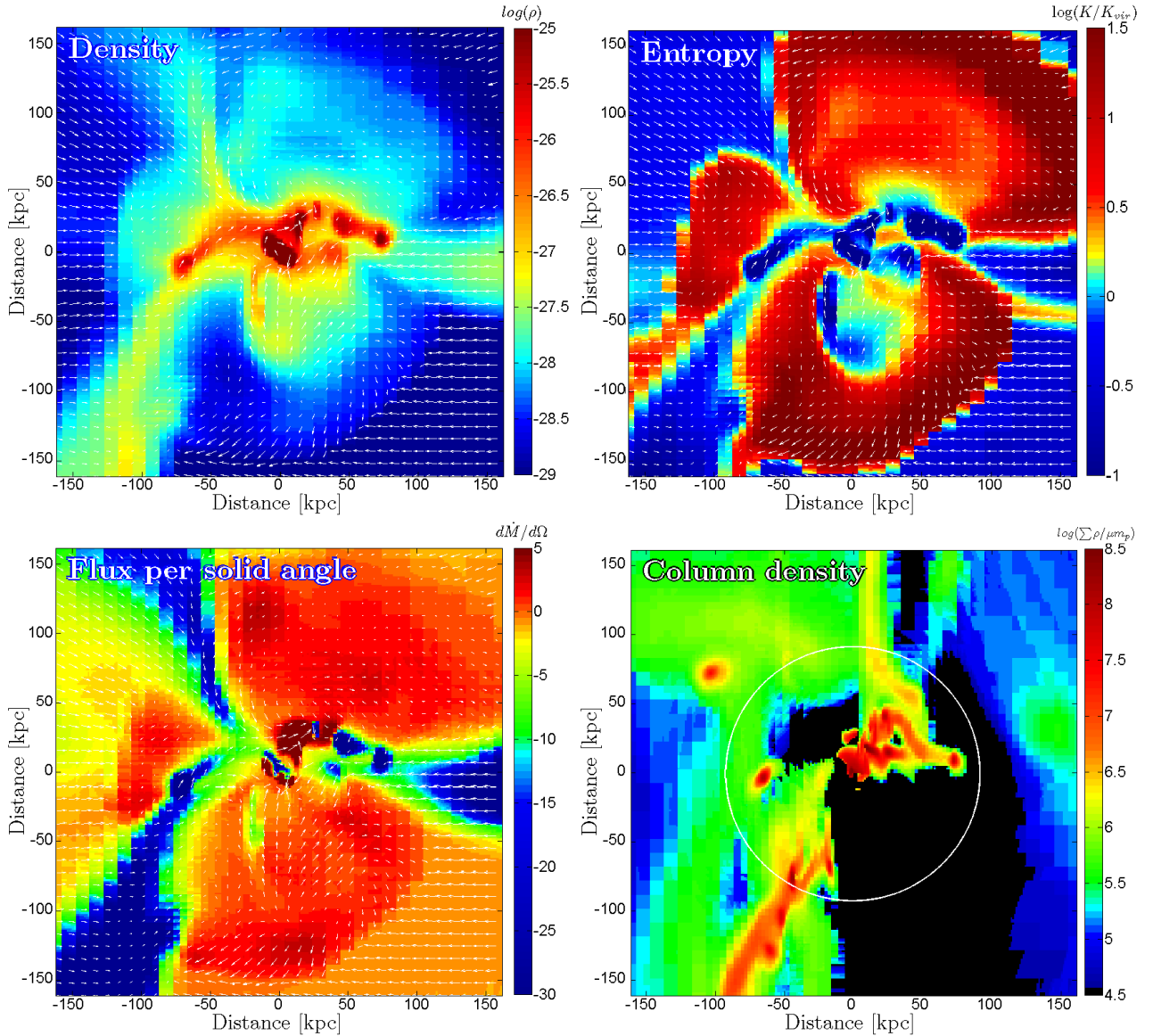


Figure 25: Gas maps in a thin slice and flux-selected column density through a galaxy of mass  $M_{vir} \approx 10^{12} M_{\odot}$  at redshift  $z = 2.46$ . Arrows describe the velocity field and the circle marks the halo virial radius. The density map emphasizes the narrowness of the streams and reveals that they are typically denser than the surrounding medium by more than an order of magnitude. The entropy  $K \propto T/\rho^{2/3}$  highlights the high-entropy medium filling the halo out to the virial shock and exhibits three radial low-entropy streams penetrating to the inner disk seen edge-on. The radial flux per solid angle,  $\dot{m} = r^2 \rho v_r$ , demonstrates that almost all the inward flux is channeled through the streams and the flux-selected column density map averages the density along a specified direction in the cells in which the flux per solid angle is higher than two times the virial flux.

## C.3 Halo 311 output 75

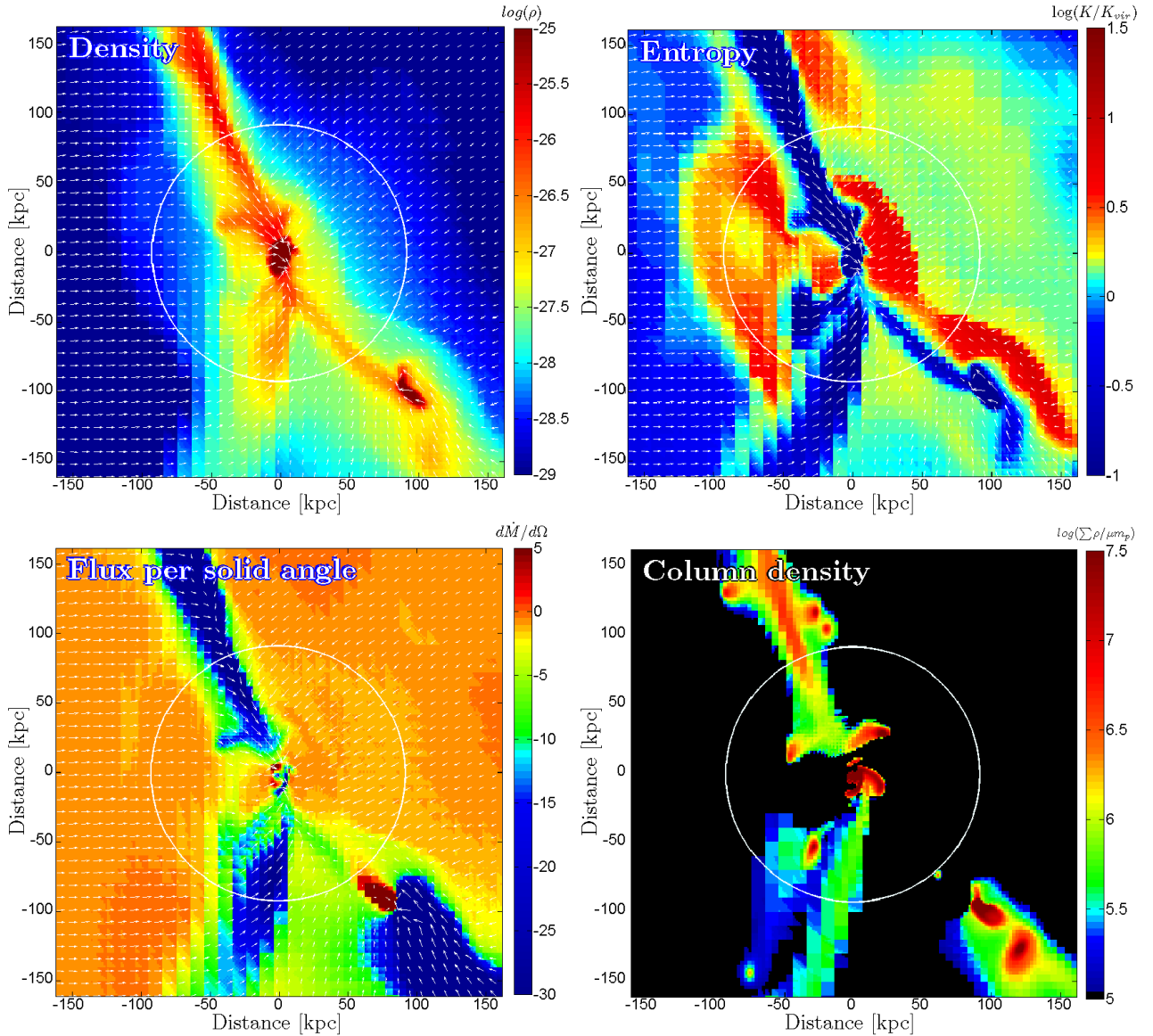


Figure 26: Gas maps in a thin slice and flux-selected column density through a galaxy of mass  $M_{vir} \approx 10^{12} M_{\odot}$  at redshift  $z = 2.46$ . Arrows describe the velocity field and the circle marks the halo virial radius. The density map emphasizes the narrowness of the streams and reveals that they are typically denser than the surrounding medium by more than an order of magnitude. The entropy  $K \propto T/\rho^{2/3}$  highlights the high-entropy medium filling the halo out to the virial shock and exhibits three radial low-entropy streams penetrating to the inner disk seen edge-on. The radial flux per solid angle,  $\dot{m} = r^2 \rho v_r$ , demonstrates that almost all the inward flux is channeled through the streams and the flux-selected column density map averages the density along a specified direction in the cells in which the flux per solid angle is higher than two times the virial flux.

## C.4 Halo 314 output 75

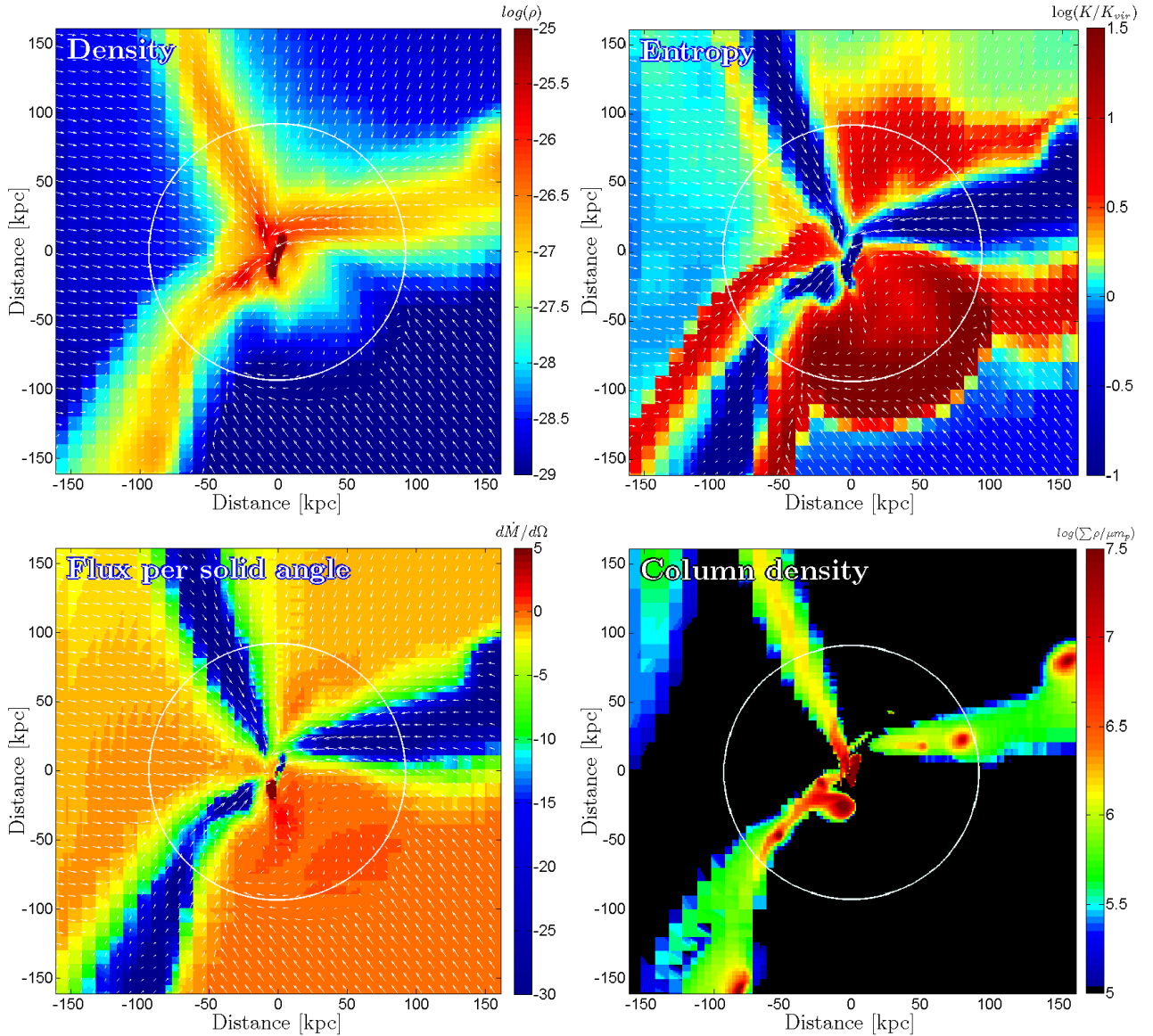


Figure 27: Gas maps in a thin slice and flux-selected column density through a galaxy of mass  $M_{vir} \approx 10^{12} M_{\odot}$  at redshift  $z = 2.46$ . Arrows describe the velocity field and the circle marks the halo virial radius. The density map emphasizes the narrowness of the streams and reveals that they are typically denser than the surrounding medium by more than an order of magnitude. The entropy  $K \propto T/\rho^{2/3}$  highlights the high-entropy medium filling the halo out to the virial shock and exhibits three radial low-entropy streams penetrating to the inner disk seen edge-on. The radial flux per solid angle,  $\dot{m} = r^2 \rho v_r$ , demonstrates that almost all the inward flux is channeled through the streams and the flux-selected column density map averages the density along a specified direction in the cells in which the flux per solid angle is higher than two times the virial flux.



## D Workshop poster: *New understanding of galaxy evolution*

Joint Research Workshop of the Institute for Advanced Studies & the Israel Science Foundation

מכון  
ליידים  
מתקדמים  
Institute for  
Advanced  
Studies

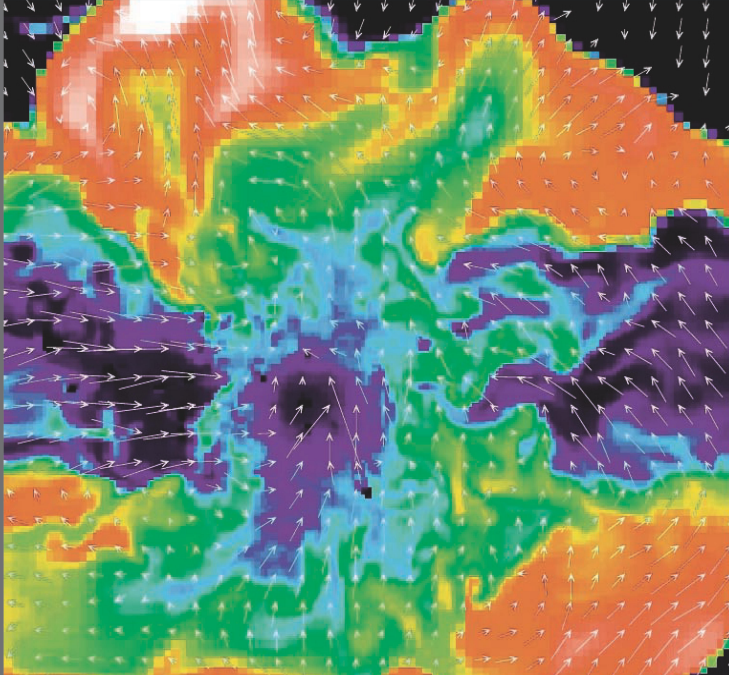
מכון  
ליידים  
מתקדמים  
Institute for  
Advanced  
Studies

# New Understanding of Galaxy Evolution

Directors: **Avishai Dekel** and **Sandra M. Faber**

**THEME**

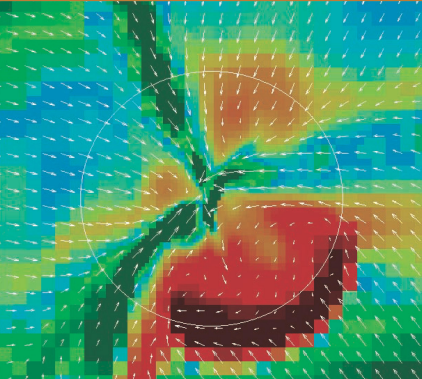
*New observational programs, from space and from the ground at different wavelengths, are providing unprecedented data on the properties of galaxies as they were when the universe was only a few billion years old. This opens a new era in the study of galaxy formation and evolution within the cosmological model dominated by dark matter and dark energy. Together with the rapid advance in our theoretical understanding and supercomputer modeling, this allows for breakthroughs in our understanding of how galaxies have formed and evolved. The two-week workshop brings together world experts to study the major open issues in the theory of galaxy formation. The program consists of a daily organized discussion session followed by collaborative work in small groups.*



**June 11-24  
2008**

**PARTICIPANTS**  
**Yuval Birnboim**, The Hebrew U & Harvard / **James Bullock**, UC Irvine / **Andrea Cattaneo**, Potsdam / **Daniel Ceverino**, New Mexico SU & The Hebrew U / **Darren Croton**, UC Berkeley / **Avishai Dekel**, The Hebrew U / **Aaron Dutton**, UC Santa Cruz / **Sandra M. Faber**, UC Santa Cruz / **Orly Gnat**, Caltech / **Tobias Goerdt**, The Hebrew U / **Yehuda Hoffman**, The Hebrew U / **Neal Katz**, U of Massachusetts / **Anatoly Klypin**, New Mexico SU / **Andrey Kravtsov**, U of Chicago / **Noam Libeskind**, The Hebrew U & Potsdam / **Arieh Maller**, NY / **Gary Mamon**, IAP Paris / **Zacharia Myers**, Technion / **Smadar Naoz**, Tel Aviv U / **Julio Navarro**, U of Massachusetts / **Adi Nusser**, Technion / **Eyal Neistein**, The Hebrew U & MPA Garching / **Hagai Netzer**, Tel Aviv U / **Jeremiah P. Ostriker**, Princeton U / **Joel R. Primack**, UC Santa Cruz / **Ravi Sheth**, U of Penn / **Rachel Somerville**, Space Telescope Sci / **Amiel Sternberg**, Tel Aviv U / **Romain Teyssier**, Saclay, France / **Jeremy Tinker**, U of Chicago / **Risa Wechsler**, Stanford U / **Joanna Woo**, The Hebrew U / **Elad Zinger**, The Hebrew U

For program details please see IAS website:  
[www.as.huji.ac.il/workshops/isf/galaxy/](http://www.as.huji.ac.il/workshops/isf/galaxy/)



**E Submitted *Nature* article: *Massive galaxy formation by cold streams***

# Massive Galaxy Formation by Cold Streams

A. Dekel<sup>1</sup>, Y. Birnboim<sup>1</sup>, G. Engel<sup>1</sup>, J. Freundlich<sup>1,2</sup>, T. Goerdt<sup>1</sup>, M. Mumcuoglu<sup>1</sup>, E. Neistein<sup>1</sup>, C. Pichon<sup>3</sup>, R. Teyssier<sup>4</sup>, & E. Zinger<sup>1</sup>

<sup>1</sup>Racah Institute of Physics, The Hebrew University, Jerusalem 91904, Israel

<sup>2</sup>Department de Physique, Ecole Normale Supérieure, 24 rue Lhomond, 75231 Paris cedex 05, France

<sup>3</sup>Institut d'Astrophysique de Paris and UPMC, 98bis Boulevard Arago, Paris 75014, France

<sup>4</sup>Institut de Recherches sur les lois Fondamentales de l'Univers, DSM, l'Orme des Merisiers, 91198 Gif-sur-Yvette, France

The massive galaxies in the young universe, ten billion years ago, form stars at surprising intensities<sup>1,2</sup>. While they were commonly attributed to violent mergers, many of them are extended rotating discs incompatible with mergers<sup>3,2,4</sup>. In order to decipher this phenomenon, we use a cutting-edge cosmological simulation<sup>5</sup> and clustering theory<sup>6,7</sup> to explore how these galaxies acquired their gas. We find that these are “Stream-Fed Galaxies”, growing via steady, narrow, cold gas streams, which penetrate effectively through the shock-heated media of dark-matter haloes as massive as the Milky Way’s<sup>8</sup>. Half the stream mass is in clumps leading to mergers of mass ratio 1:10 or higher, and half is in smoother flows. Since the merger duty cycle is 0.1, three-quarters of the galaxies forming stars at a given rate are fed by smooth streams. Unlike destructive major mergers, the smoother flows can keep the discs intact, though thick and perturbed. The observed abundance of star-forming galaxies implies that the inflowing gas turns into stars at maximum efficiency. In contrast, the sub-millimeter galaxies that form stars even more intensely<sup>1</sup> are largely compact merger-induced starbursts in haloes twice as massive.

---

## Star-Formation Rate versus Halo Growth Rate

It appears that the most effective star formers in the universe were galaxies of stellar and gas mass on the order of  $10^{11} M_{\odot}$  at redshifts  $z = 2 - 3$ <sup>9,2</sup>, when the universe was about 3 Gyr old. The common cases<sup>3,2</sup> show star-formation rates (SFR) of  $100 - 200 M_{\odot} \text{ yr}^{-1}$ . These include UV-selected galaxies termed BX/BM, and rest-frame optically selected galaxies termed sBzK, which we jointly refer to as “Star-Forming Galaxies” (SFG). Their SFR is much higher than the  $4 M_{\odot} \text{ yr}^{-1}$  in the Milky Way today, while their characteristic dynamical time is only about 5 times shorter. The comoving space density of SFGs is  $n \simeq 2 \times 10^{-4} \text{ Mpc}^{-3}$ , implying within the standard  $\Lambda$ CDM cosmology that they reside in dark-matter haloes of masses  $\lesssim 3.5 \times 10^{12} M_{\odot}$ . In parallel, the most extreme star formers are observed as dusty objects, termed Sub-Millimeter Galaxies (SMG)<sup>10,11</sup>, with SFRs up to  $\sim 1,000 M_{\odot} \text{ yr}^{-1}$  and  $n \simeq 2 \times 10^{-5} \text{ Mpc}^{-3}$ . While the SMGs could largely be starbursts induced by major mergers, the morphology and kinematics of the SFGs indicate extended, thick rotating discs that are incompatible with the expected compact or highly perturbed appearance of ongoing major mergers<sup>3,2,12,4</sup>. The big puzzle is how massive galaxies form most of their stars so efficiently at early times and not through major mergers, given that there is no equivalent phenomenon in today’s universe and its origin is not obvious



theoretically. A necessary condition is clearly a steady, rapid gas supply into appropriately massive discs at early epochs.

One should first verify that the required rate of gas supply is compatible with the predicted growth rate of the corresponding dark-matter haloes in the standard cosmological model. The average growth rate of halo virial mass  $M_v$ , via mergers and smooth accretion, is derived<sup>6</sup> based on the EPS theory of gravitational clustering<sup>13</sup> (Methods). It resembles the assembly rate in cosmological  $N$ -body simulations<sup>14,15</sup>. For the  $\Lambda$ CDM cosmology (a flat universe with 72% dark energy, mass dominated by cold dark matter, and fluctuation normalization parameter  $\sigma_8 = 0.8$ )<sup>16</sup>, the corresponding growth rate of the baryonic component is well fitted by the practical formula<sup>6</sup>

$$\dot{M} \simeq 6.6 M_{12}^{1.15} (1+z)^{2.25} f_{.165} M_{\odot} \text{ yr}^{-1}, \quad (1)$$

where  $M_{12} \equiv M_v/10^{12}M_{\odot}$ , and  $f_{.165}$  is the baryonic fraction in the matter assembled into haloes in units of the cosmological value  $f_b = 0.165$ . Thus, at  $z = 2.2$ , the average baryonic growth rate of haloes of  $2 \times 10^{12}M_{\odot}$  is predicted to be  $\dot{M} \simeq 200 M_{\odot} \text{ yr}^{-1}$ , fairly sufficient for feeding the SFR observed in SFGs. However, this is not by a large margin, implying that (a) the incoming material must be mostly gaseous, (b) the cold gas must very efficiently penetrate deep into the inner halo, and (c) the SFR must closely follow the gas supply rate.

### Penetrating Cold Narrow Streams

The required efficient penetration into the inner halo is not a trivial matter, given that the indicated halo masses of  $M_v > 10^{12}M_{\odot}$  are above the threshold for virial shock heating<sup>17,18,19,8</sup>,  $M_{\text{shock}} \lesssim 10^{12}M_{\odot}$ . Such haloes are encompassed by a stable shock near their outer radius  $R_v$ , inside which gravity and thermal energy are in virial equilibrium. Infalling gas through the virial shock is expected to heat up to the virial temperature and stall in quasi-static equilibrium before it can cool and gradually rain into the inner galaxy<sup>20</sup>. However, Dekel & Birnboim<sup>8</sup> have conjectured that at  $z \geq 2$ , these hot massive haloes are penetrated by narrow cold streams. The reason is that at early times, the haloes of  $M_v > M_{\text{shock}}$  populate the extreme massive tail of the halo mass distribution. As such, they are fed by dark-matter filaments from the cosmic web that are narrow compared to  $R_v$  and denser than the mean density within the halo. The enhanced density of the gas that streams along these filaments allows it to cool more rapidly than the dynamical compression rate behind a shock and thus avoid the shock heating that occurs elsewhere in the halo (Supplementary Information).

To test this conjecture, we study the way gas feeds massive high- $z$  galaxies in the MareNostrum simulation - a hydrodynamical simulation in a comoving cosmological box of  $50 h^{-1}\text{Mpc}$  and a resolution of  $\sim 1 h^{-1}\text{kpc}$  at the galaxy centers (Methods). Fig. 1 maps the entropy and inward flux of gas in a thin slice centered on one typical galaxy of  $M_v = 10^{12}M_{\odot}$  at  $z = 2.5$ . It demonstrates that the shock-heated, high-entropy, low-flux medium that fills most of the halo out to  $R_v$  and beyond is penetrated by three massive, narrow streams of low-entropy gas. They flow into the central disc with a radial flux per solid angle several times the average virial flux as estimated from eq. (1). The opening angle of a typical stream at  $R_v$  is  $20 - 30^\circ$ , so the streams cover a total area of  $\sim 0.4 \text{ rad}^2$ , namely a few percent of the sphere. The flux map in Fig. 2 displays the three-dimensional structure of the streams and uncovers clumps along two of them.

The penetration through the halo into the center can be evaluated via the profiles of total mass inflow rate  $\dot{M}(r)$  through shells of radius  $r$ , obtained by integrating  $\rho v_r r^2 d\Omega$  over a shell, where  $\rho$  is the gas density,  $v_r$  the radial velocity, and  $d\Omega$  the angular-area element. Fig. 3 displays the average flux profile over the simulated galaxies of  $M_v \simeq 10^{12}M_{\odot}$  at  $z = 2.5$ , on top of the profiles of four representative cases (Supplementary Information). The average profile reveals that the total flux remains roughly constant from well outside the virial radius ( $\sim 90 \text{ kpc}$ ) all the way to the disc vicinity inside  $r \sim 15 \text{ kpc}$ . The inflow rate of  $\sim 100 M_{\odot} \text{ yr}^{-1}$  is consistent with the virial growth rate predicted by eq. (1). Apparently, the flux decay while traveling through the halo is roughly compensated by the higher cosmological flux when that gas entered the halo, eq. (1), leading to the apparent constancy of flux with radius.

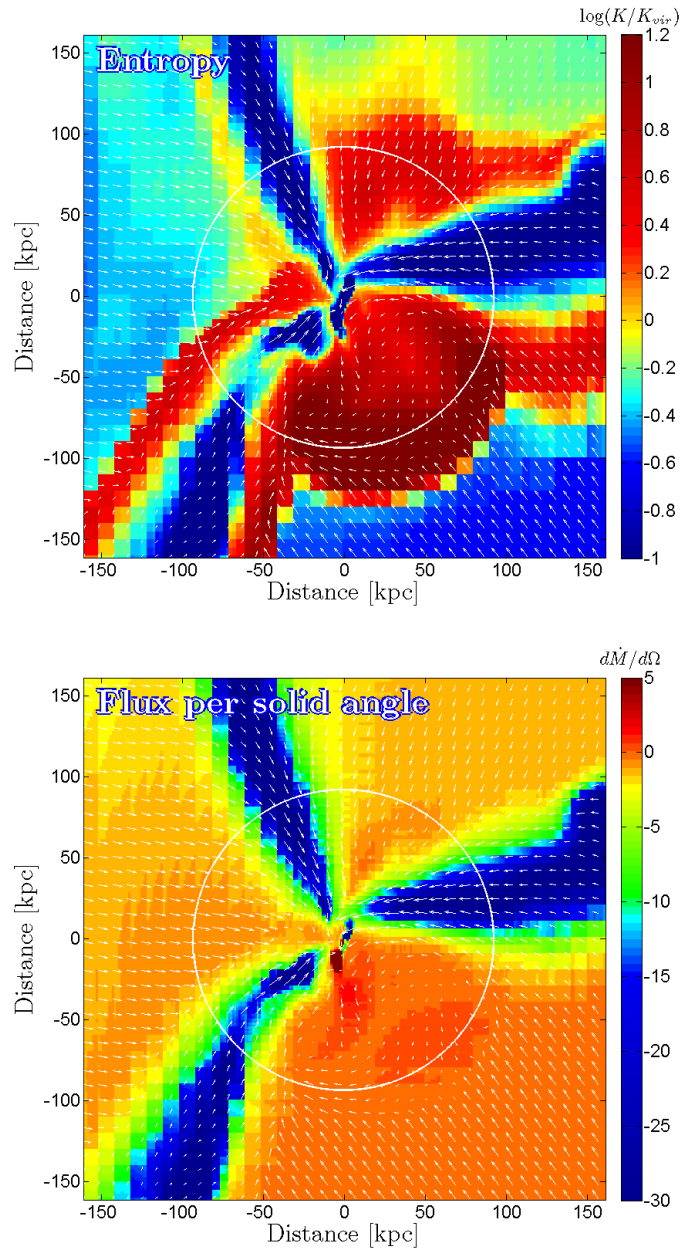


Figure 1: Gas maps in a thin slice through a galaxy of  $M_v = 10^{12} M_\odot$  at  $z = 2.5$ . Arrows describe the velocity field and the circle marks the halo virial radius  $R_v$ . The **entropy**,  $K \propto T/\rho^{2/3}$ , highlights (in red) the high-entropy medium filling the halo out to the virial shock near  $R_v$ . It exhibits three, radial, low-entropy streams (blue) penetrating into the inner disc seen edge-on. The radial **flux** per solid angle,  $\dot{m} = r^2 \rho v_r$ , demonstrates that almost all the inward flux is channeled through the streams (blue), at a rate that remains roughly the same at all radii. This rate is several times higher than the spherical average outside the virial sphere,  $\dot{m}_{\text{vir}} \simeq 8 M_\odot \text{yr}^{-1} \text{rad}^{-2}$ .

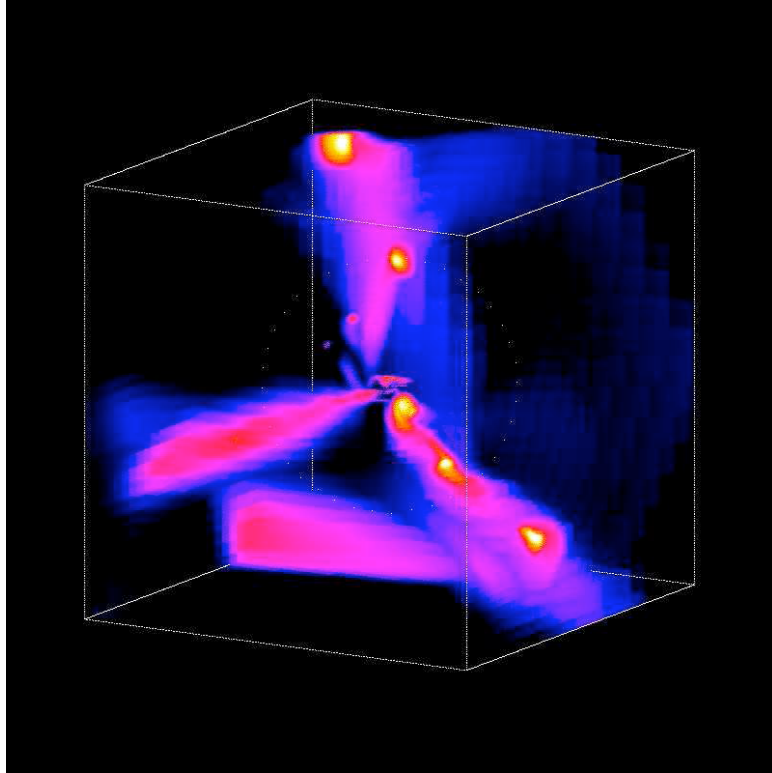


Figure 2: Flux map of the galaxy shown in Fig. 1, highlighting the three-dimensional structure of the streams in a box of side 320 kpc. The colors refer to inflow rate per solid angle of point-like tracers at the centers of the cubic grid cells. Two of the three radial streams show gas clumps of mass on the order of one tenth of the central galaxy.

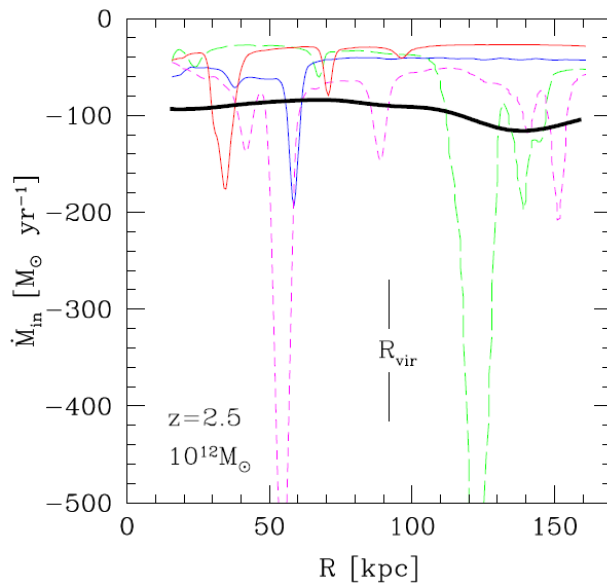


Figure 3: Gas inflow rate through spherical shells of radius  $r$ , from the disc vicinity to almost twice the halo virial radius. The thick black curve is the average over the simulated galaxies of  $M_v \simeq 10^{12} M_{\odot}$  at  $z = 2.5$ , showing deep penetration at a roughly constant rate. The colored curves refer to four representative galaxies, two showing clumps of  $\mu \gtrsim 0.1$  and two with smoother flows involving only mini-minor clumps of  $\mu < 0.1$ .

## Abundance of Gas Inflow Rates

In order to relate to the observed abundance of galaxies as a function of SFR, we use the MareNostrum flux profiles to evaluate  $n(>\dot{M})$ , the comoving number density of galaxies with an instantaneous gas-flow rate higher than  $\dot{M}$ . We first extract from the simulated flux profiles the conditional probability distribution at a given mass,  $P(\dot{M}|M_v)$ . It is done by sampling the  $\dot{M}(r)$  profiles uniformly in  $r$ , given that the inflow velocity along the stream is roughly constant (Methods & Supplementary Informations). This is convolved with the halo mass function  $n(M_v)$ , based on the Sheth-Tormen approximation<sup>21</sup>, to provide

$$n(\dot{M}) = \int_0^\infty P(\dot{M}|M_v) n(M_v) dM_v . \quad (2)$$

The desired cumulative abundance  $n(>\dot{M})$  is obtained by integration from  $\dot{M}$  to infinity, and shown at  $z = 2.2$  in the upper curve of Fig. 4. We see that galaxies with  $\dot{M} > 150 M_\odot \text{yr}^{-1}$  are expected at a comoving number density  $n \sim 3 \times 10^{-4} \text{Mpc}^{-3}$ . Fluxes as high as  $\dot{M} > 500 M_\odot \text{yr}^{-1}$  are anticipated at  $n \sim 6 \times 10^{-5} \text{Mpc}^{-3}$ . It is encouraging to note that this theoretical prediction lies safely above the observed values as indicated by the symbols. However, the difference between the gas supply rate and SFR is only by a factor of order 2, confirming our earlier conclusion that once the gas reaches the disc, it should very efficiently convert into stars on a dynamical time scale.

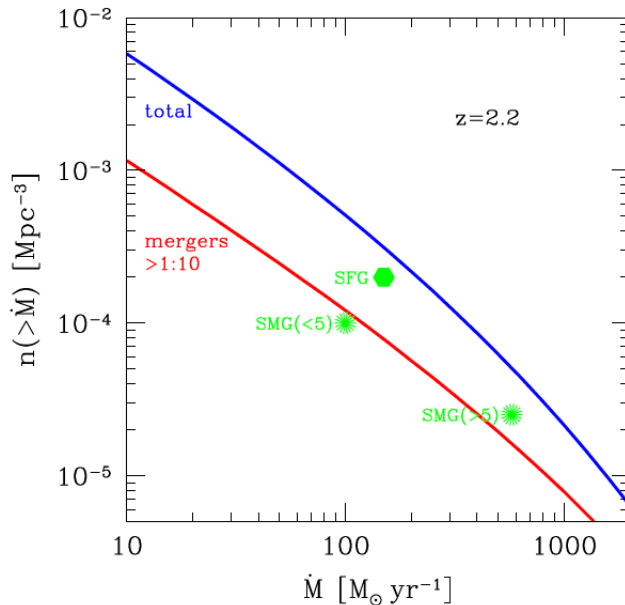


Figure 4: Comoving number density of galaxies with gas inflow rate higher than  $\dot{M}$  at  $z = 2.2$ , as predicted from our analysis of the cosmological simulation. The upper curve refers to total inflow, and the lower curve is limited to gas input by  $\mu > 0.1$  mergers. The symbols represent the vicinity of where the observed massive star-forming galaxies can be put once the observed SFR is identified with  $\dot{M}$ . The sBzK/BX/BM galaxies are marked SFG<sup>10</sup>. The SMGs brighter and fainter than 5 mJy are marked accordingly<sup>10,9</sup>. The gas inflow rate is sufficient for the SFR, but the small margin implies that the SFR must closely follow the gas supply. Most of the massive star formers should be observed while being fed by smooth flows rather than undergoing mergers.

## Smooth Flows versus Mergers

By analyzing the clumpiness of the gas streams, we address the role of major mergers versus smooth flows in the disc buildup and star formation. Fig. 2 exhibits five obvious clumps along the streams. The sample profiles in Fig. 3 reveal the clumps as narrow peaks of inward flux. We evaluate each clump mass by integrating  $M_{\text{clump}} = \int \dot{M}(r) dr/v_r(r)$  across the peak, and estimate a mass ratio for the expected merger of the clump with the central galaxy by  $\mu = M_{\text{clump}}/(f_b M_v)$ , ignoring mass loss in the clump on its way in. We term “merger”

any major or minor merger of  $\mu \geq 0.1$ , as opposed to “mini-minor” mergers where  $\mu < 0.1$ , which we refer to as “smooth” flows. Fig. 3 shows two galaxies with  $\mu > 0.1$  clumps inside  $2R_v$ , and two involving only smoother flows in this radius range. We find that about half the mass is flowing in as mergers and half as smoother flows. However, for  $M_v \sim 10^{12} M_\odot$  and  $z \sim 2.2$ , the duty cycle of mergers in a galaxy history is only  $\eta \lesssim 0.1$ , i.e., less than one out of ten galaxies is undergoing a merger at any given time.

It is encouraging to note that a similar estimate can be obtained from an EPS-based prediction, by reading from Fig. 6 of Neistein & Dekel<sup>7</sup> the rate  $dN/d\omega$  of mergers into a halo  $M_v$  with mass ratio  $> \mu$ . For the typical starburst duration we assume  $\Delta t \simeq 0.1 R_v / V_v$  (namely  $\sim 50$  Myr at  $z = 2.5$ ), based on merger simulations<sup>22</sup>. A similar estimate is derived from the typical peak width in the  $M(r)$  profiles of Fig. 3, with streaming at the virial velocity,  $(GM_v/R_v)^{1/2} \sim 220 \text{ km s}^{-1}$ . This leads to  $\eta = (dN/d\omega)\Delta t \simeq 0.09$  for  $M = 2 \times 10^{12} M_\odot$  at  $z = 2.2$ .

The lower curve in Fig. 4 is obtained similarly to the upper curve, but using only the gas fed by mergers ( $\mu > 0.1$ ). From the difference between the two curves we learn that among the galaxies of a given  $\dot{M}$ , only about a quarter are predicted to be seen while undergoing a merger. The fact that the symbol representing typical SFGs (sBzK and BM/BX galaxies) lies well above the lower, merger curve indicates that in most of them the star formation is driven by smooth flows rather than mergers. This may explain why these galaxies maintain an extended thick disc while doubling their mass over a halo crossing time<sup>4</sup>. On the other hand, as seen in Fig. 4, about half the bright SMGs (with flux  $> 5 \text{ mJy}$ ), and most of the fainter SMGs, are consistent with being merger-induced starbursts<sup>10</sup>.

## Conclusion

The cosmological gas accretion rate into galactic haloes of  $\gtrsim 10^{12} M_\odot$  at  $z = 2-3$  is sufficient to explain the observed abundance of high star-formation rates, but only barely so. This implies that the transition from accretion at the virial radius to SFR in a central galaxy has to be very efficient<sup>2,4</sup>. Indeed, our simulation reveals that the cold gas is poured into the center of each halo via a few steady narrow streams, riding the dark-matter filaments of the cosmic web, and very effectively penetrating through the shock-heated medium that otherwise fills the halo. A large fraction of the baryons comes in as mini-minor clumps, or smooth flows. The more clumpy input component, which involves about half the incoming mass, is also gas rich. We read from Fig. 4 that at a given SFR, the abundance of galaxies forming stars by smooth streams is  $\sim 3$  times higher than the merger-induced starbursts. The Star-Forming Galaxies are predominantly fed by smooth flows, and can thus be interpreted as “Stream-Fed Galaxies”. The same is true for a non-negligible fraction of the bright SMGs, the rest being driven by  $\gtrsim 1:10$  mergers.

One should note that the intense SFR associated with streams must be limited to galaxies of  $\sim 10^{11} M_\odot$  in order not to violate the observational constraints on the overall density of SFR at these epochs<sup>11,23</sup>. Star formation must be suppressed in much smaller galaxies, possibly due to stellar feedback<sup>24,25,8</sup>. For completeness, it is also interesting to note that about half the  $\sim 10^{11} M_\odot$  galaxies at  $z \sim 2.2$  have suffered a major merger during the preceding  $\sim 1.5 \text{ Gyr}$ , as well as drastic heating by an expanding shock<sup>20,26</sup> (Libeskind, N., Birnboim, Y. & Dekel, A., in preparation), so many of them are expected to be compact spheroids of low SFR rather than extended massive star formers<sup>27,28</sup>. This implies an even tighter correspondence between the gas input rate and the SFR.

## METHODS

**Halo Growth by EPS.** Neistein et al.<sup>6</sup> used the EPS<sup>13</sup> theory of cosmological clustering into spherical haloes in virial equilibrium to derive a robust approximation for the average growth rate of halo virial mass  $M_v$ ,

$$d \ln M_v / d\omega = -(2/\pi)^{1/2} [\sigma^2(M_v/q) - \sigma^2(M_v)]^{-1/2}, \quad \omega \equiv \delta_c / D(t). \quad (3)$$

The time variable  $\omega$ , which makes the expression time invariant, is inversely proportional to  $D(t)$ , the linear growth rate of density fluctuations at time  $t$  in the assumed cosmology, with  $\delta_c \simeq 1.68$ . The power spectrum of

initial density fluctuations enters via the variance  $\sigma^2(M_v)$ . The constant  $q$  is 2.2 with an uncertainty of  $\pm 0.1$  intrinsic to the EPS theory. Eq. (3) has been confirmed to resemble the assembly rate in cosmological  $N$ -body simulations<sup>14</sup>.

**The MareNostrum simulation.** The cosmological simulation<sup>5,29</sup> used in the present analysis has been performed with the Eulerian AMR code RAMSES<sup>30</sup> on 2,048 processors of the MareNostrum supercomputer. The code simulates the coupled gas and dark-matter dynamics, using a Particle-Mesh scheme for the dark-matter component and a second-order Godunov scheme for the gas component. In order to describe the formation of dense star-forming discs, the code includes metal-dependent radiative cooling, UV heating by a standard photo-ionizing background, star formation, supernovae feedback and metal enrichment. The simulation box of comoving  $50 h^{-1}\text{Mpc}$  involved  $1,024^3$  dark-matter particles and  $4 \times 10^9$  gas cells. Using a quasi-Lagrangian refinement strategy, the spatial resolution reaches  $\sim 1 h^{-1}\text{kpc}$  in physical units at all times. The dark-matter particle mass is  $\sim 10^8 M_\odot$ , so each of the haloes studied here consists of  $\sim 10^4$  particles within the virial radius. Since one can reliably describe the formation of haloes down to  $\sim 100$  particles<sup>31</sup>, namely  $\sim 10^{10} M_\odot$ , the  $10^{12} M_\odot$  haloes addressed here are two orders of magnitude above the minimum halo mass. This simulation allows us to capture the important properties of gas accretion into galaxies in more than 100 haloes of  $\sim 10^{12} M_\odot$  at  $z \sim 2.5$ , thus providing a large statistical sample. A first analysis of galaxies from this simulation<sup>5</sup> have confirmed the bi-modal nature of cold flows and hot media as a function of mass and redshift<sup>8</sup>.

Our current analysis is based on robust features that are properly simulated, such as the large-scale structure of the streams, the total flux in them, and the gas clumps more massive than  $\sim 10^{10} M_\odot$ . However, the finite resolution does not allow a fair treatment of small-scale gas phenomena such as turbulence in the hot gas, ram-pressure stripping of clumps, hydrodynamical instabilities at the stream boundaries, and the formation of small clumps. Furthermore, the current resolution does not allow a detailed study of the discs that form at the halo centers as the disc thickness is barely resolved. More accurate analysis of the fine stream structure and disc buildup should await simulations of higher resolution.

**Computing the flux abundance.** In order to evaluate the conditional probability  $P(\dot{M}|M_v)$  for eq. (2), we measure  $P_0(\dot{M}|M_0)$  from a fair sample of MareNostrum galaxies in haloes of  $M_0 = 10^{12} M_\odot$  at  $z_0 = 2.5$  (Supplementary Information). We then generalize it to other masses  $M_v$  using the scaling from eq. (1),  $\dot{M} \propto M_v^{1.15}$ , namely

$$P(\dot{M}|M_v) = P_0[\dot{M}(M_0/M_v)^{1.15}|M_0]. \quad (4)$$

At  $z \sim 2.5$ , this estimate of  $\dot{M}$  is good to within a factor of two for  $M_v \leq 10^{13} M_\odot$ , beyond which it becomes a more severe overestimate (Goerdt et al., in preparation). The results for other redshifts ( $z > 2$ ) are obtained using the scaling from eq. (1),  $\dot{M} \propto (1+z)^{2.25}$ .

- 
1. Chapman, S. C., Smail, I., Blain, A. W. & Ivison, R. J. A Population of Hot, Dusty Ultraluminous Galaxies at  $z \sim 2$ . *Astrophys. J.* 614, 671-678 (2004).
  2. Genzel, R. *et al.* The rapid formation of a large rotating disk galaxy three billion years after the Big Bang. *Nature* 442, 786-789 (2006).
  3. Förster Schreiber, N. M. *et al.* SINFONI Integral Field Spectroscopy of  $z \sim 2$  UV-selected Galaxies: Rotation Curves and Dynamical Evolution. *Astrophys. J.* 645, 1062-1075 (2006).
  4. Genzel, R. *et al.* From rings to bulges: evidence for rapid secular galaxy evolution at  $z \sim 2$  from integral field spectroscopy in the SINS survey. ArXiv e-prints 0807.1184 (2008).
  5. Ocvirk, P., Pichon, C. & Teyssier, R. Bimodal gas accretion in the MareNostrum galaxy formation simulation. ArXiv e-prints 0803.4506 (2008).
  6. Neistein, E., van den Bosch, F. C. & Dekel, A. Natural downsizing in hierarchical galaxy formation. *Mon. Not. R. Astron. Soc.* 372, 933-948 (2006).

7. Neistein, E. & Dekel, A. Merger Rates of Dark-Matter Haloes. ArXiv e-prints 0802.0198 (2008).
8. Dekel, A. & Birnboim, Y. Galaxy bimodality due to cold flows and shock heating. *Mon. Not. R. Astron. Soc.* 368, 2-20 (2006).
9. Wall, J. V., Pope, A. & Scott, D. The evolution of submillimetre galaxies: two populations and a redshift cut-off. *Mon. Not. R. Astron. Soc.* 383, 435-444 (2008).
10. Tacconi, L. J. *et al.* Submillimeter Galaxies at  $z \sim 2$ : Evidence for Major Mergers and Constraints on Lifetimes, IMF, and CO-H2 Conversion Factor. *Astrophys. J.* 680, 246-262 (2008).
11. Madau, P., Pozzetti, L. & Dickinson, M. The Star Formation History of Field Galaxies. *Astrophys. J.* 498, 106-114 (1998).
12. Bouché, N. *et al.* Dynamical Properties of  $z \sim 2$  Star-forming Galaxies and a Universal Star Formation Relation. *Astrophys. J.* 671, 303-309 (2007).
13. Lacey, C. & Cole, S. Merger rates in hierarchical models of galaxy formation. *Mon. Not. R. Astron. Soc.* 262, 627-649 (1993).
14. Neistein, E. & Dekel, A. Constructing merger trees that mimic N-body simulations. *Mon. Not. R. Astron. Soc.* 383, 615-626 (2008).
15. Genel, S. *et al.* Mergers and Mass Accretion Rates in Galaxy Assembly: The Millennium Simulation Compared to Observations of  $z \sim 2$  Galaxies. (2008).
16. Komatsu, E. *et al.* Five-Year Wilkinson Microwave Anisotropy Probe (WMAP) Observations: Cosmological Interpretation. ArXiv e-prints 0803.0547 (2008).
17. Birnboim, Y. & Dekel, A. Virial shocks in galactic haloes? *Mon. Not. R. Astron. Soc.* 345, 349-364 (2003).
18. Binney, J. On the origin of the galaxy luminosity function. *Mon. Not. R. Astron. Soc.* 347, 1093-1096 (2004).
19. Keres, D., Katz, N., Weinberg, D. H. & Davé, R. How do galaxies get their gas? *Mon. Not. R. Astron. Soc.* 363, 2-28 (2005).
20. Birnboim, Y., Dekel, A. & Neistein, E. Bursting and quenching in massive galaxies without major mergers or AGNs. *Mon. Not. R. Astron. Soc.* 380, 339-352 (2007).
21. Sheth, R. K. & Tormen, G. An excursion set model of hierarchical clustering: ellipsoidal collapse and the moving barrier. *Mon. Not. R. Astron. Soc.* 329, 61-75 (2002).
22. Cox, T. J., Jonsson, P., Somerville, R. S., Primack, J. R. & Dekel, A. The effect of galaxy mass ratio on merger-driven starbursts. *Mon. Not. R. Astron. Soc.* 384, 386-409 (2008).
23. Hopkins, A. M. On the Evolution of Star-forming Galaxies. *Astrophys. J.* 615, 209-221 (2004).
24. Dekel, A. & Silk, J. The origin of dwarf galaxies, cold dark matter, and biased galaxy formation. *Astrophys. J.* 303, 39-55 (1986).
25. Dekel, A. & Woo, J. Feedback and the fundamental line of low-luminosity low-surfacebrightness/ dwarf galaxies. *Mon. Not. R. Astron. Soc.* 344, 1131-1144 (2003).
26. Dekel, A. & Birnboim, Y. Gravitational quenching in massive galaxies and clusters by clumpy accretion. *Mon. Not. R. Astron. Soc.* 383, 119-138 (2008).
27. Kriek, M. *et al.* Spectroscopic Identification of Massive Galaxies at  $z \sim 2.3$  with Strongly Suppressed Star Formation. *Astrophys. J. Lett.* 649, L71-L74 (2006).
28. van Dokkum, P. G. *et al.* Confirmation of the Remarkable Compactness of Massive Quiescent Galaxies at  $z \sim 2.3$ : Early-Type Galaxies Did not Form in a Simple Monolithic Collapse. *Astrophys. J. Lett.* 677, L5-L8 (2008).
29. Prunet, S. *et al.* Initial Conditions for Large Cosmological Simulations. ArXiv e-prints 0804.3536 (2008).

30. Teyssier, R. Cosmological hydrodynamics with adaptive mesh refinement. A new high resolution code called RAMSES. *Astron. Astrophys.* 385, 337-364 (2002).
31. Rasera, Y. & Teyssier, R. The history of the baryon budget. Cosmic logistics in a hierarchical universe. *Astron. Astrophys.* 445, 1-27 (2006).
32. Press, W. H. & Schechter, P. Formation of Galaxies and Clusters of Galaxies by Self-Similar Gravitational Condensation. *Astrophys. J.* 187, 425-438 (1974).
33. Springel, V. *et al.* Simulations of the formation, evolution and clustering of galaxies and quasars. *Nature* 435, 629-636 (2005).
34. Cattaneo, A., Dekel, A., Devriendt, J., Guiderdoni, B. & Blaizot, J. Modelling the galaxy bimodality: shutdown above a critical halo mass. *Mon. Not. R. Astron. Soc.* 370, 1651-1665 (2006).
35. Croton, D. J. *et al.* The many lives of active galactic nuclei: cooling flows, black holes and the luminosities and colours of galaxies. *Mon. Not. R. Astron. Soc.* 365, 11-28 (2006).
36. Bower, R. G. *et al.* Breaking the hierarchy of galaxy formation. *Mon. Not. R. Astron. Soc.* 370, 645-655 (2006).
37. Cattaneo, A., Dekel, A., Faber, S. M. & Guiderdoni, B. *et al.* Downsizing by Shutdown in Red Galaxies. ArXiv e-prints 0801.1673 (2008).

**Acknowledgments** We acknowledge stimulating discussions with N. Bouche, R. Genzel, A. Kravtsov, A. Pope, A. Sternberg & J. Wall. This research has been supported by the France-Israel Teamwork in Sciences, the German-Israel Science Foundation, and a Minerva fellowship (TG). We thank the computer resources and technical support by the Barcelona Centro Nacional de Supercomputacion. The simulation is part of the Horizon collaboration.

**Author Information** The authors declare no competing financial interests. Correspondence and requests for materials should be addressed to A.D. (dekel@phys.huji.ac.il).



## MASSIVE GALAXY FORMATION BY COLD STREAMS

This is an extension of the Letter to Nature, aimed at providing further details, in support of the results reported in the main body of the Letter.

### 1 On the origin of narrow streams

Dekel & Birnboim 2006<sup>8</sup> (hereafter DB06) put forward the conjecture that at redshifts higher than  $z_{\text{crit}} \sim 2$ , narrow cold streams penetrate deep into the dark-matter haloes even when the haloes are more massive than the shock-heating scale,  $M_{\text{shock}} \lesssim 10^{12} M_{\odot}$ . This prediction is summarized in Fig. 5.

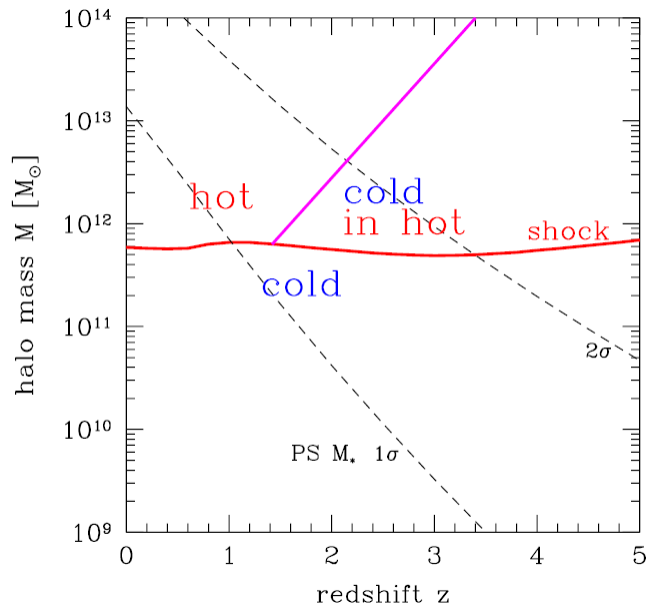


Figure 5: Analytic prediction for the regimes dominated by cold flows and shock-heated medium in the plane of halo mass and redshift, based on Fig. 7 of DB06. The nearly horizontal curve marks the robust threshold mass for a stable shock based on spherical infall analysis,  $M_{\text{shock}}(z)$ . Below this curve the flows are predicted to be predominantly cold and above it a shock-heated medium is expected to extend out to the halo virial radius. The inclined solid curve is the conjectured upper limit for cold streams, valid at redshifts higher than  $z_{\text{crit}} \sim 2$ . The hot medium in haloes of  $M_v > M_{\text{shock}}$  at  $z > z_{\text{crit}}$  is predicted to host penetrating cold streams, while haloes of a similar mass at  $z < z_{\text{crit}}$  are expected to be all hot, shutting off most of the gas supply to the inner galaxy. Also shown is the characteristic Press-Schechter halo mass  $M_*(z)$ ; it is much smaller than  $M_{\text{shock}}$  at  $z > 2$ .

The critical condition for a stable virial shock is that the radiative cooling rate behind the shock is slower than the compression rate,  $t_{\text{cool}}^{-1} < t_{\text{comp}}^{-1}$ , allowing the buildup of pressure support behind the shock against global gravitational collapse. Based on a spherical analysis, DB06 found that a virial shock should exist in dark-matter haloes above a threshold mass  $M_{\text{shock}} \lesssim 10^{12} M_{\odot}$  that is rather constant in time, at an actual value that is sensitive to the metallicity of the gas in the halo. The existence of such a threshold mass and its value as a function of redshift have been confirmed by the analysis of cosmological simulations<sup>19,8,20,5</sup>. However, at high redshifts, even above the threshold mass, a shock is not expected to develop along narrow, cold, radial streams that penetrate through the halo, because the cooling there is more efficient than in the surrounding halo.

The appearance of intense streams at high  $z$ , as opposed to their absence at low  $z$ , reflects the interplay between the shock-heating scale and the independent characteristic scale of nonlinear clustering, i.e., the Press-Schechter<sup>32</sup> mass  $M_*$  that corresponds to the typical dark-matter haloes forming at a given epoch. The key difference between the two epochs is that the rapid growth of  $M_*$  with time, as seen in Fig. 5, makes  $M_{\text{shock}} \gg M_*$  at  $z > 2$  while  $M_{\text{shock}} \sim M_*$  at lower redshifts.

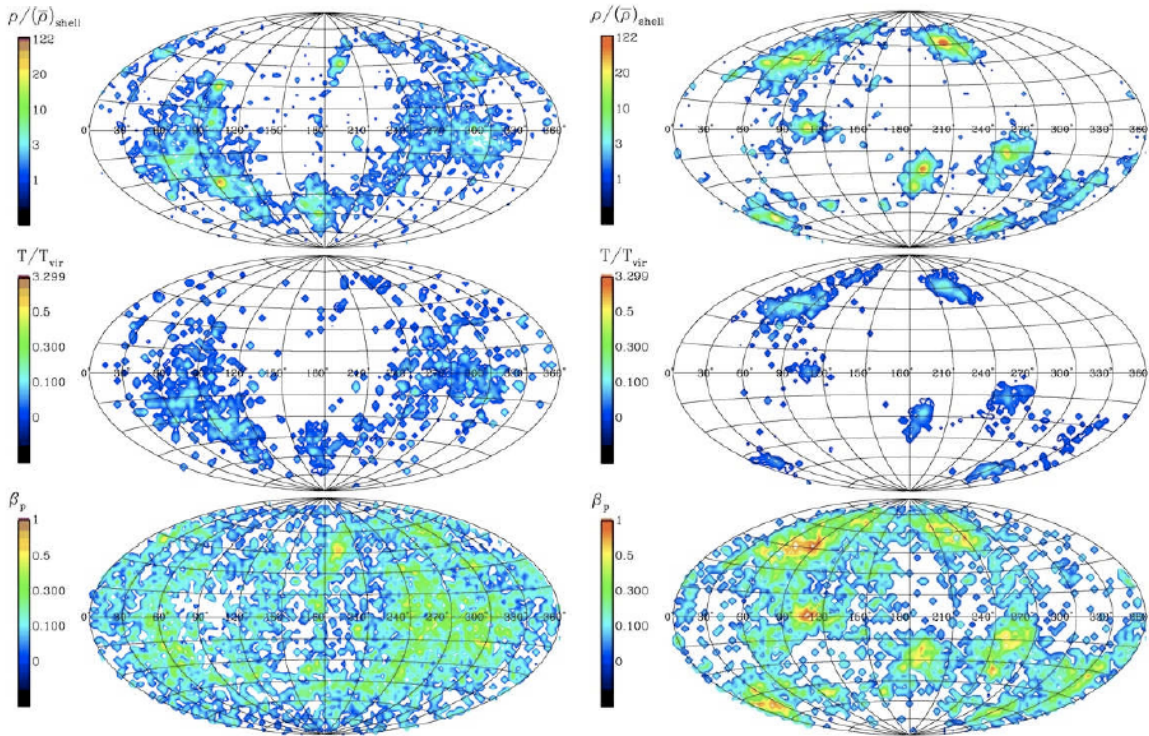


Figure 6: The pattern of dark-matter inflow in a shell  $(1-3)R_v$  outside two haloes from a cosmological N-body simulation at  $z = 0$  (based on P. Seleson & A. Dekel, in preparation). **Left:** a typical halo with  $M_v \sim M_\star$ . **Right:** a rare halo with  $M_v \gg M_\star$ . In terms of the different ways by which these two haloes are fed by dark-matter, they correspond to two haloes of the same mass  $M_v \sim 10^{12} M_\odot$ , but at  $z \sim 0$  and  $z \sim 2 - 3$  respectively. Top to bottom: density, temperature and infall velocity. We see that the typical halo resides inside a broad filament so it is practically fed by wide-angle diffuse accretion. On the other hand, the rare halo is fed by a few narrow, dense, in-flowing filaments.

The following argument explains why rare dark-matter haloes of  $M_v \gg M_\star$  are fed by narrow streams, while typical haloes  $\sim M_\star$  accrete from a wide angle. The large-scale structure of dark matter is expected to be roughly self-similar in time when masses are measured in terms of  $M_\star$  and densities in terms of the background universal density. We learn from cosmological N-body simulations<sup>19,33</sup> that this is indeed the case for the large-scale filamentary structure: the characteristic width of the filaments is comparable to  $R_\star \propto M_\star^{1/3}$ , the typical size of an  $M_\star$  halo, while the typical filament length is larger by about an order of magnitude and scales similarly in time. This means that while the infall pattern into  $\sim M_\star$  haloes is practically a wide-angle, nearly spherical pattern, the infall into  $M_v \gg M_\star$  haloes is along a few well-defined filaments that are thin relative to the halo size. Assuming that at any given epoch the accretion rate of dark matter,  $\dot{M}$ , is roughly proportional to the halo mass  $M_v$  (Eq. 1 of the Letter), while the virial densities in haloes of all masses are the same (by definition), this geometrical difference implies that the densities in the filaments penetrating  $M_v \gg M_\star$  haloes are higher by a factor of a few than the typical densities in their host haloes. This is demonstrated in Fig. 6.

Assuming that the density of the gas flowing along the filaments scales with the dark-matter density, and that the infall velocity is comparable to the halo virial velocity, we conclude that the cooling rate in the filaments feeding an  $M_v \gg M_\star$  halo should be higher by a factor of a few than in the surrounding spherical halo. If the compression rate in the filaments is comparable to that in the host halo, this implies that the thin filaments have a harder time supporting a stable shock. As a result, the critical halo mass for shock heating in the filaments feeding it must be larger by a factor of a few. This is the case for  $M_v \gtrsim M_{shock}$  haloes at high redshifts.

A crude estimate led DB06 to the conjectured upper limit for penetrating streams shown in Fig. 5:

$$M_{stream} \sim \frac{M_{shock}}{f M_\star} M_{shock} \quad \text{for} \quad f M_\star < M_{shock}, \quad (5)$$

where the characteristic width of the streams is  $\propto (fM_\star)^{1/3}$ , with  $f$  a factor of order a few. At low  $z$ , where  $fM_\star > M_{shock}$ , cold flows exist only for  $M_v < M_{shock}$ . At high  $z$ , where  $fM_\star < M_{shock}$ , cold streams appear even in  $M_v > M_{stream}$  haloes where shocks have heated part of the gas, as long as  $M_v < M_{stream}$ . The critical redshift  $z_{crit}$  separating these two regimes is defined by

$$fM_\star(z_{crit}) = M_{shock} . \quad (6)$$

This crude maximum mass for cold streams is shown in Fig. 5 for an arbitrary choice of  $f = 3$ .

A preliminary analysis of the MareNostrum simulation<sup>5</sup> confirms the prediction of eq. 5, when taking into account the lower metallicities in the simulation compared to that assumed in the analytic calculation. The streams analyzed in the current Letter, in dark-matter haloes of  $M_v = 10^{12}M_\odot$  at  $z = 2.5$ , represent an encouraging confirmation of the validity of the DB06 conjecture. Further analysis in progress (T. Goerdt et al., in preparation) indicates, for example, that at  $z = 2.5$ , the fraction of inflow in cold streams drops by a factor of three at  $M_v \simeq 2 \times 10^{13}M_\odot$ , much in the spirit of the crude prediction of Fig. 5. The permitted cold gas supply by streams in massive haloes at high redshift, followed by a shutdown above  $M_{shock}$  at low redshifts, turn out to provide good match to many observed galaxy properties when these features are incorporated in semi-analytic simulations of galaxy formation<sup>34–37</sup>.

## 2 Maps of entropy, flux and density for several galaxies

Fig. 7 to 9 extend the visual information provided by Figs. 1 and 2 of the Letter. They display different gas properties that highlight the structure and kinematics of the cold streams in three simulated galaxies of  $M_v = 10^{12}M_\odot$  at  $z = 2.5$ .

The entropy maps show  $\log(T/\rho^{2/3})$  where the temperature and gas density are in units of the virial temperature and mean density within the halo virial radius  $R_v$ . They exhibit the virial shock, covering most of the area of the virial sphere and sometimes extending beyond  $2R_v$ . The narrow streams are of much lower entropy, by more than three orders of magnitude, comparable to the low entropy in the central disc they lead to. The boundaries between the streams and the hot medium within the virial radius are sharp and well defined. We also note that semi-cylindrical shocks sometimes partly surround the elongated streams long before they enter the halo virial radius.

The arrows mark the velocity field projected on the slice plane, and the flux color maps show the flow rate per solid angle,  $\dot{m} = r^2 \rho v_r$ . The flux inward is almost exclusively channeled through the narrow streams. This flux is several times the average over a sphere,  $\dot{m}_{vir} \simeq 8 M_\odot \text{ yr}^{-1} \text{ rad}^{-2}$ . The opening angle of a typical stream at  $R_v$  is  $20 - 30^\circ$ , so the streams cover a total area of  $\sim 0.4 \text{ rad}^2$ , namely a few percent of the sphere. The velocity field in the hot medium is turbulent and sometimes showing vast outflows. The inward flux over most of the sphere area is negligible, both inside and outside the virial radius or the virial shock. The streaming velocities are supersonic, with a Mach number of order a few.

Although the streams tend to be rather radial when viewed on scales comparable to the halo virial radius, some of them flow in with impact parameters on the order of 10 kpc, comparable to the disc sizes. The steady high flux along a line of a rather fixed orientation with a non-negligible impact parameter is the source of angular momentum required for the buildup of an extended rotating disc (A. Zinger et al., in preparation).

The gas density maps emphasize the narrowness of the streams, and reveal that they are typically denser than the surrounding medium by more than an order of magnitude. This confirms the prediction described in §E, and explains why a virial shock is avoided along the streams, allowing them to penetrate cold and unperturbed into the inner halo.

The column-density maps of the inflowing material are obtained by summing up the densities in grid cells along each line of sight inside the box of side 320 kpc. The cells that enter this sum are only those where the inward flux per solid angle is at least twice the average over a sphere based on Eq. 1 of the Letter. The densities

here are in units of  $cm^{-3}$ , after dividing by  $0.6m_p$ . These maps highlight the three-dimensional configuration of radial streams, and the clumps along some of them.

Fig. 10 displays three-dimensional TIPSYS<sup>1</sup> pictures of the radial influx  $\dot{m}$ , similar to Fig. 2 of the Letter. It shows the overall structure of the inflowing streams in 3D perspective for four simulated haloes. The pictures reveal that the typical configuration is of three major narrow streams. Some of the streams are straight lines, and others are curved. Some of the streams are of rather fixed width from well outside  $R_v$ , and others display a conical shape, starting broad at large radii and getting narrower as they penetrate into the halo. The gas streams show dense clumps, with about half the stream mass in clumps of mass ratio  $\mu > 0.1$ , namely mass above  $\sim 10^{10}M_\odot$ . The rest is in smaller clumps, some clearly hidden below the resolution limit. Since these mini-minor clumps are not expected to cause significant damage to the central disc<sup>22</sup>, we can refer to them in this respect as “smooth” flows. It is not clear at this point to what extent the smooth component is truly smooth or built by mini-minor clumps, and whether the perfect smoothness has a physical origin or is merely a numerical artifact, but this distinction does not make a qualitative difference to our present discussion.

---

<sup>1</sup><http://www-hpcc.astro.washington.edu/tools/tipsy/tipsy.html>

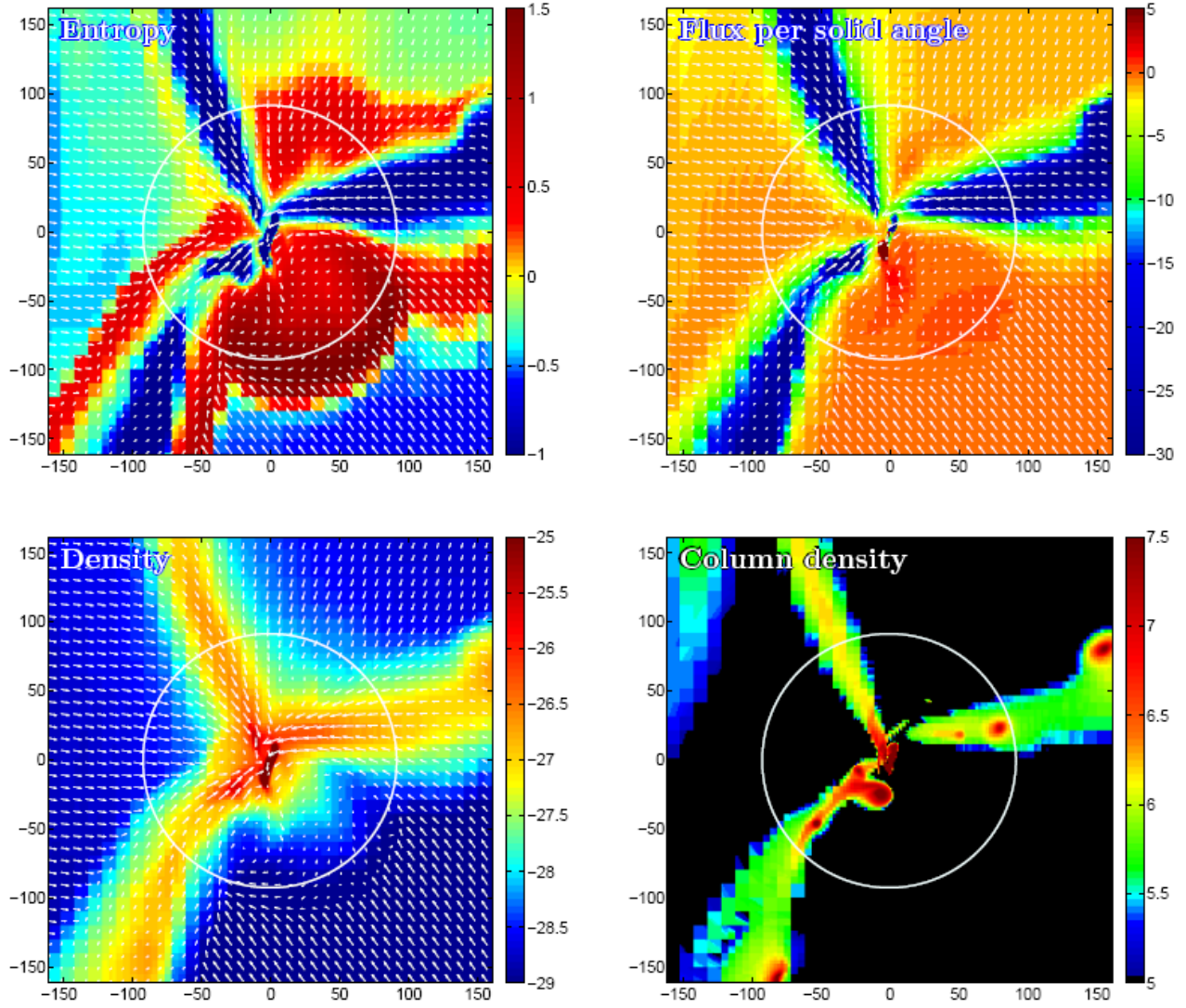


Figure 7: Gas in halo 314 of the MareNostrum simulation. Three maps refer to a thin equatorial slice. They show (a) entropy  $\log K = \log(T/\rho^{2/3})$  in units of the virial quantities, (b) radial flux  $\dot{m} = r^2 \rho v_r$  in  $M_\odot \text{yr}^{-1} \text{rad}^{-2}$ , and (c) log density in units of the mean gas density within  $R_v$ . The fourth panel shows log column density through the 3D box of side 320 kpc, considering only the cells where the radial flux inward is at least twice as high as the average over a shell based on Eq. 1 of the Letter. The circle marks the virial radius.

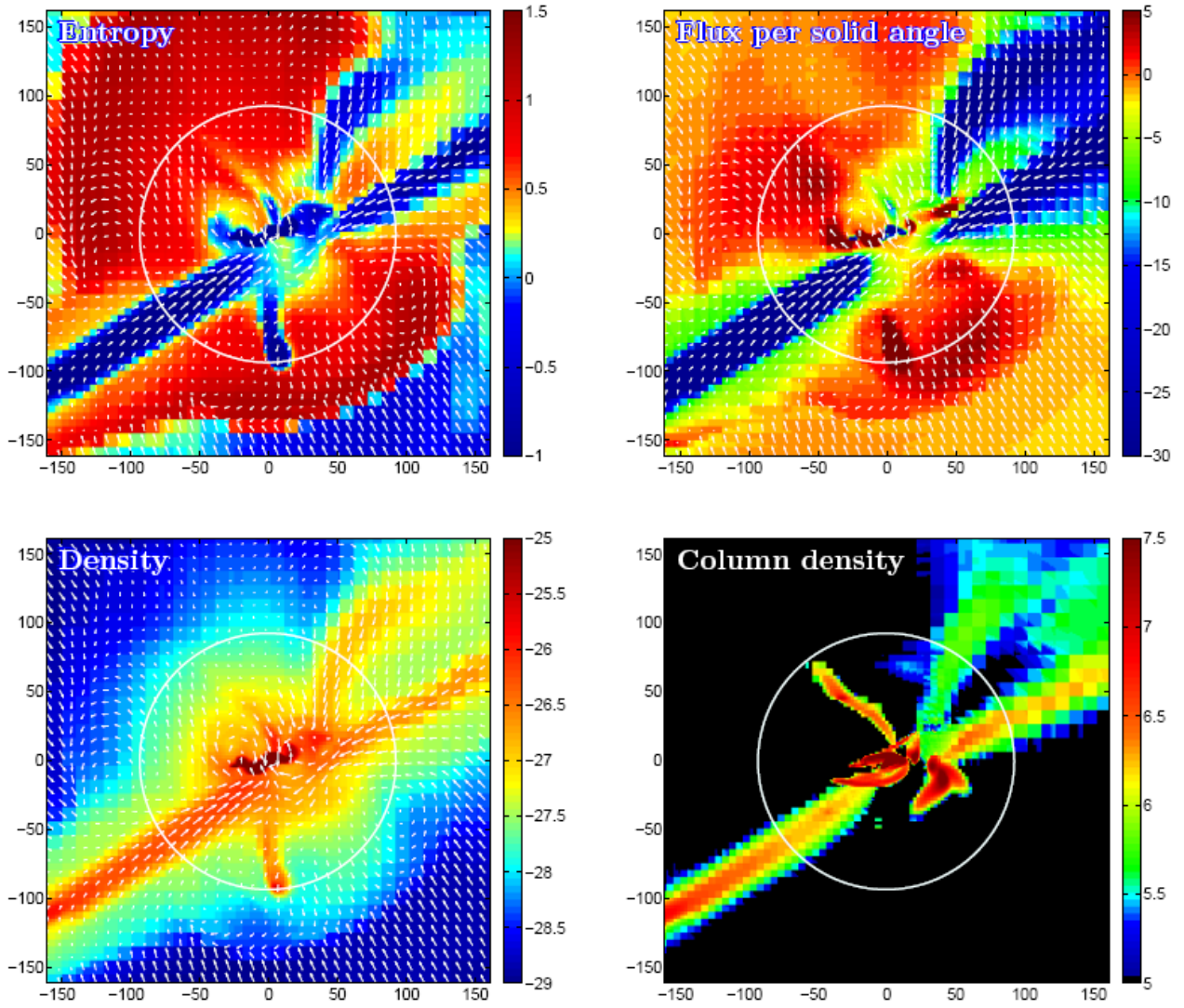


Figure 8: Gas in halo 303 of the MareNostrum simulation. Three maps refer to a thin equatorial slice. They show (a) entropy  $\log K = \log(T/\rho^{2/3})$  in units of the virial quantities, (b) radial flux  $\dot{m} = r^2 \rho v_r$  in  $M_\odot \text{yr}^{-1} \text{rad}^{-2}$ , and (c) log density in units of the mean gas density within  $R_v$ . The fourth panel shows log column density through the 3D box of side 320 kpc, considering only the cells where the radial flux inward is at least twice as high as the average over a shell based on Eq. 1 of the Letter. The circle marks the virial radius.



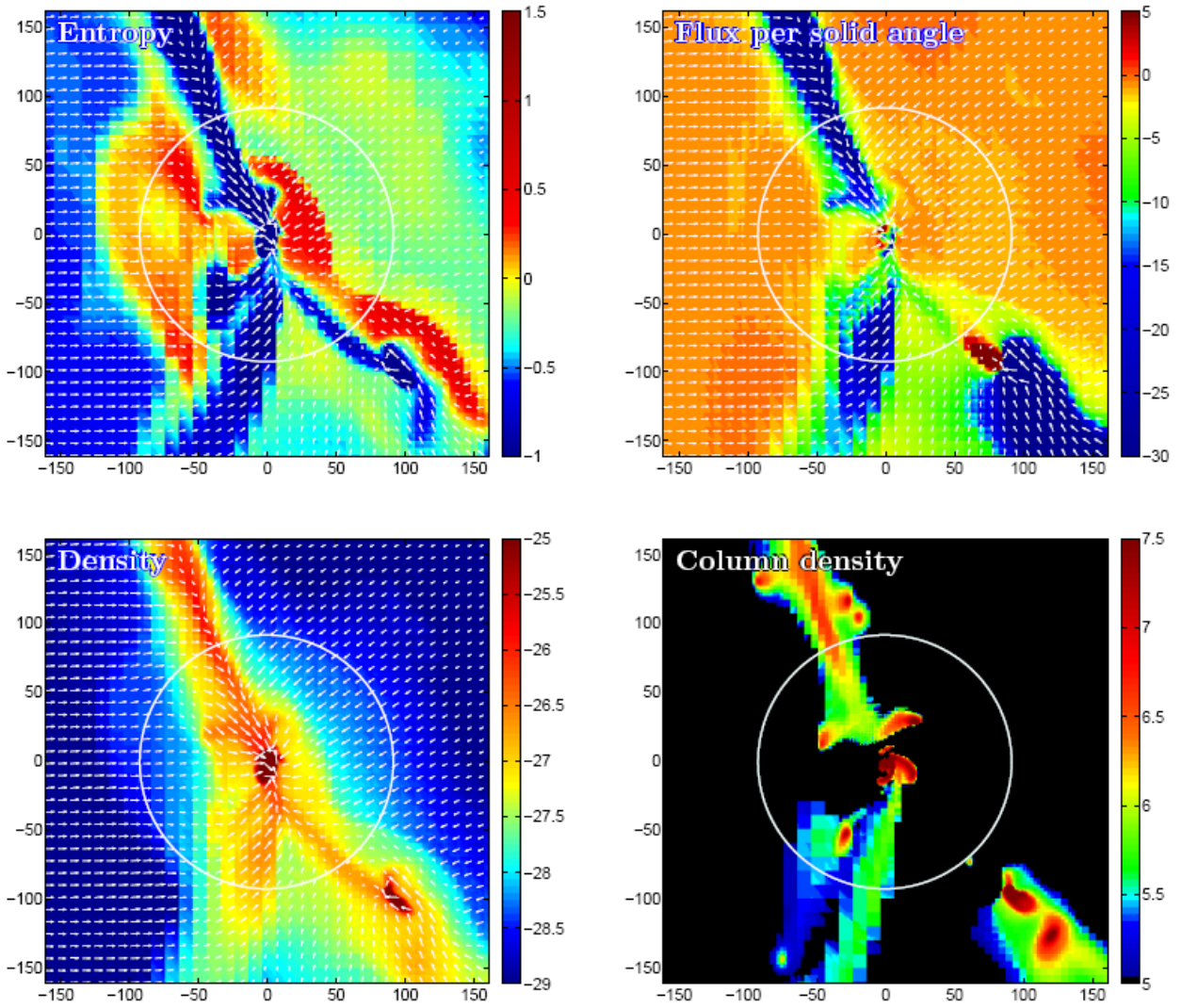


Figure 9: Gas in halo 311 of the MareNostrum simulation. Three maps refer to a thin equatorial slice. They show (a) entropy  $\log K = \log(T/\rho^{2/3})$  in units of the virial quantities, (b) radial flux  $\dot{m} = r^2 \rho v_r$  in  $M_\odot \text{yr}^{-1} \text{rad}^{-2}$ , and (c) log density in units of the mean gas density within  $R_v$ . The fourth panel shows log column density through the 3D box of side 320 kpc, considering only the cells where the radial flux inward is at least twice as high as the average over a shell based on Eq. 1 of the Letter. The circle marks the virial radius.

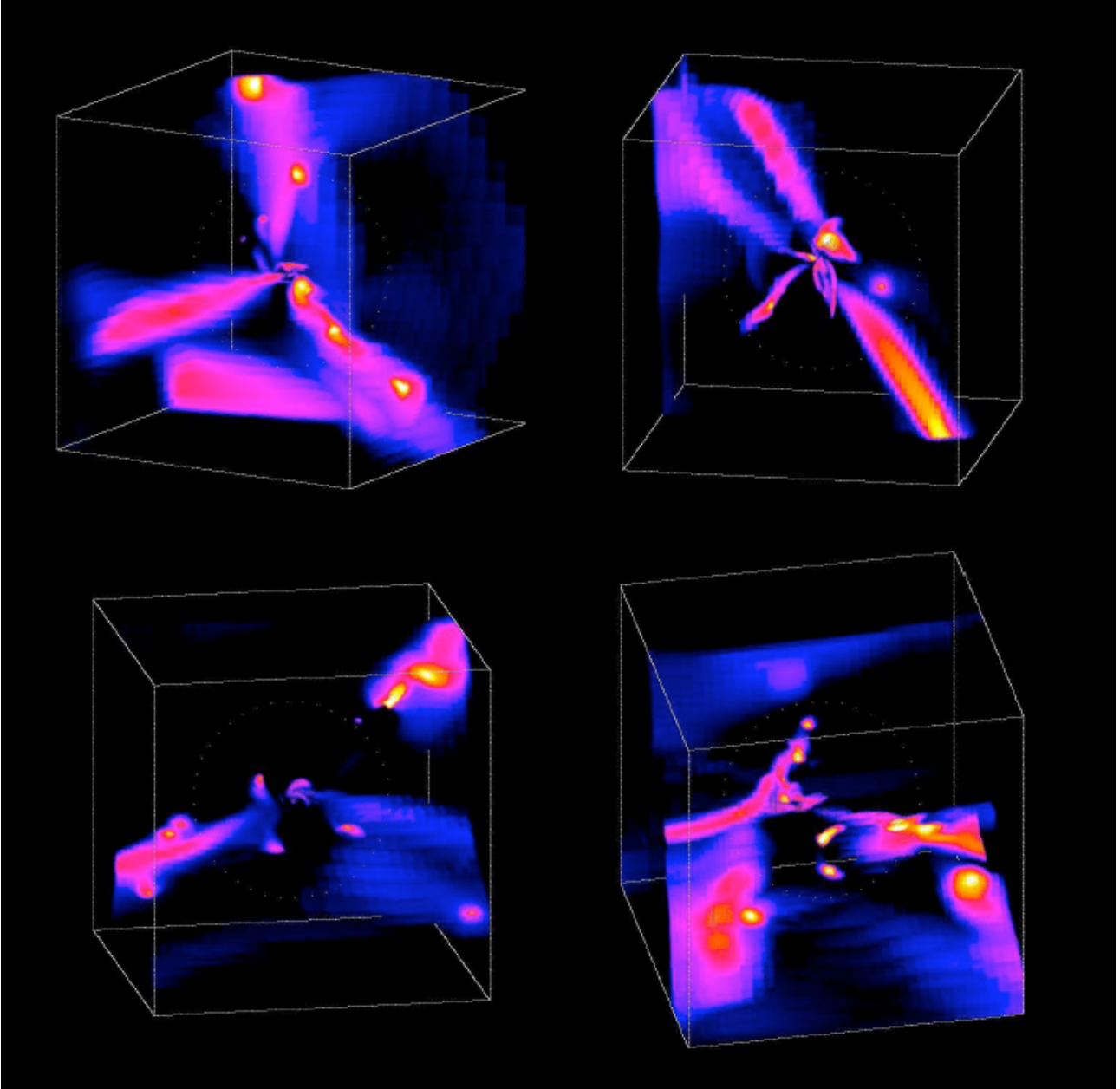


Figure 10: Inward flux in the three-dimensional boxes of side 320 kpc centered on galaxies 314, 303, 311 and 310 from the MareNostrum simulations. The colors refer to inflow rate per solid angle of point-like tracers at the centers of the cubic grid cells. The dotted circle marks the virial radius. All haloes show high-flux streams, some smooth and some with embedded clumps. Galaxy 310 (bottom right) is undergoing multiple minor mergers due to the particularly clumpy streams.



### 3 Flux profiles and probability distribution

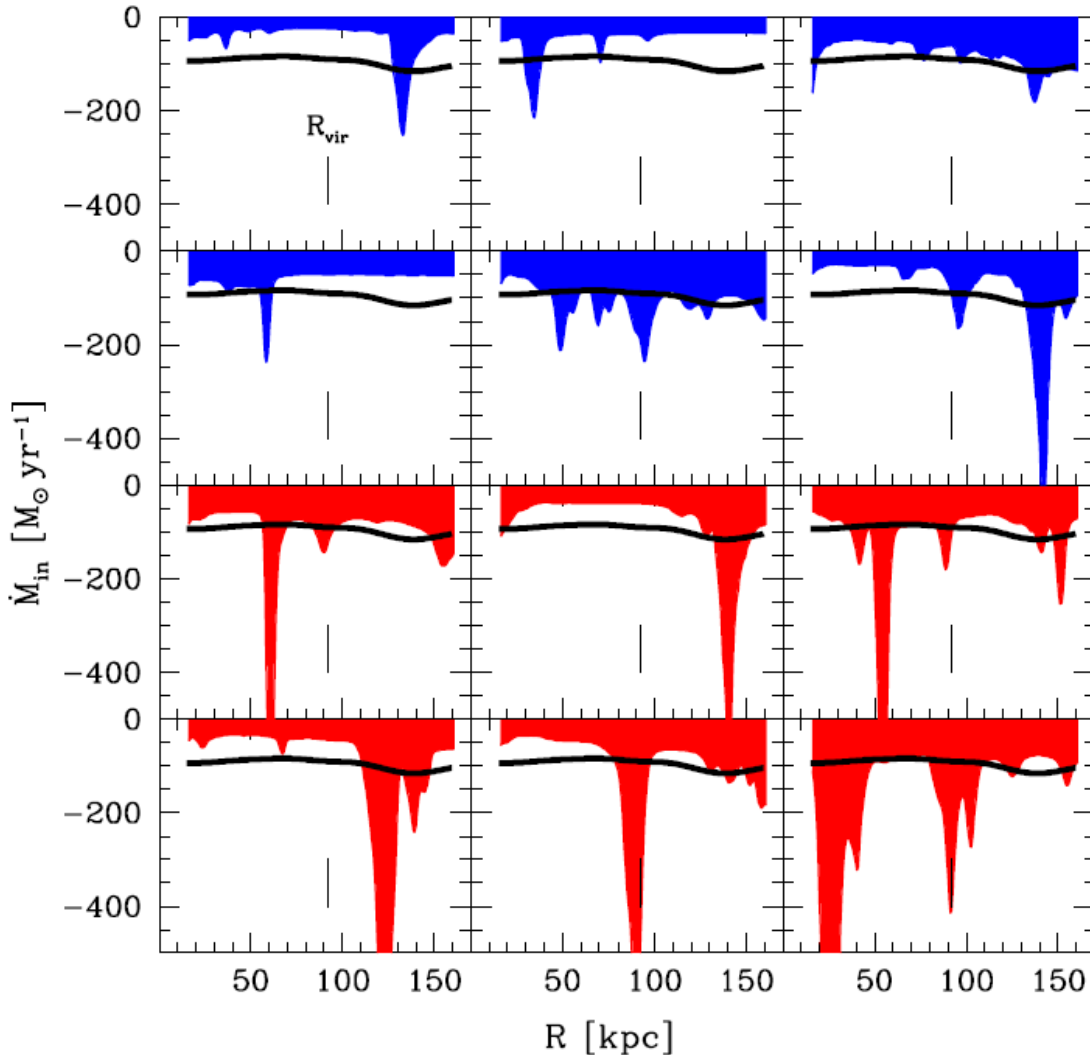


Figure 11: Profiles of total gas inflow rate through spherical shells as in Fig. 3 of the Letter. Shown here are twelve galaxies of  $M_v \approx 10^{12} M_\odot$  at  $z = 2.5$ , randomly chosen from the simulation. The lower six panels show clumps that correspond to mergers of mass ratio  $\mu > 0.1$ , while the upper six are fed by smoother flows with only mini-minor mergers of  $\mu < 0.1$ .

Fig. 11 is an extension of Fig. 3 of the Letter, presenting the influx profiles of twelve galaxies, all with  $M_v \simeq 10^{12} M_\odot$  at  $z = 2.5$ , chosen at random from the MareNostrum simulation. The profiles extend from  $r = 15$  kpc, the disc vicinity, to  $r = 160$  kpc, almost twice the virial radius of  $R_v \simeq 90$  kpc. Six galaxies turn out to show clumps leading to mergers of  $\mu > 0.1$ , and the rest show only smaller clumps in smoother flows. One can read from the relative width of the clumps in the figure that the duty cycle for  $\mu > 0.1$  clumps in each individual galaxy is less than 0.1. By comparing the areas above the individual profiles with the average for galaxies of that mass and redshift, one can see that on average only about half the stream mass is in clumps.

Fig. 12 shows the probability distribution of  $\dot{M}$  for the fiducial galaxies of  $M_v = M_0 = 10^{12} M_\odot$  at  $z = 2.5$ . It has been derived as explained in the Methods section of the Letter, by uniform sampling of the flux profiles shown in Fig. 11. This  $P_0(\dot{M}|M_0)$  is used in Eq. 4 of the Letter to derive the conditional probability for other halo masses,  $P(\dot{M}|M_v)$ , which is then used in Eq. 2 to derive the abundance of galaxies with a given  $\dot{M}$ . The tail of the distribution at  $\dot{M} > 200 M_\odot \text{ yr}^{-1}$  is dominated by  $\mu > 0.1$  mergers, while the main body of the distribution is mostly due to smoother streams. Recall that the average is about  $100 M_\odot \text{ yr}^{-1}$ .

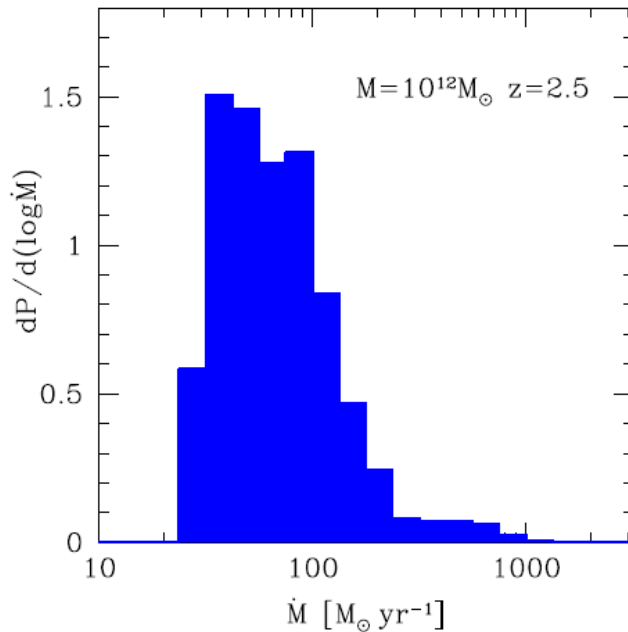


Figure 12: The conditional probability distribution  $P(\dot{M}|M_v)$  for the fiducial case  $M_v = M_0 = 10^{12} M_\odot$  at  $z = 2.5$ .

#### 4 The abundance as a function of mass and redshift

As described in Methods, we derived the conditional probability distribution  $P(\dot{M}|M_v)$  from the simulated haloes at  $z = 2.5$  for a fiducial halo mass  $M_v = 10^{12} M_\odot$ , shown in Fig. 12. We then used the scaling of eq. 1 of the Letter to obtain an estimate for other halo masses. Preliminary analysis of more massive haloes at that redshift (T. Goerdt et al., in preparation) indicates that the actual flux starts dropping below the adopted estimate in haloes more massive than  $M_{stream} \sim 10^{13} M_\odot$ . For a first crude estimate of the effect this might have on our results shown in Fig. 4 of the Letter, we re-compute the comoving number density  $n(>\dot{M})$  as described in the main text, but now limit the halo mass range that contributes to  $\dot{M}$  by an upper cutoff at  $M_{stream}$ . Fig. 13 shows the results for different values of  $M_{stream}$ . We see that a cutoff at  $M_{stream} = 10^{13} M_\odot$  makes only a small difference to  $n(>\dot{M})$ , by a factor of  $\sim 2$  at the high- $\dot{M}$  regime corresponding to the bright SMGs. Thus, the decay of cold streams above  $10^{13} M_\odot$  is not expected to alter our results in a qualitative way. On the other hand, we learn from the fact that the symbols lie far above the lower curve that the high-SFR objects at these redshifts are dominated by central galaxies in haloes more massive than  $10^{12} M_\odot$ . In fact, we find that some of the SFGs and many of the bright SMGs are associated with haloes more massive than  $3 \times 10^{12} M_\odot$ .

Fig. 13 also shows the predicted abundance  $n(>\dot{M})$  at different redshifts, now applying no finite upper mass cutoff  $M_{stream}$ . This is justified for  $z > 2$  based on our preliminary investigation of the MareNostrum galaxies at different redshifts and masses and consistent with the conjecture of DB06<sup>8</sup>. We see that the comoving abundance of galaxies with  $\dot{M} \sim 150 M_\odot \text{ yr}^{-1}$  is predicted to vary by a factor less than two between  $z = 2$  and 4. By  $z \sim 7$  that abundance drops by an order of magnitude. The variation with redshift is somewhat larger at the high-flux end, toward  $\dot{M} \sim 10^3 M_\odot \text{ yr}^{-1}$ . At lower redshifts, the contribution of streams in massive haloes above  $M_{shock}$  is most likely overestimated by this procedure, so a similar analysis in the low- $z$  regime should impose an upper limit at  $M_{stream} \simeq M_{shock}$ .

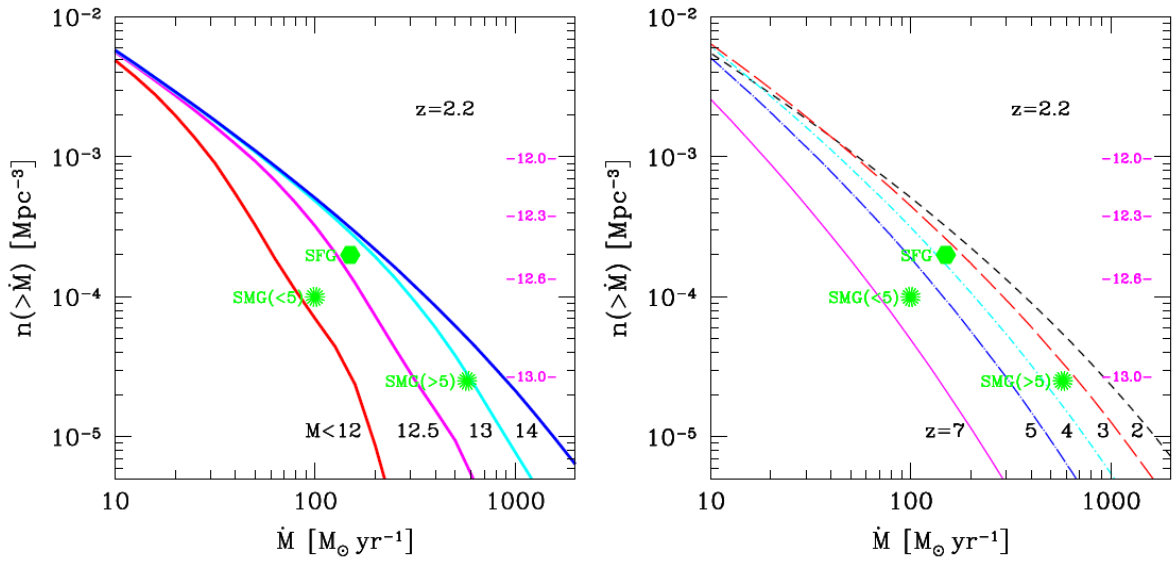


Figure 13: Comoving number density of galaxies with total gas inflow rate higher than  $\dot{M}$  at  $z = 2.2$ , as in Fig. 4 of the main body of the Letter. The numbers on the right refer to  $\log M_v$  of haloes with the corresponding abundance. **Left:** Dependence on the maximum halo mass that contributes to cold streams, for  $M_{stream} = 10^{12}, 10^{12.5}, 10^{13}, 10^{14} M_\odot$ . **Right:** Variation with redshift,  $z = 2, 3, 4, 5, 7$ .